FDR4ALT

Validation Report Document (FDR)

CLS-ENV-NT-23-0426

Issue 4.1 – 04/07/2023

Public

AUTHORS TABLE

Object	Name
Authors	Mathilde Siméon, Marie-Laure Fréry, Jean-Alexis Daguzé, Fanny Piras (CLS)
Checked by	Gabriele Brizzi (SERCO) and Pierre Féménias (ESA)
Accepted by	Pierre Féménias (ESA)

CHRONOLOGY ISSUES

Issue	Date	Object
1.0	17/05/22	Draft version for Phase 2 PM#1
2.0	02/12/22	Intermediate version for Phase 2 PM #1 (80% completed for ENVISAT)
3.0	02/05/23	Final version for Final Review
4.0	23/05/23	Final version for Final Review with RIDs implemented
4.1	04/07/23	Final version: document has been splitted between FDR and TDP to have ligher documents

TABLE OF CONTENT

LIST OF FIGURES

LIST OF TABLES

1 Introduction

This document has been written in the frame of the FDR4ALT project, ESA contract N°4000128220/19/I-BG. It is a deliverable of task 4 of the project and is identified as [D-4-02].

1.1 The FDR4ALT Project

In the framework of the European Long Term Data Preservation Program (LTDP+) which aims at generating innovative Earth system data records named Fundamental Data Records (basically level 1 altimeter and radiometer data) and Thematic Data Records (basically level 2+ geophysical products), ESA/ESRIN has launched a reprocessing activity of ERS-1, ERS-2 and ENVISAT altimeter and radiometer dataset, called the FDR4ALT project (Fundamental Data Records for Altimetry). A large consortium of thematic experts has been formed to perform these activities which are:

1) To define products including the long, harmonized record of uncertainty-quantified observations.

2) To define the most appropriate level 1 and level 2 processing.

3) To reprocess the whole times series according to the predefined processing.

4) To validate the different products and provide them to large communities of users focused on the observation of the atmosphere, ocean topography, ocean waves, coastal, hydrology, sea ice, ice sheet regions.

1.2 Purpose and scope of the validation report

After the FDR/TDP definition step and all benchmarking (Round Robin) between standard solutions addressed by each expert group, comes the production and validation step.

The objective of this document is to provide a validation report for the Fundamental Data Records, following the strategy defined in the Validation Plan Document [D-4-01]. Note that to avoid heavy documents, the validation reports have been divided: there is one validation report for the FDRs (ALT FDR and MWR FDR) and one validation for each of the six TDPs. This document therefore contains only results for the **ALT FDR and MWR FDR**.

This document describes in detail the validation that has been performed for the FDRs to assess the performances of the FDR4ALT final products. The validation covers the full lifespan of the missions and therefore includes long-term analysis, as well as cyclic analysis or targeted analysis that are relevant for this TDP.

2 Terminology

This section aims at defining clearly the terminology used in the FDR4ALT deliverables.

- **Product** refers a specific type of file, defined and described by a dedicated handbook, and designed for a clear purpose (the FDR4ALT project, the REAPER project, …). It is a “container”. One product refers to one file. The use of plural is designed to refer to a group of files, for instance the Thematic Data Products. “FDR4ALT products” will usually refer to all TDPs and FDRs, i.e., the outputs of the whole project. Note that the word “product” does not imply any notion of start date or end date, whereas “dataset” does.
- **File** can be used to refer to one single product or any other file that is not a product.

- **Parameter or variable** refers to a product's field, i.e., the content of the product. For instance, the sea level anomaly is a parameter of the Ocean & Coastal Thematic Data Products.
  Dataset can be used to refer to any group of data, not necessarily products. However, in the context of this project, it will often be used to refer to a sub-ensemble of products, on a specific period of time or a specific geographic area. For instance, the TDS (test dataset) refers to a dataset of 3 years of test products.

3 ALT Fundamental Data Records

3.1 Introduction

In the frame of FDR4ALT project, the Altimetry Fundamental Data Record (ALT FDR) product inherits from previous official products, namely:

- ✓ Baseline V3.0 for ENVISAT
- ✓ REAPER reprocessing for ERS-1/2

Therefore, the validation of the ALT FDR focuses only on all the different improvements brought by the project, assuming that all the variables that have been extracted from the previous ERS and ENVISAT reprocessing datasets have already been validated in the frame of REAPER and V3.0, respectively.

A completeness analysis has also been performed. It is briefly described in section 3.2 but is more largely detailed in a dedicated document (Completeness Report Document [D-5-04])

3.2 Completeness

The completeness of the ALT FDR product is addressed through cyclic plots throughout the mission lifetime. For each cycle of data, a chart is produced, representing for each pass, the corresponding file size, allowing data gaps to be identified ("missing tracks" are highlighted in red). Please note that missing tracks and data gaps were already present in the original data (REAPER and V3.0). The purpose of this analysis is to give to the user an overview of the data completeness.

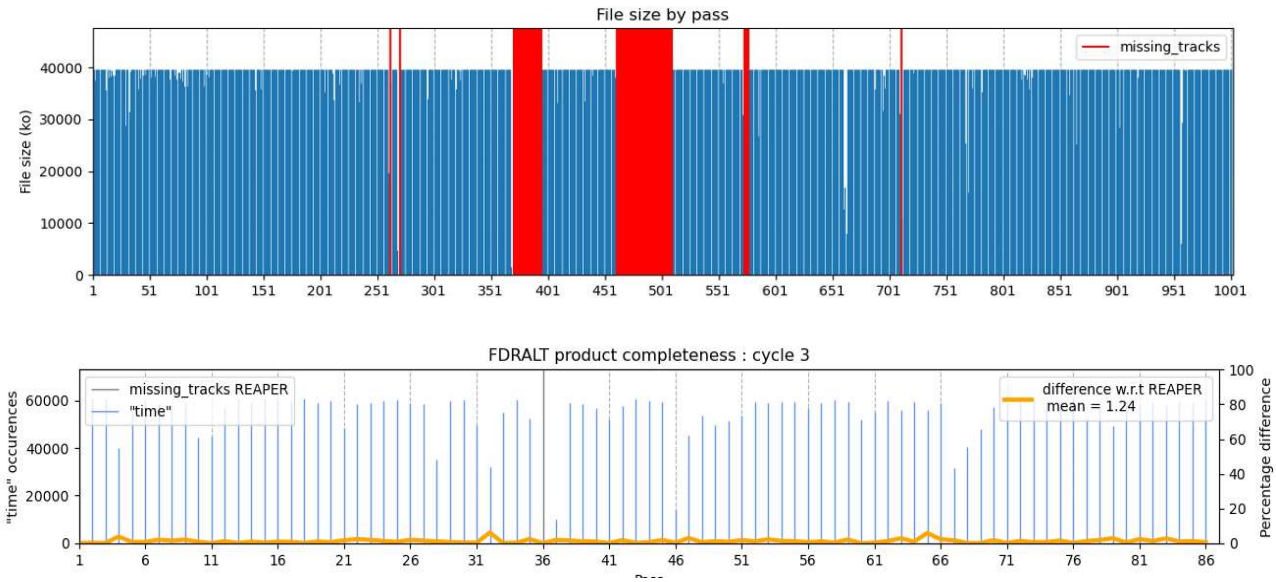

Figure 3-1 : Top: Example of a completeness cyclic plot for ENVISAT. Bottom: Example of a completeness cyclic plot for ERS

It is also crucial to validate the completeness of the FDR4ALT product against the previous official products to ensure that no data has been lost in the new reprocessing activity. In order to do so, for each data cycle, the number of tracks per cycles is compared to the previous official products.

A table, detailing all missing tracks per cycle per mission, is available in the Completeness Report Document [D-5-04].

3.3 ERS REAPER Time jumps

As explained in the REAPER Handbook [RD-1]: *"Time tags are not guaranteed to be monotonic and increasing, i.e. there may be overlapping ranges of time between files, outliers and forwards and backwards time jumps. The overlap is generally between a few seconds and half a minute. […] Time tags not only reverse but can also jump forward and then back to normal. [..] Particularly affected is ERS-1 cycle 150, where nearly every pass has a few time tags out of sync. The cause of this issue is corruption in the on-board binary counter".*

To correct this, an algorithm was developed in the frame of the FDR4ALT project: time jumps are detected in the REAPER NetCDF products by using the 1Hz consecutive time deltas, as suggested in the user handbook [RD-1]. Values with negative time deltas are discarded but some small negative 20Hz time jumps, not big enough to create a negative 1Hz time jump after compression, were still present. The second step of our algorithm detects them as well and removes the corresponding values from the REAPER products.

To detect these small 20Hz negative time jumps, a threshold of 0.95s was empirically chosen based on several tests performed on different cases. The threshold had to be small enough to not risk removing valid data, but still close to one second to remove these anomalies. Figure 3-2 shows an example of the two steps of the algorithm on one ERS file: the top plot shows the consecutive time differences, i.e., the differences between one time tag and the next, before application of the algorithm. The middle plot shows the same metrics after the first step of the algorithm (correction of the 1Hz time jumps), and the bottom plots shows the final result after correction of for the remaining 20Hz time jumps using the 0.95s threshold.

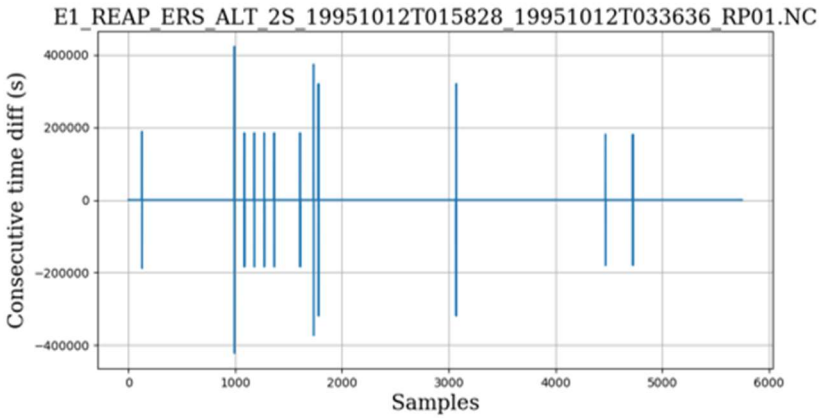

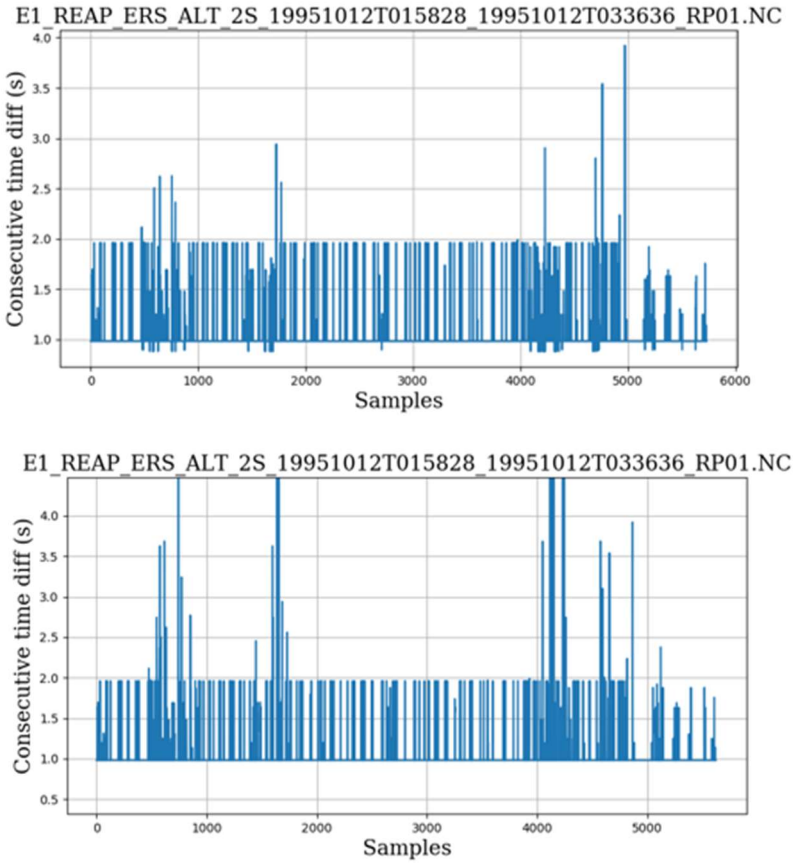

Figure 3-2 : Consecutive time differences for one ERS file, before correction (top), after the first step removing the main time jumps (middle) and after the correction of the remaining 20Hz time jumps (bottom)

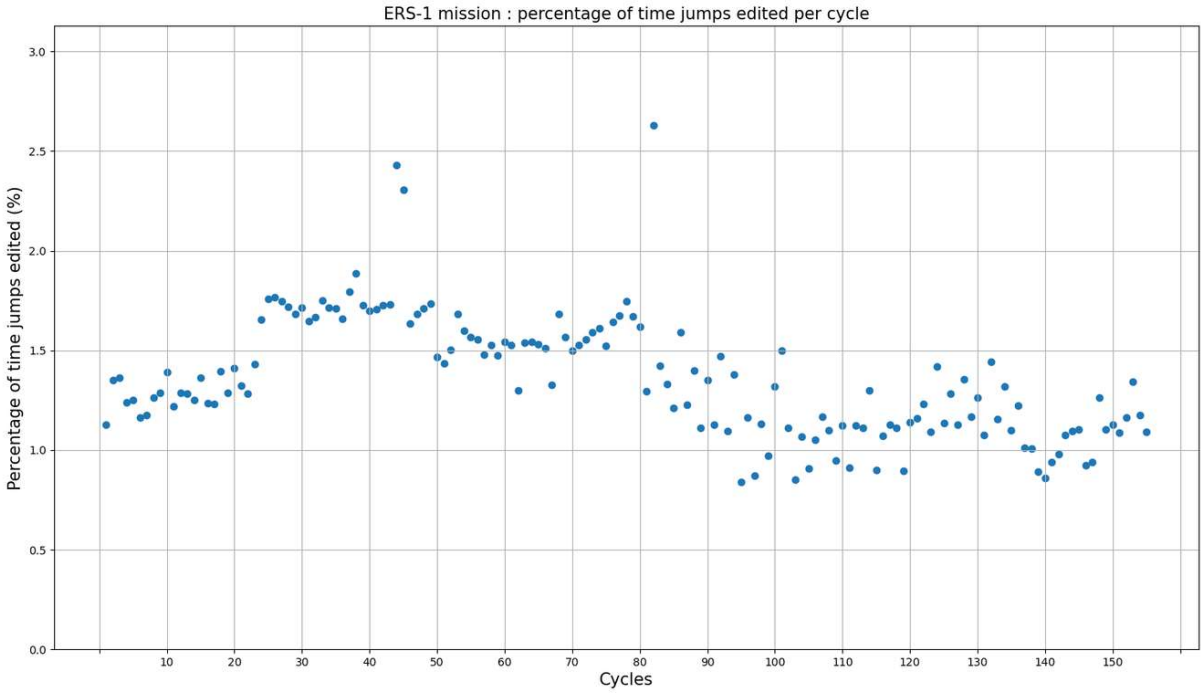

Figure 3-3 : Percentage of time jumps edited per cycle for ERS-1

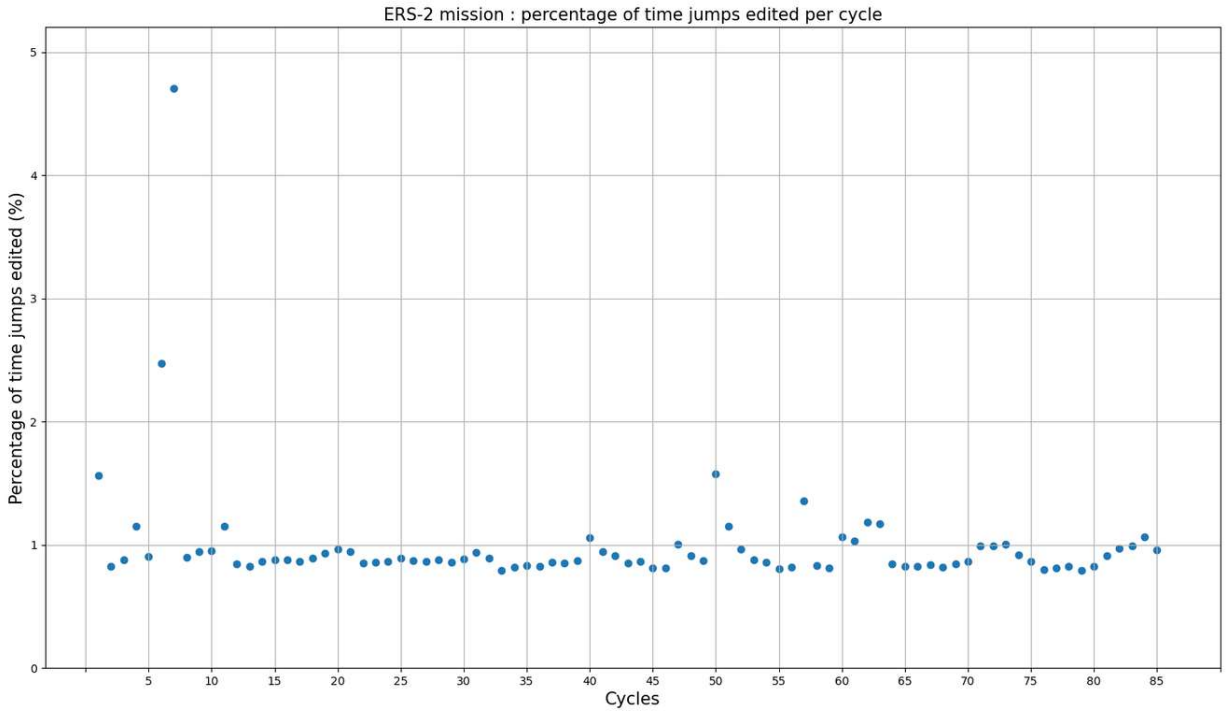

Figure 3-4 : Percentage of time jumps edited per cycle for ERS-2

For ERS-1 and ERS-2, approximately 1% of data are edited with this editing algorithm.

3.4 ERS REAPER Negative Waveforms

As explained in [D-1-02], one of the improvements of the ALT FDR product is the correction of the negative values found in the waveforms, due to a numerical overflow of the NetCDF field. The percentage of waveforms corrected have been computed for ERS-1 and ERS-2 for each cycle of data and can be found in Figure 3-5 and Figure 3-6.

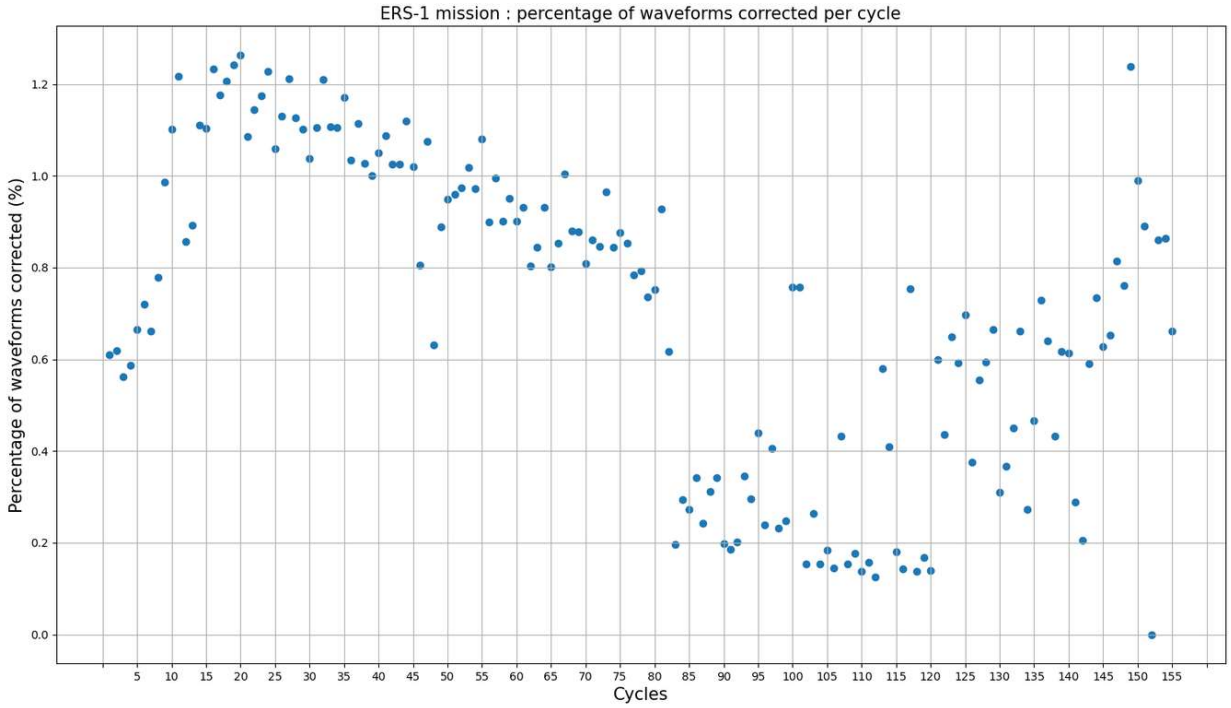

Figure 3-5 : Percentage of waveforms corrected per cycle for ERS-1

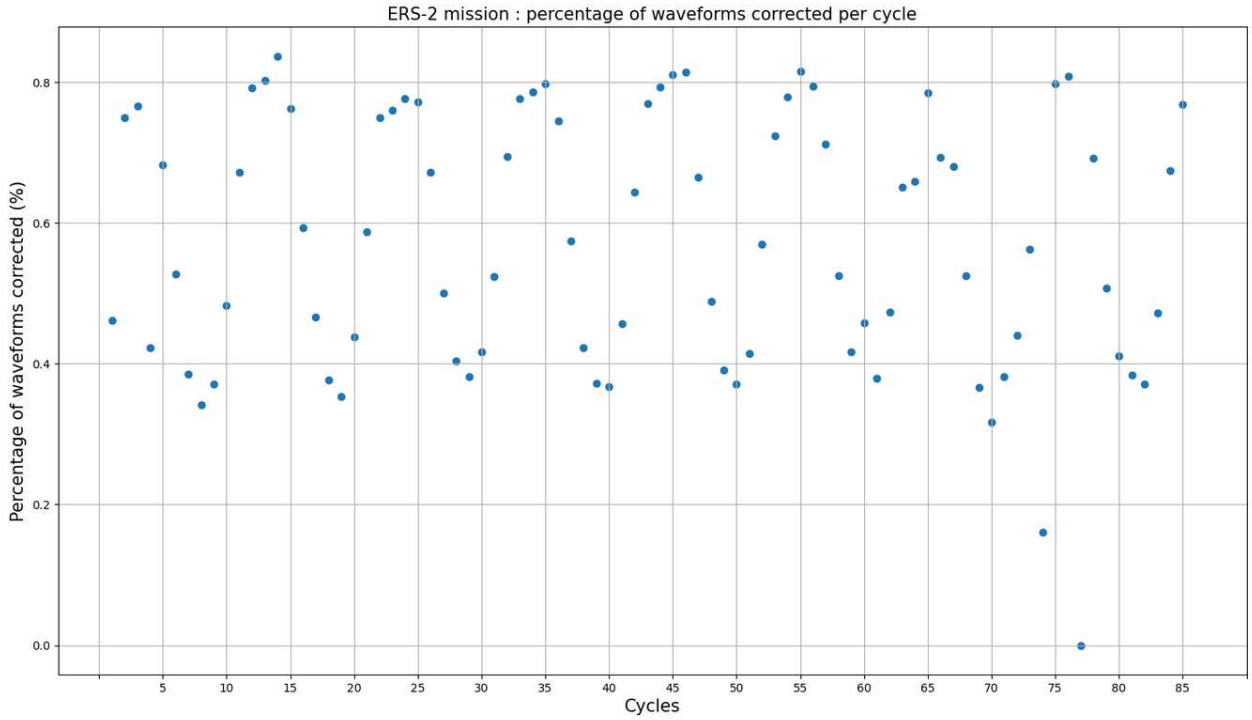

Figure 3-6 : Percentage of waveforms corrected per cycle for ERS-2

A seasonal signal can be observed on ERS-2 and can be interpreted as such: the overflow will happen for very energetic waveforms, usually found over specular areas such as sea-ice or rivers. The signal is therefore likely linked to the ratio of peaky waveforms evolving throughout the year.

This signal is not obvious for ERS-1: indeed, as opposed to ERS-2, the duration of the orbital cycle went from 3 days (up to cycle 82), to the classical 35-days and then 160 days, making it more difficult to see the annual signal on a plot using cycle number as x-axis.

3.5 Validation of the ENVISAT Waveform classification

For the ENVISAT classification, the development and validation have already been performed in the frame of ESA Sea Level CCI project ([**RD-4**]). This paper presents the "Development of an ENVISAT Altimetry Processor Providing Sea Level Continuity Between Open Ocean and Arctic Leads" that includes a detailed validation process over sea ice surfaces for sea level continuity (Leads identification).

This section aims at providing more results about the waveform classification.

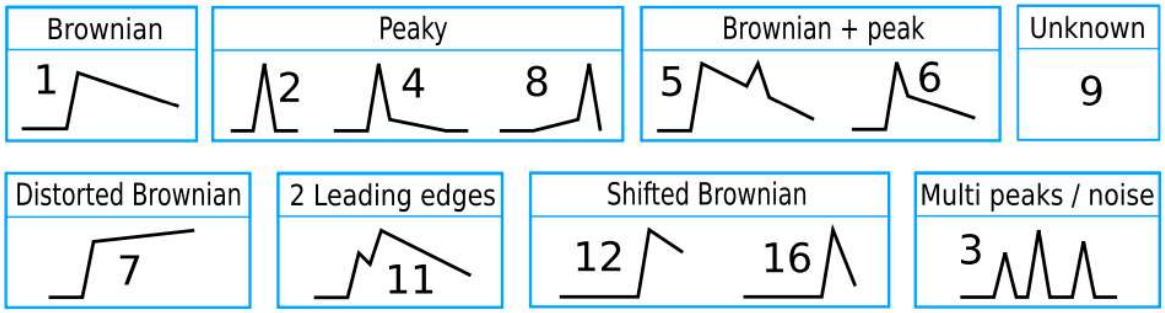

*Figure 3-7: List of class defined for ENVISAT. Images are from [**RD-4**].*

Mean waveforms for each class must be consistent with their definition in term of shape according to the learning phase. According to Figure 3-7 we plotted mean waveform for each class of the following dataset:

Classes	1	2	3	4	5	6	7	8	9	11	12	16
Effectives	1093	63	159	150	179	311	17	13	25	27	123	154
Percentages	44.8	2.58	6.52	6.15	7.34	12.75	0.7	0.53	5.25	1.1	5.04	6.3

Figure 3-8: Randomly picked waveform over passes 244, 293, 330 and 872 of cycle 14

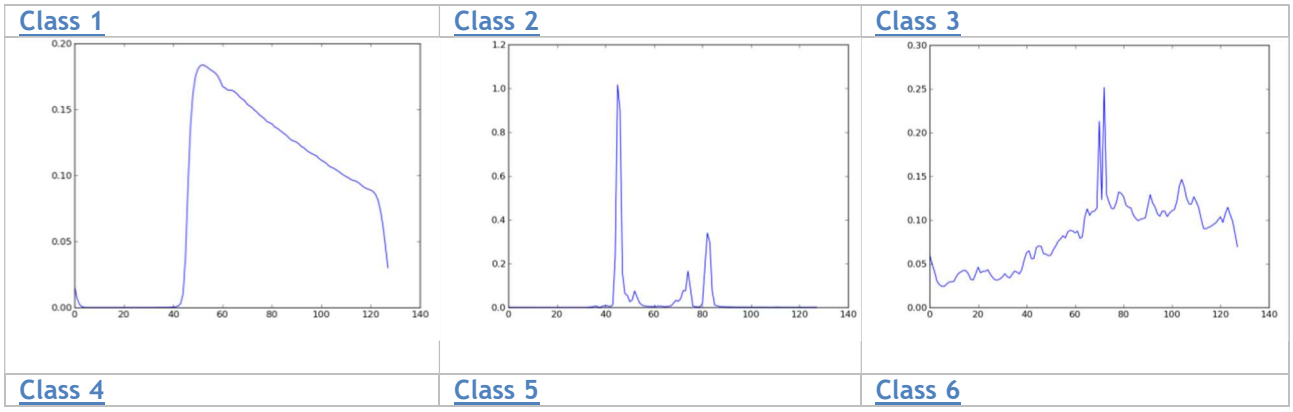

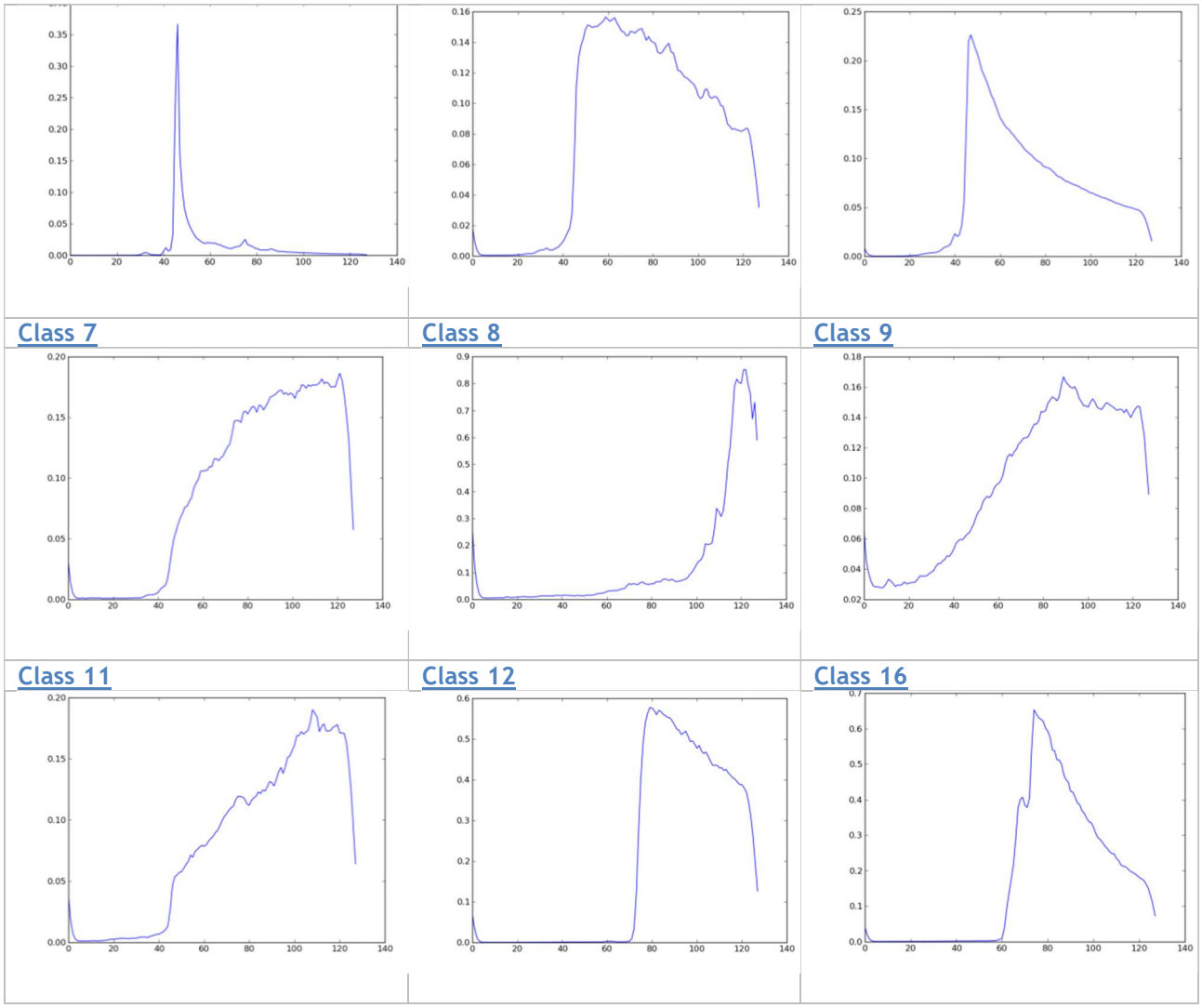

Here we find relevant to show the spatial distribution of the most important class over ocean which is class N°1 as illustrated in density plot in Figure 3-10. Indeed, the shape of class 1 is the most found over ocean as shown in Figure 3-9.

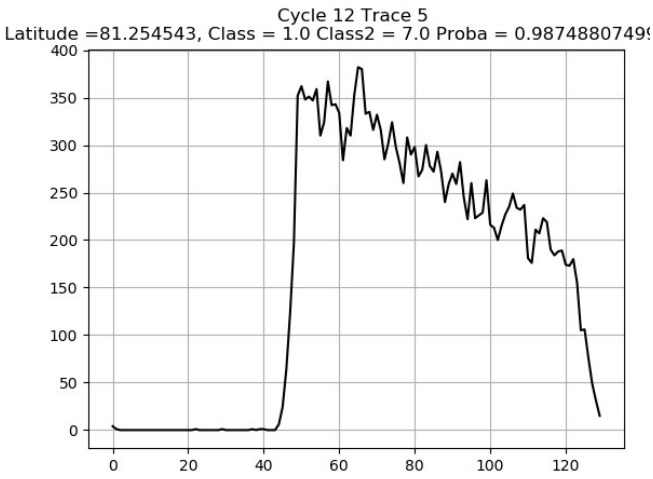

Figure 3-9: Example of class 1 waveform

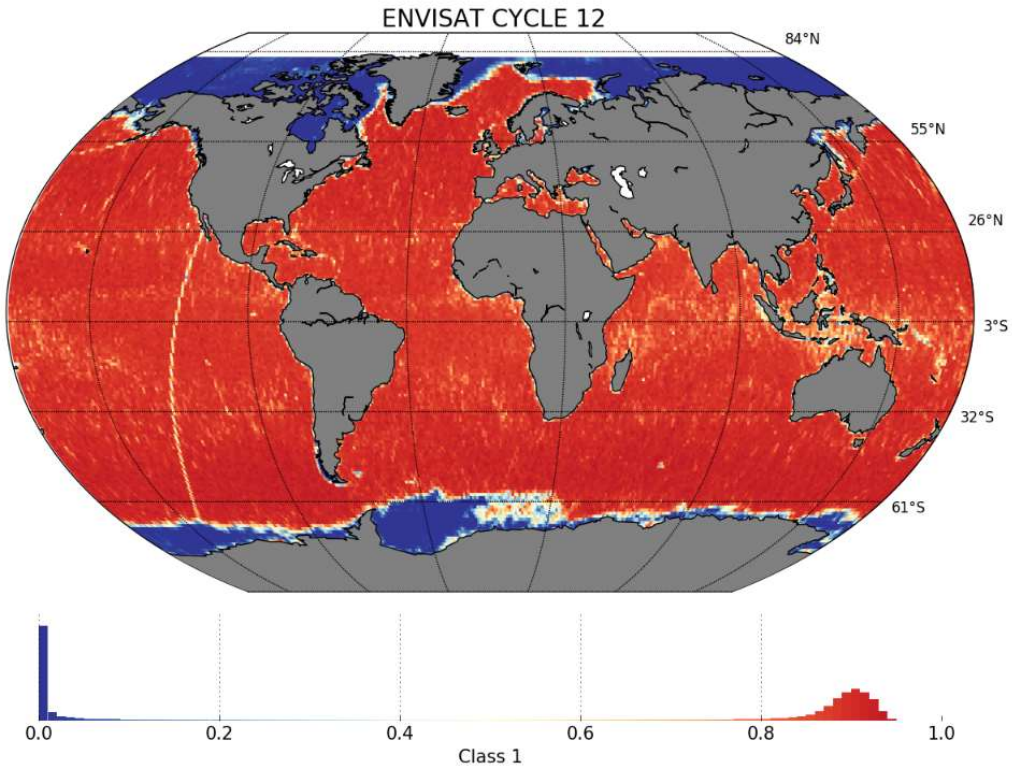

Figure 3-10: Density plot of class 1, main waveform shape over ocean.

On the contrary, we find peaky waveforms over sea ice and land regions as illustrated in Figure 3-11.

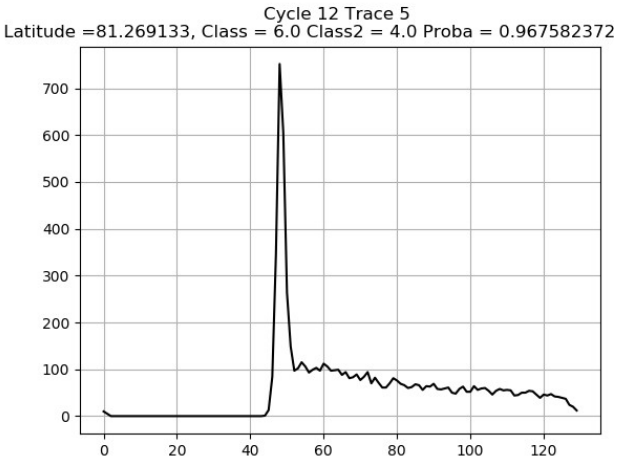

Figure 3-11:Peaky waveform predicted as class N°6

This is confirmed looking at polar density plots of the class 6 and 4 in Figure 3-12.

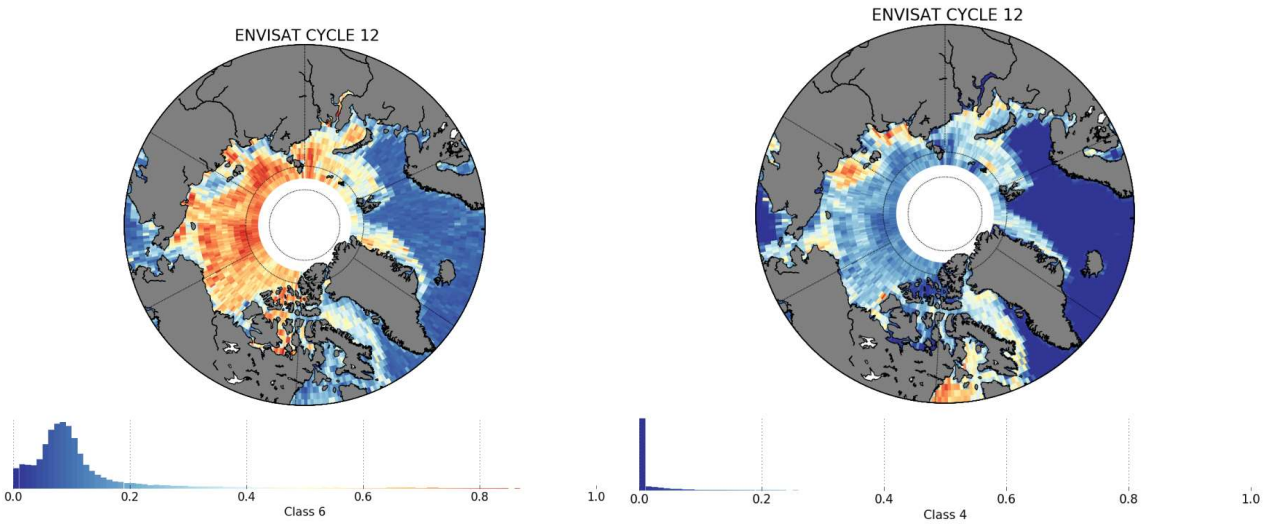

Figure 3-12: Density plots of class 4 and 6

3.6 Validation of the ERS Waveform classification

For both ERS1 and ERS2, we developed a new classifier. Indeed, we needed to define and train a new neural network for ERS waveforms. The first step was to collect waveforms from various overflown surfaces. This crucial step enables us to define a new and relevant list of classes for both ERS1 and ERS2. The resulting list of classes must correspond to all representative shapes that are encountered on the different surfaces. It is important to define a class for each echo shape of interest but also for all other waveforms numerous enough to impact the classifier. Even if they do not provide useful information for the user, their identification as a dedicated class number prevents the algorithm from misclassifying them as shapes of interest. In Figure 3-13 is presented an example of a waveform collected in south of the Mediterranean Sea near the coastline. This collection step is done manually and can take a long time. This was done over January 1996 for both ERS1 and ERS-2 (respectively cycle 8 and cycle 153).

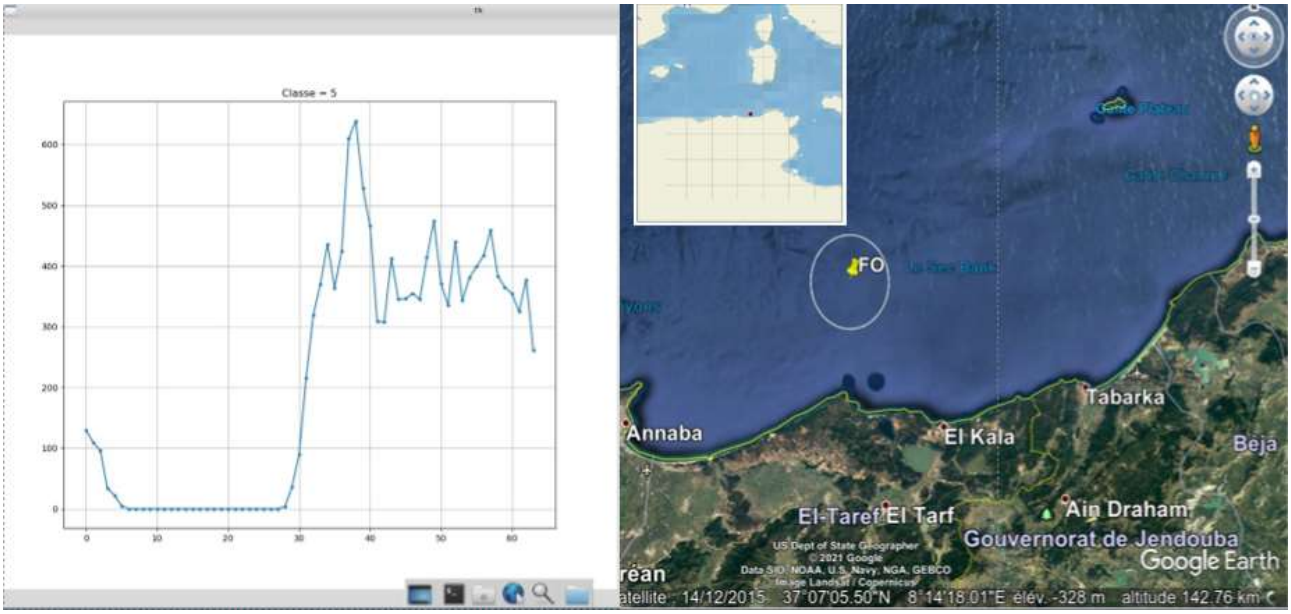

Figure 3-13 : Individual ERS-2 waveform picked up in coastal zone.

After collecting thousands of waveforms, we analysed the occurrence of each class. Figure 3-14 presents the class distribution of the collected dataset and we can clearly see that some classes are more significant than others.

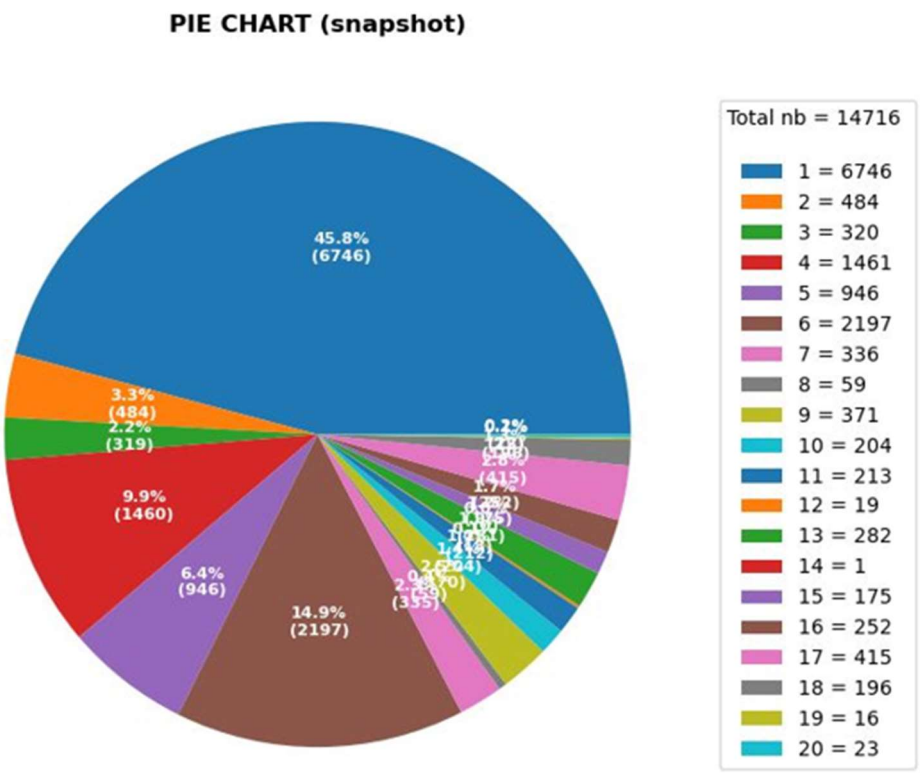

Figure 3-14 : Class labelling pie chart of the ERS collected dataset.

That way we determine only 15 relevant classes for ERS-1/-2 as detailed in Figure 3-15.

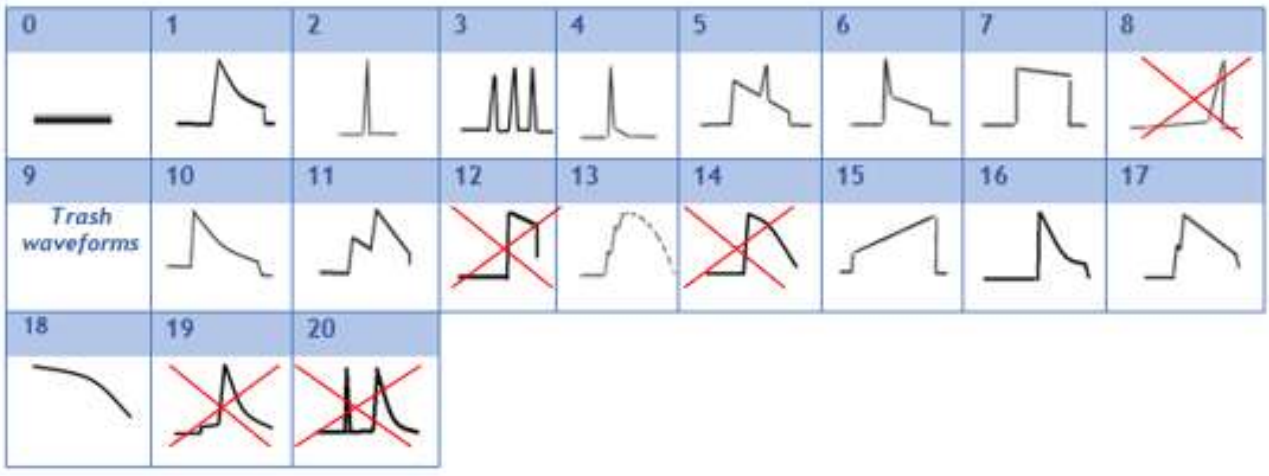

Figure 3-15 : List of class defined for ERS-1 and ERS-2

As well as for ENVISAT, we did not use the whole waveform as direct input in the neural network, but a set of geometrical parameters derived from the 64-sample radar waveform. That way we can avoid the curse of

dimensionality at the price of the determination of the best set of parameters regarding the performances and the goodness of the neural network. We found that the best performances were obtained with the following list of parameters:

- Slope of the leading edge, trailing edge, and thermal noise
- Amplitude of main peak on the trailing edge and the thermal noise
- Breakage flag on the leading edge
- Centre of gravity of the waveform
- Peakiness, kurtosis, and skewness
- Mean quadratic error between the waveform and the mean ocean shape.

This set of 11 parameters describes the main waveform shape varieties found on ERS. For instance, some parameter analyses power distribution in different regions of the waveform (slope, power statistic). Also, a flag is computed based on the leading-edge continuity to identify breakage as seen in Figure 3-16. Finally, a mean square error Is computed between the waveform and an averaged 64-samples waveform computed over open ocean (-50°<latitude<50° and distance to shoreline>20km).

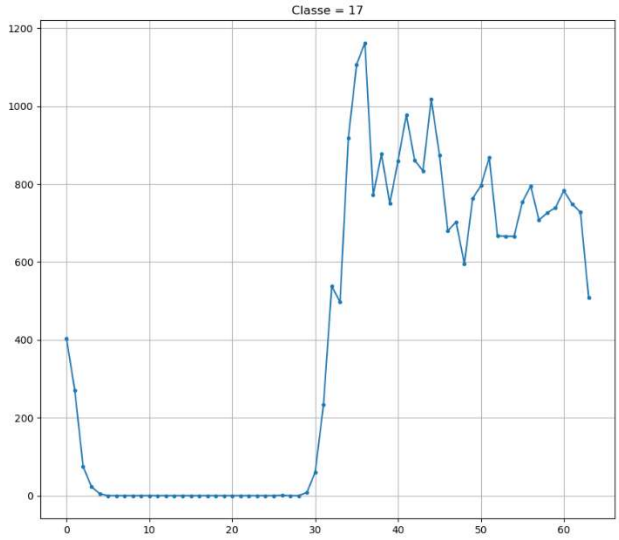

Figure 3-16: Example of waveform classified as N°17 due to a breakage in the leading edge.

Also, the best results were obtained with the following neural network structure [11-25-15]: 11 neurons in input layer, 25 neurons in the hidden layer, 15 output neurons referring to class labelling previously defined). To assess the performance of the neural network the dataset was divided into two subsets for the training and testing (respectively 75% and 25% of the original dataset). We ensure that the two datasets are strictly independent so that the result are not biased. Table 1 presents the distribution of each class in both the training and test dataset.

Classes	1	2	3	4	5	6	7	9	10	11	13	15	16	17	18
Nb base app(tot=10616)	4723	363	240	1096	710	1648	252	279	153	160	212	132	189	312	147
Nb base test (tot=3982)	2023	121	80	365	236	549	84	92	51	53	70	43	63	103	49

Table 2: Distribution of each class in the training and test datasets.

The learning efficiency is bound to many parameters. The R *nnet* function used here to compute the network takes the number of neurons as input as well as a *decay* parameter which reduce the learning rate and prevent the learning from overfitting. After testing different couples, decay=1e-12 for 25 neurons in the hidden layer seems to be the best setting. For that, we looked at the double-entry Table 3 which sums up the testing of the neural network model as predicted classes versus expected classes from the hand-made test dataset. In this way we can fully understand the performances of the *nnet* model in terms of error and misclassification. In Table 2 we computed the error corresponding to incorrect classification with respect to the expected classes defined in the test dataset.

Indeed, when building both learning and test waveform databases, we introduced ambiguities according to the variability within each class. For instance, an increase of the trailing edge slope of an ocean echo swaps the predicted class from 1 to 7 at some point. Since the reality is complex, the learning test here reports it as ambiguities errors in the classification table results. Finally, we obtain an 4.6% misclassification – raw – error for the main class 1 meaning that more than 95% from the test dataset are correctly classified. The other classes are described in Table 2.

	1	2	3	4	5	6	7	9	10	11	13	15	16	17	18
1	1929	0	0	0	63	26	32	0	0	1	2	0	2	33	0
2	0	106	0	21	0	0	0	0	0	0	0	0	0	0	0
3	0	0	48	3	4	2	0	3	1	7	0	2	0	0	0
4	0	15	11	321	0	19	0	0	0	0	0	0	6	0	0
5	30	0	2	0	136	7	8	0	1	12	10	0	2	7	0
6	34	0	0	19	10	485	0	0	2	1	1	0	6	1	0
7	17	0	0	0	6	1	41	0	1	0	4	0	0	0	0
9	0	0	7	0	0	0	0	53	2	4	3	7	1	0	5
10	0	0	3	0	0	3	0	2	40	0	4	0	0	0	0
11	0	0	3	0	5	0	0	3	0	12	0	1	3	0	0
13	1	0	1	0	5	0	0	6	2	11	37	1	0	2	0
15	0	0	1	0	0	0	0	15	2	3	3	32	0	0	0
16	3	0	3	1	3	6	0	0	0	1	1	0	43	1	0
17	9	0	1	0	4	0	3	0	0	1	5	0	0	59	0
18	0	0	0	0	0	0	0	10	0	0	0	0	0	0	44

Table 1 : Class prediction with the test dataset

Class	1	2	3	4	5	6	7	9	10	11	13	15	16	17	18
Error (%)	4.6	12.4	40	12	42	11.6	51.2	42.3	21.6	77.4	47.1	25.6	31.7	42.7	10.2

Table 2 : Table of errors for each class

Even if the performances of the network have been evaluated with representative datasets, it is necessary to look at the link between the classification and its geophysical significance. Looking at geographical distributions that are good indicators of the classification quality.

Starting with global scale analysis we paid attention to the class distribution over different surfaces (ocean, coastal, high latitude ocean, land, wet land, sea ice). In addition, we looked at mean waveforms for each class

that must be consistent with their definition in term of shape according to the learning phase. Note that the validation process for the waveform classification does not need to be performed for the whole time series of ERS. The assessment on real data is presented in the following.

Table 3: Table of density maps for each predicted class over 1 cycle of ERS-2 data.

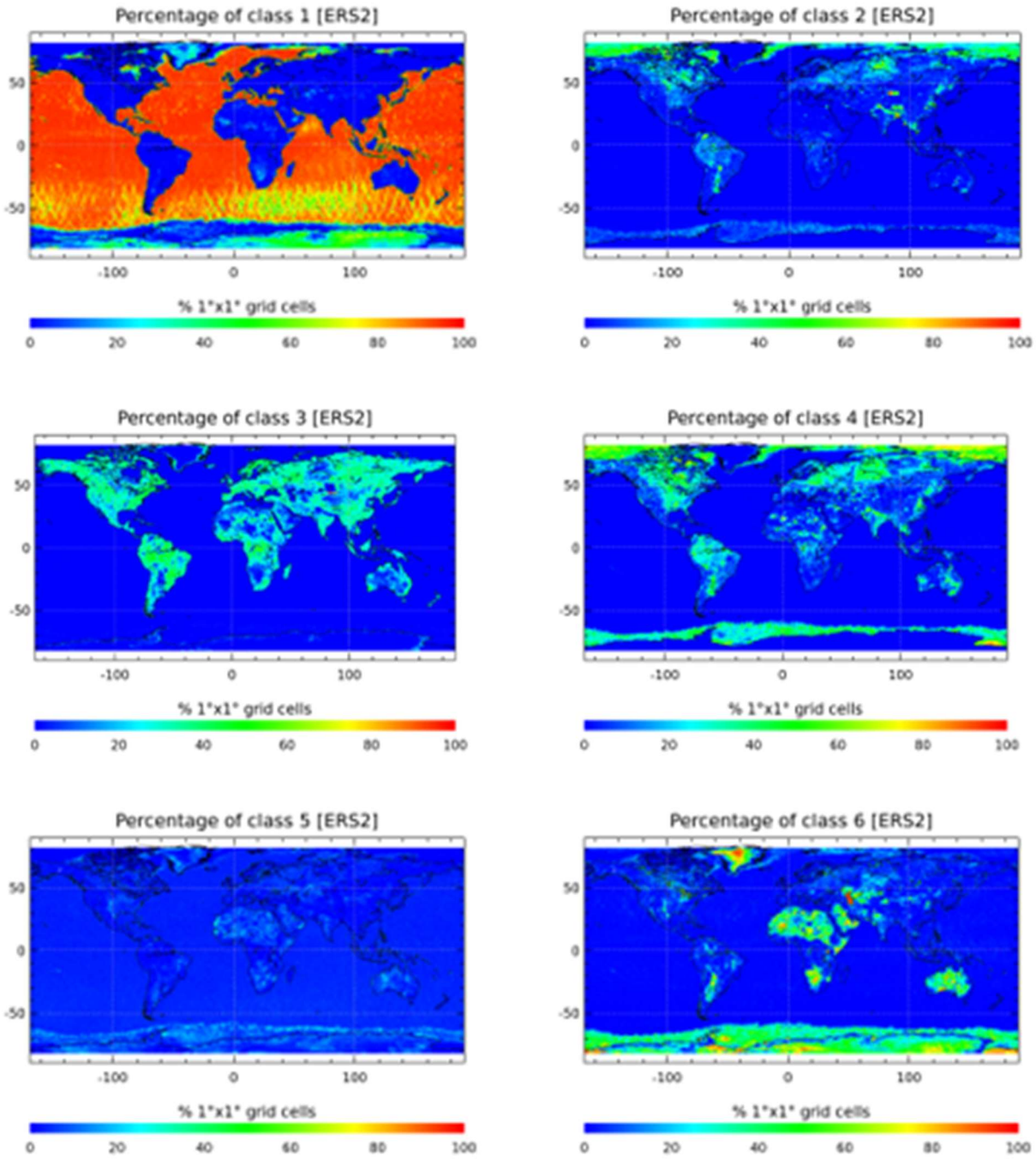

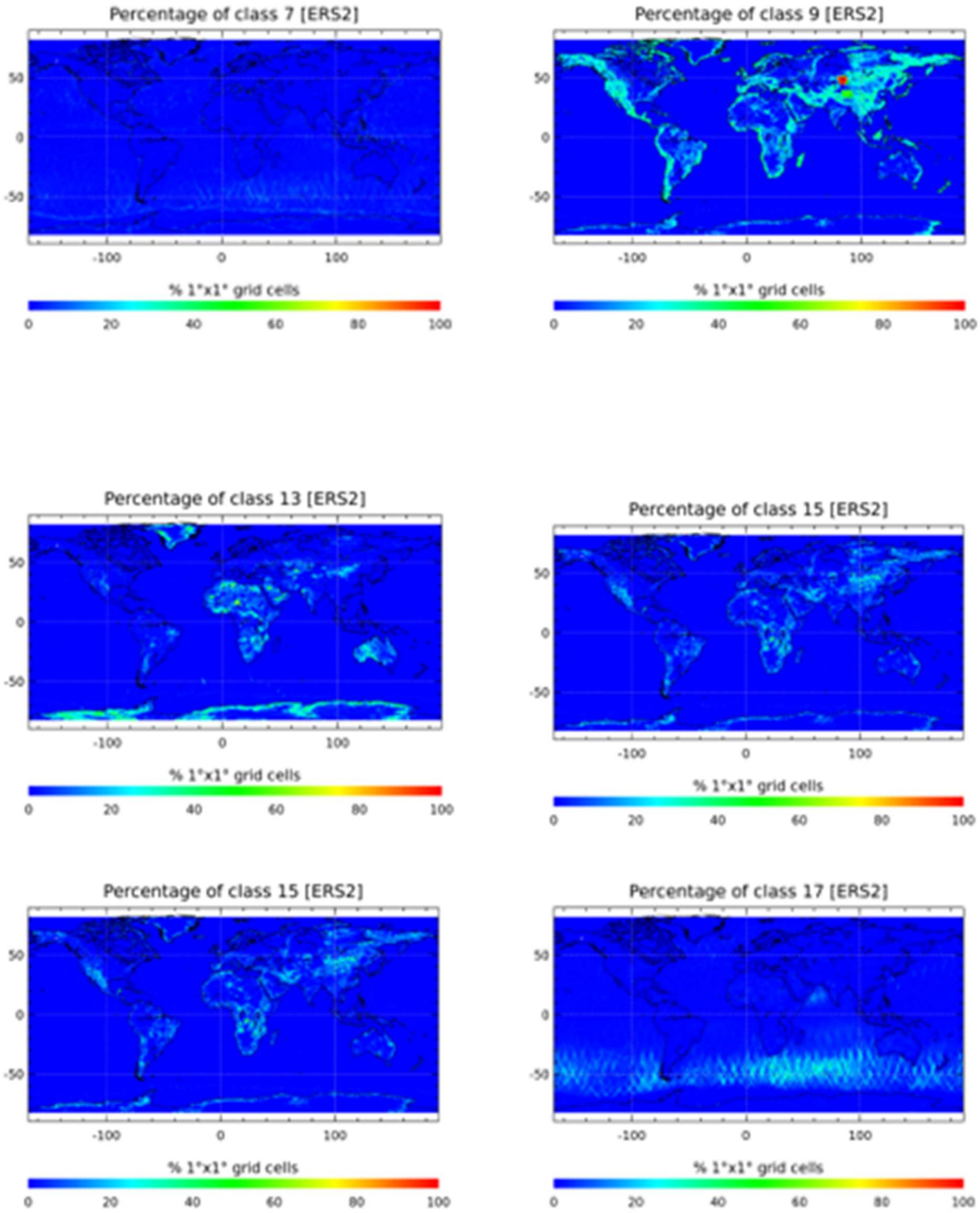

According to Table 3 and as expected, class 1 (brow-like shape) is the main predicted class over open-ocean with also class 17 (brown-like shape with brake on the leading edge) over the circumpolar current region. In addition, Class 2, 4 and 6 are peaky echo shapes and are found in polar regions over specular ice-covered areas which is coherent. Other class maybe found over inland water as for 3 (multi-peaks) or 9 (very complex and unknown shape). From open-ocean to coastal regions, Figure 3-17 clearly shows class changes as the satellite is approaching the coastline, illustrating the impact of sea-state and shoreline in these areas on the altimeter waveform shape. Class definition is the same for Jason-3 making it comparable with ERS results to

analyse consistencies and physical significance of the predicted classes through this graph. Through this global analysis over 1 cycle of data, we were able to validate the goodness of the new classification algorithm developed for ERS-1 and ERS-2 in this project.1e-12

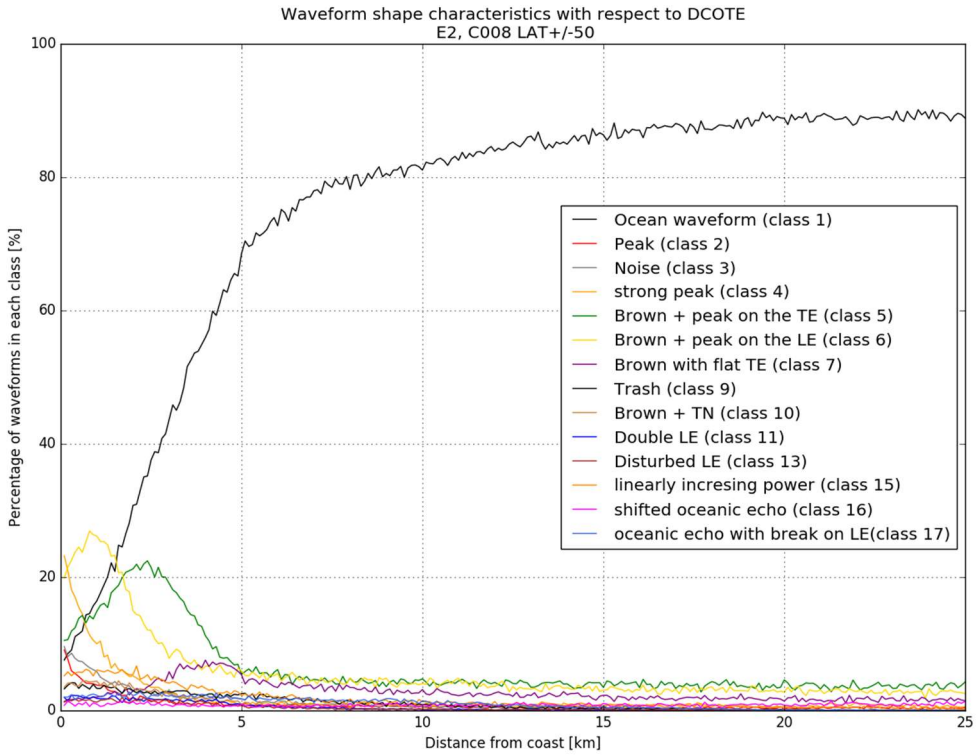

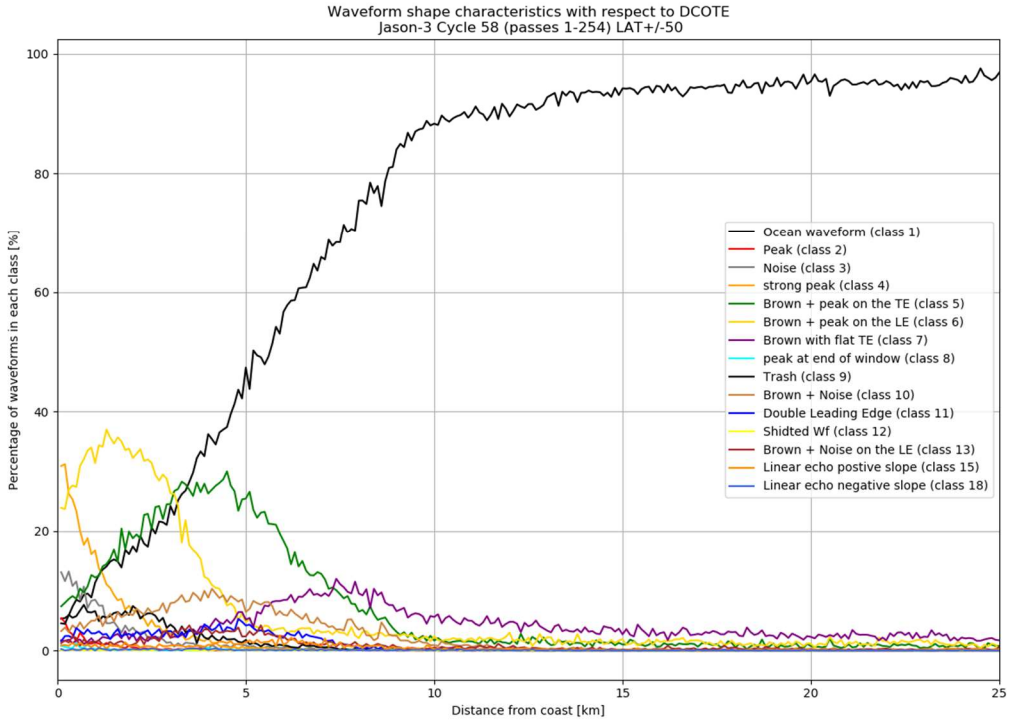

Figure 3-17: Percentage of each class as function of the distance to coastline. Top is for ERS-2 cycle 8 and bottom is obtained for Jason-3.

3.7 Validation of the Low Pass Filters (LPF)

The CAL2 mode measures the altimeter transfer function (Low Pass Filter, LPF). For each LPF, we extract 3 slopes values (right and left side and full window). That way, we can monitor the shape evolution over time. In the ALT FDR products, LPF signals are provided for ENVISAT and ERS as these characterize the waveforms shape for each altimeter.

3.7.1 ERS

ERS-1

For ERS, calibrations data are recovered from the Level-0 auxiliary data. The structure is described in Table 4 extracted from [**RD-2**]. In total 266 files for ERS-1 and 1979 files for ERS-2 have been recovered in the frame of the project.

Column	Description	Code name	Unit	Byte length	Data type
1	IF mask reference time	if_mask_time	MJD	8	double
2	64 IF Correction Mask samples	if_corr_mask_samp	FFT units	8	double
3	Quality Flag	qua_flag		2	us
4	Number of averaged spectra	num_ave_spec		2	us

Table 4 : IF masks output from file type E1(2)_TEST_AUX_IFFXXX_YYYYMMDDHHT_ YYYYMMDDHH_0001.DBL

According to Table 4, the LPF 64-samples are obtained by averaging thousands of individual calibration measurements so that the noise is reduced. Since no additional correction has been applied in the frame of this project, only slope estimation is presented to ensure consistency with the REAPER quality assessment report. See [**RD-5**] for more information. Slope is computed over 3 different window sizes:

- Left slope: [0-31]
- Right slope: [32-63]
- Main slope: [0-64]

Also, quality flag output is “valid” when equal to 0.

- First measurement: 1992/03/07

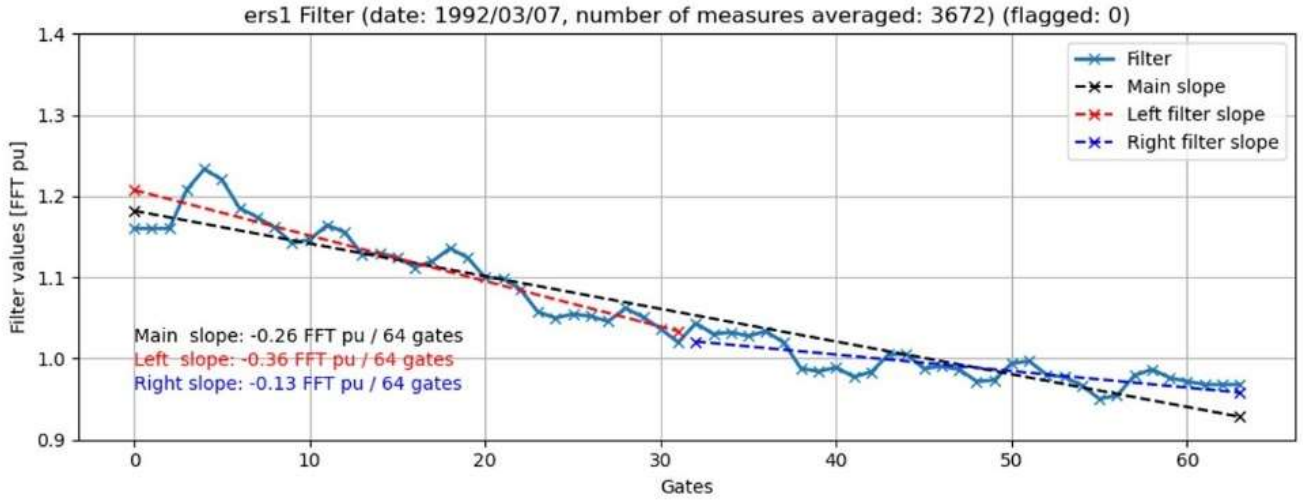

- Last measurement: 1999/06/23

Figure 3-18 : Example of ERS-1 LPF at the beginning of the mission

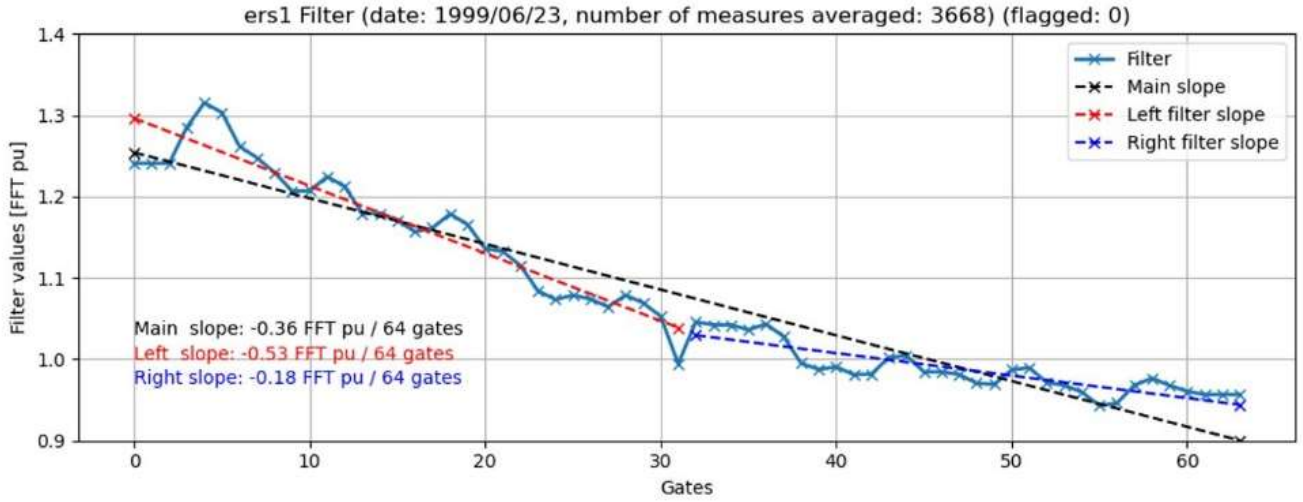

Figure 3-19 : Example of ERS-1 LPF at the end of the mission

In addition, it is important to monitor the long-term evolution (LTM) of the slope's parameters over the lifetime of the mission to see any change in the shape that would impact the resulting waveform signal over time.

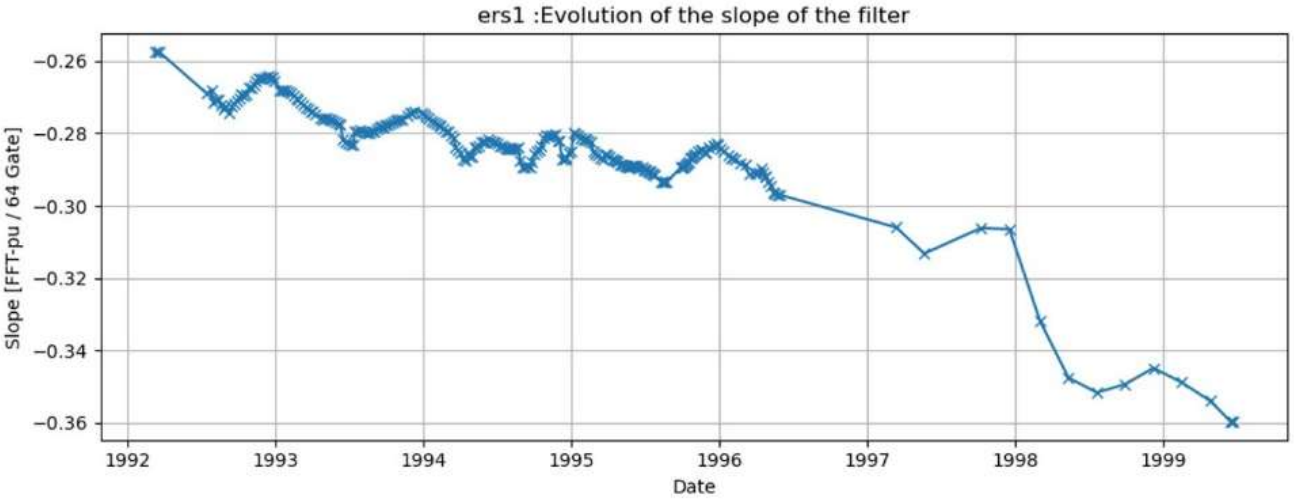

Figure 3-20 : Evolution of the total slope of the LPF throughout the whole ERS-1 mission.

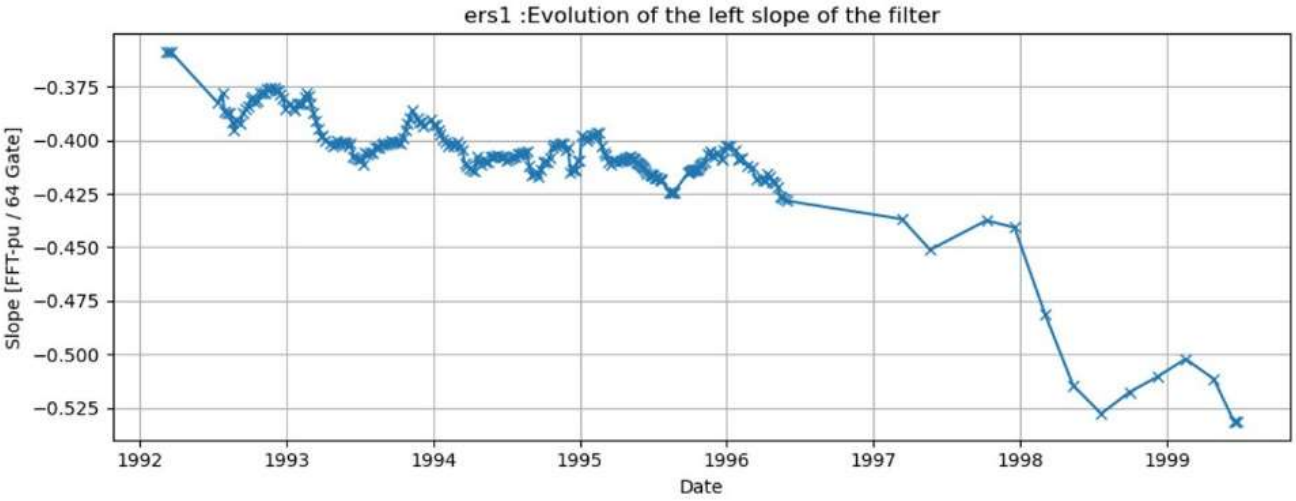

Figure 3-21 : Evolution of the left slope of the LPF throughout the whole ERS-1 mission.

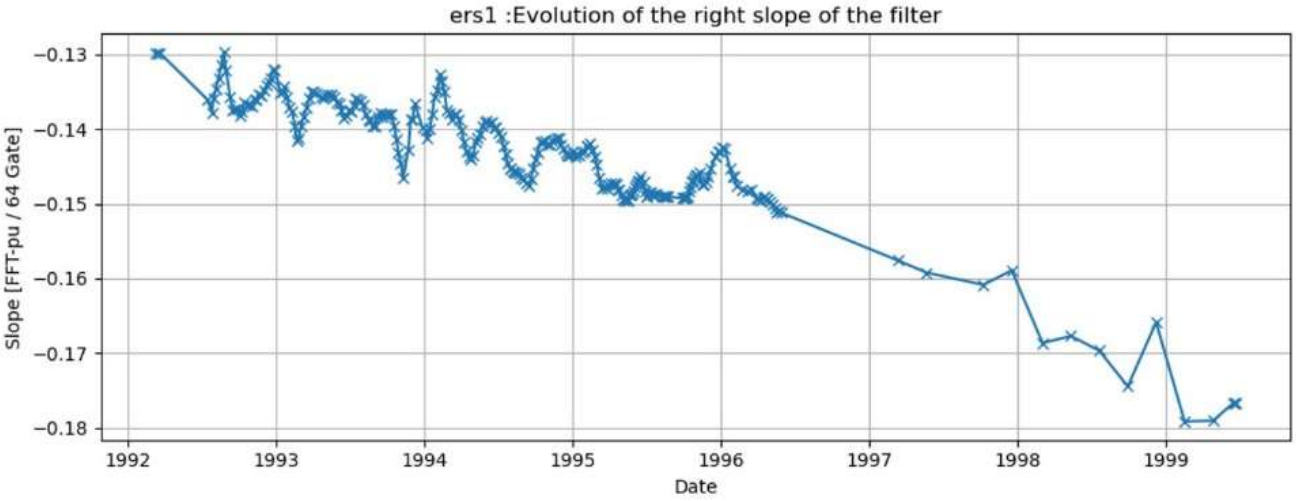

Figure 3-22 : Evolution of the right slope of the LPF throughout the whole ERS-1 mission.

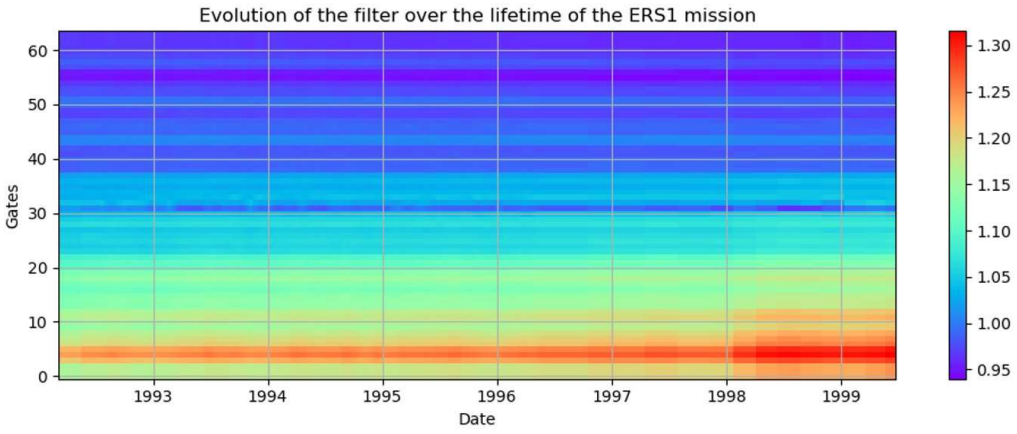

Figure 3-23 : Evolution of the whole LPF over the lifetime of ERS-1

ERS-2

Like ERS-1, the same analysis has been performed for ERS-2.

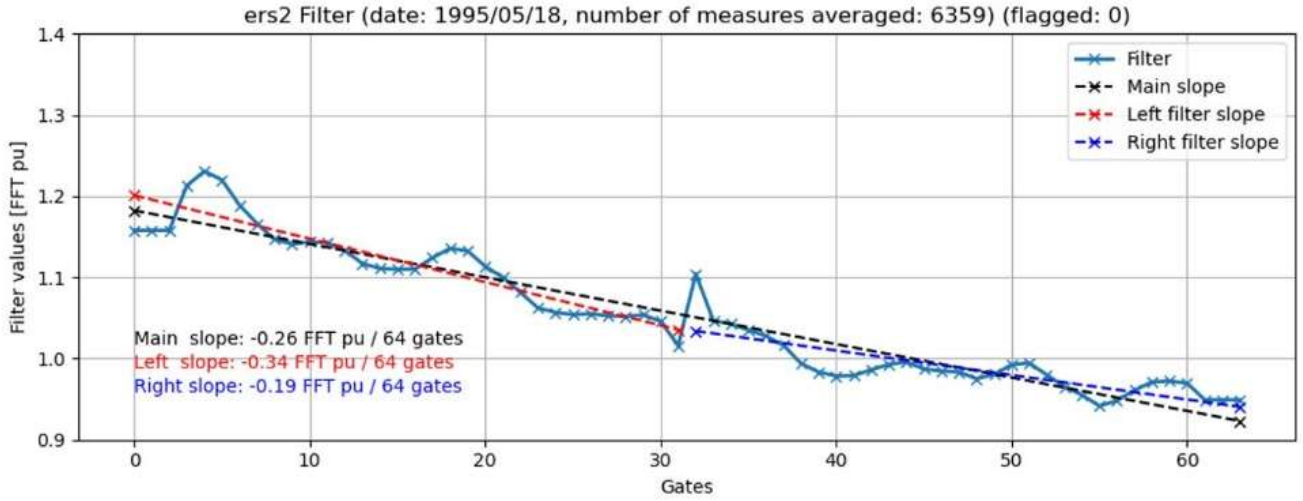

Figure 3-24 : Example of ERS-2 LPF at the beginning of the mission

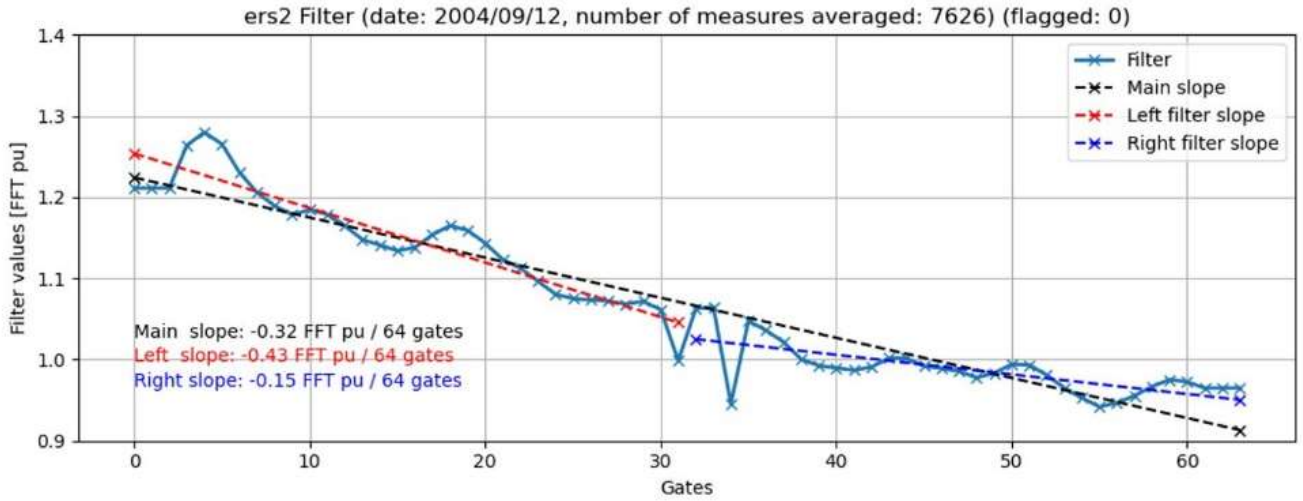

Figure 3-25 : Example of ERS-2 LPF at the end of the mission

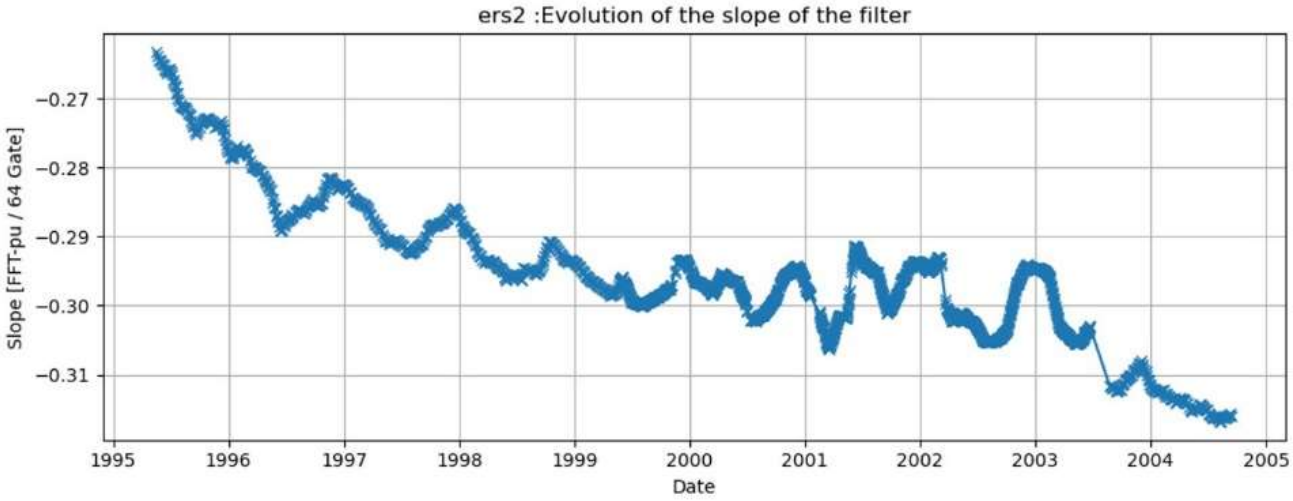

Figure 3-26 : : Evolution of the total slope of the LPF throughout the whole ERS-2 mission.

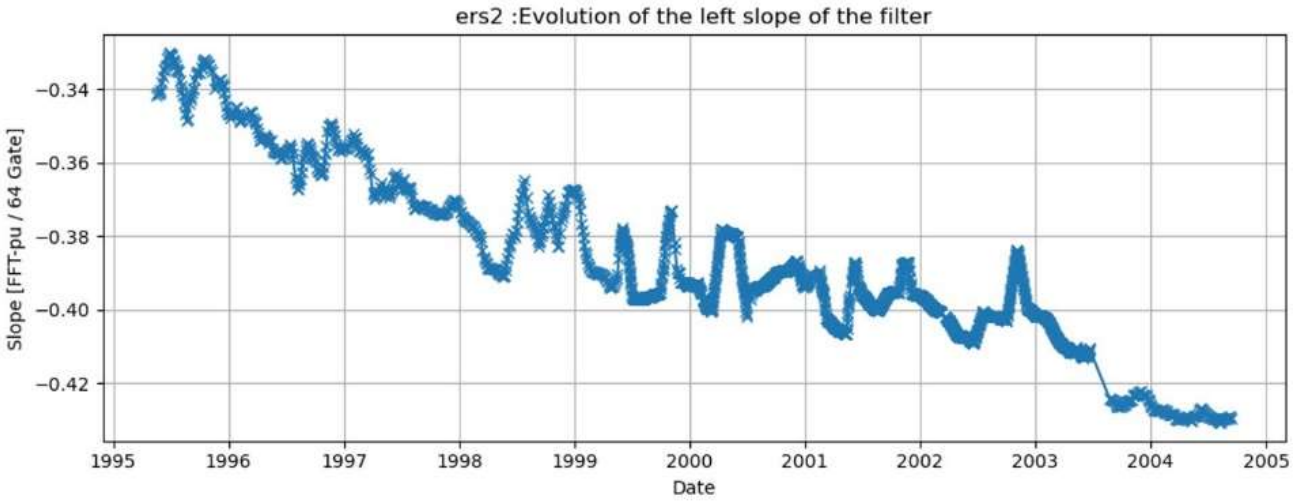

Figure 3-27 : Evolution of the left slope of the LPF throughout the whole ERS-2 mission.

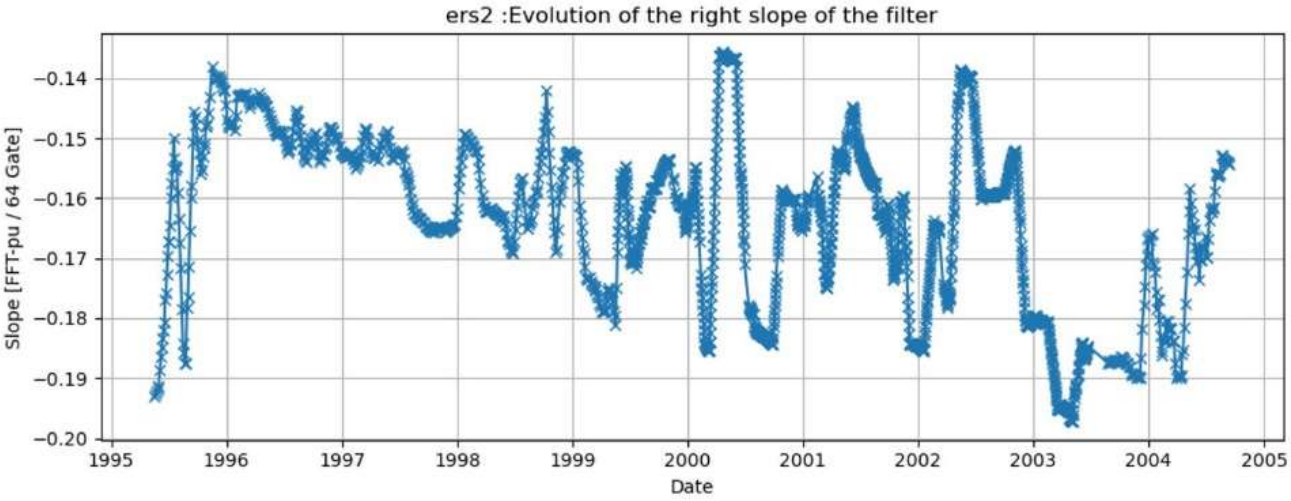

Figure 3-28 : Evolution of the right slope of the LPF throughout the whole ERS-2 mission.

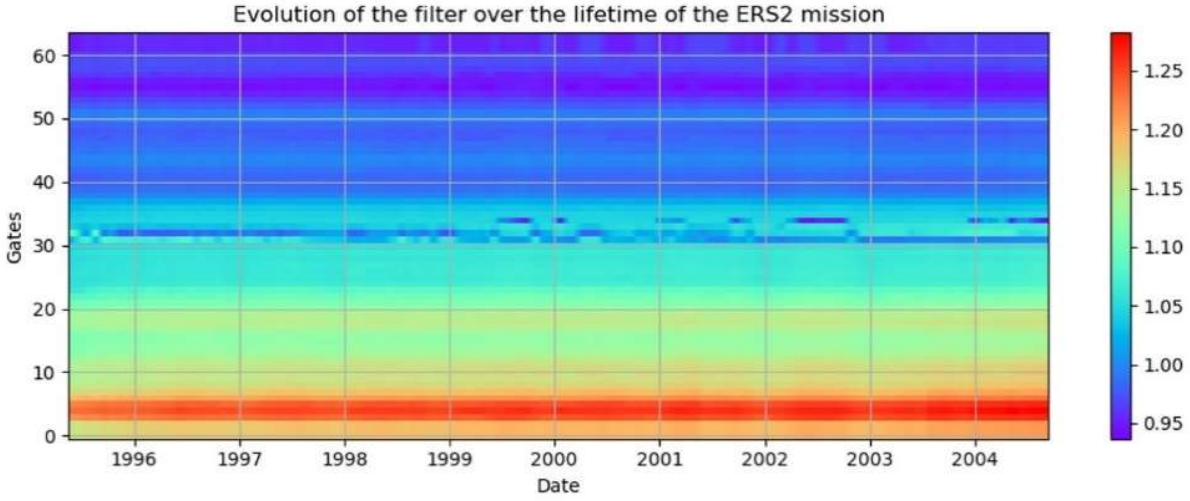

Figure 3-29 : Evolution of the whole LPF over the lifetime of ERS-2

3.7.2 ENVISAT

The IF Mask (or LPF) data file is used to correct the amplitude of the waveform samples for the instrument IF filter shape. The LPF can be derived on-ground or in-flight. Since it was decided to switch the RA2 instrument to its B-Side between the 15th of May 2006 and 21st June 2006, one LPF has been recovered during that time. Indeed there is no reason that both sides A & B should have strictly the same in-flight instrumental behaviour, hence calibration data are also provided during Side B operational time.

ENVISAT LPF data have been recovered from the original RA2_IFF_AXV files.

102 files covering from 2002 to 2012 are analysed in this section.

In the ALT FDR, the 20Hz waveforms are already corrected from the Low-Pass Filter. To ensure data preservation, the low pass filter values are provided in the product in a dedicated field (see [D-1-01] [D-1-02] for more information). For each data pass, the corresponding filter is available. In this section some filter stability analysis is detailed.

Here we present examples of 128-bins filter values for specific dates:

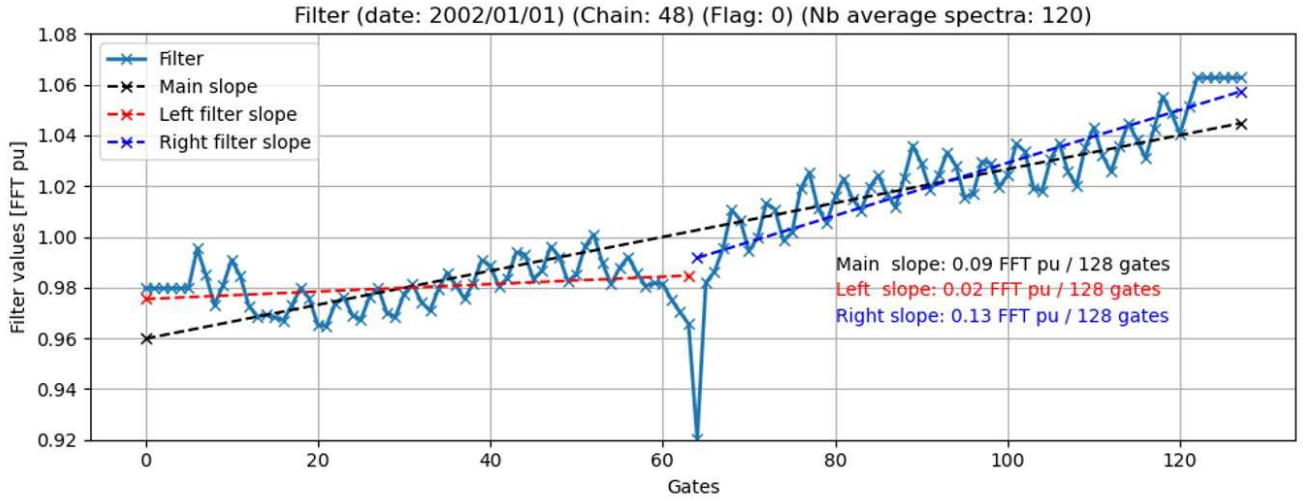

Figure 3-30 : First ENVISAT Low-Pass-Filter (chain A on 01/01/2002)

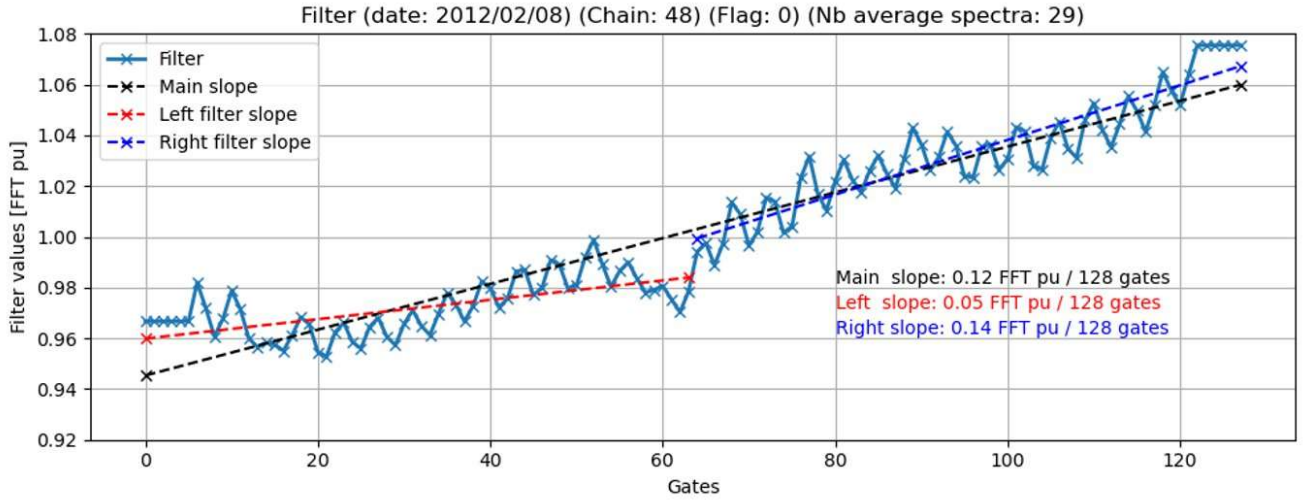

Figure 3-31 : Last ENVISAT Low-Pass-Filter (chain A on 08/02/2012)

On each LPF, slopes have been computed for monitoring the evolution of the LPF shape over time.

- Total slope: [0-127]
- Left slope: [0-63]
- Right slope: [64-127]

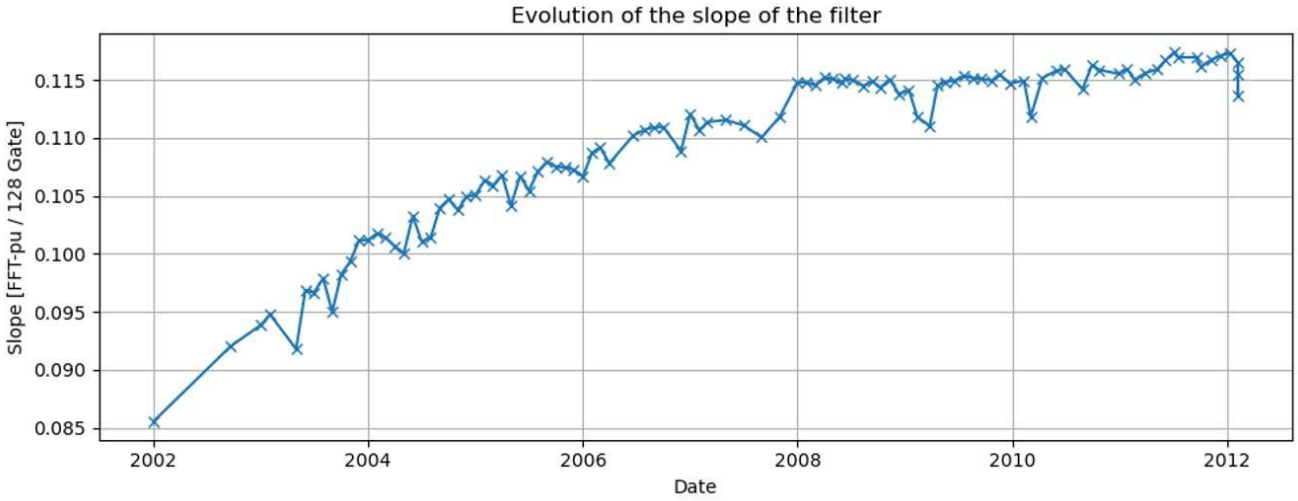

Figure 3-32 : Evolution of the total slope of the LPF throughout the whole ENVISAT mission

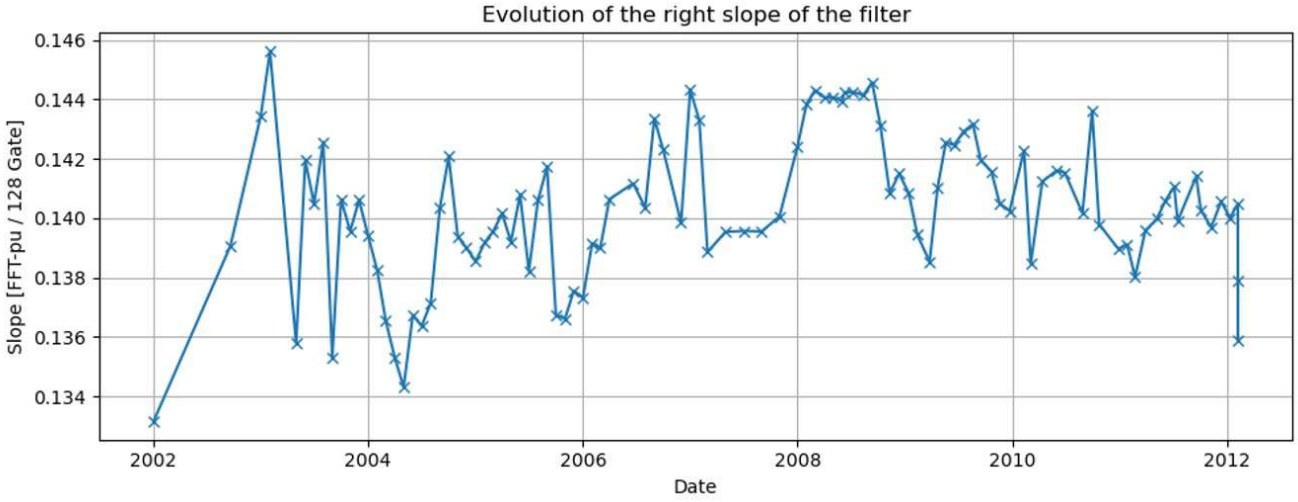

Figure 3-33 : Evolution of the right slope of the LPF throughout the whole ENVISAT mission

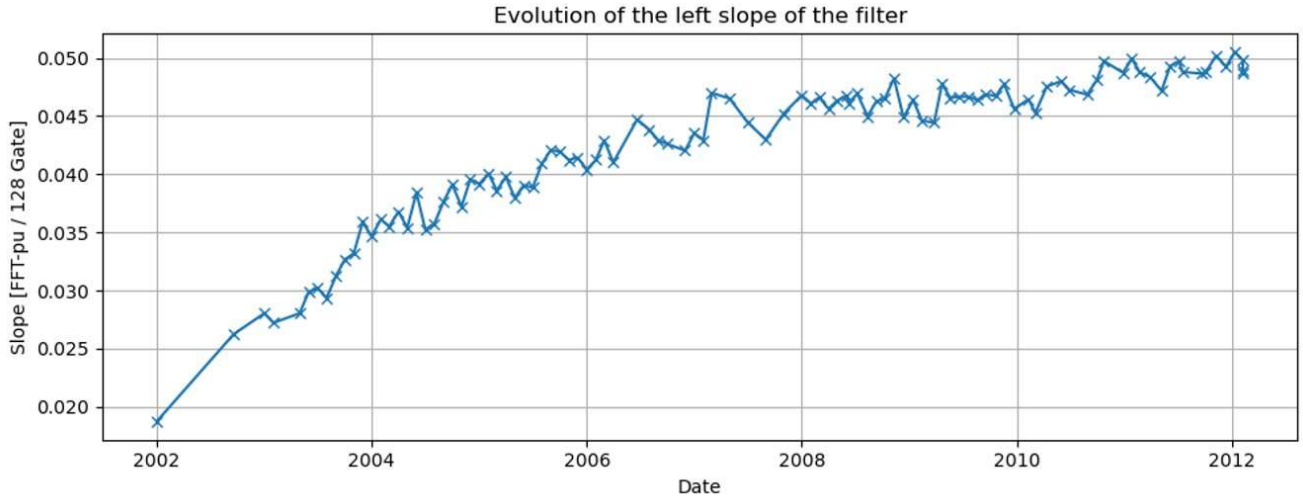

Figure 3-34 : Evolution of the left slope of the LPF throughout the whole ENVISAT mission

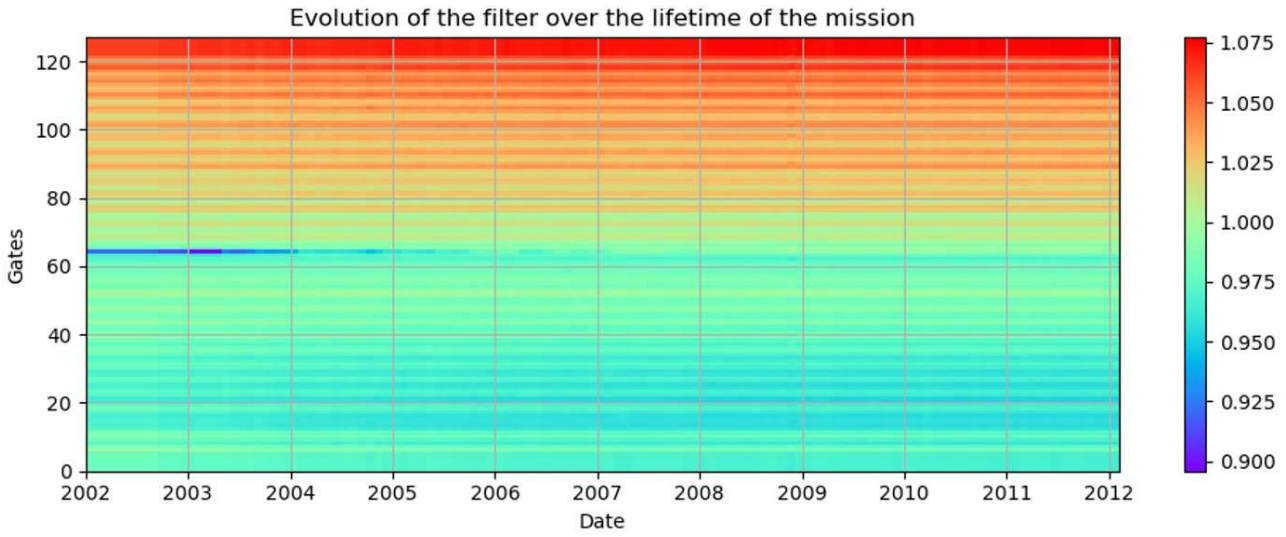

Figure 3-35 : Evolution of the LPF throughout the whole ENVISAT mission

Figure 3-35 shows that the LPF is quite stable throughout the lifespan of the ENVISAT mission. One can notice that for the first two years, a spike is clearly visible in gate 64. This spurious is regularly found in low-pass filters and is the consequence of the attenuation steps used: the filter does not have enough power. As seen on Figure 3-35 , it has been corrected later during the mission.

One can wonder about the effect of this spurious on the data quality. In the frame of this project, a few tests have been performed to ensure that this spurious does not affect data quality.

Impact on the waveforms

Figure 3-36 shows the strong impact on waveforms of the spurious at gate 64 at the beginning of the mission, which fades away later during the mission. This spurious is the consequence of the calibration sequence itself

(not enough power during the calibration), and therefore is not a real signal. As it is not real signal, when the waveforms are corrected from the Low-Pass filter, it artificially changes the amplitude of the echo at gate 64.

To see this effect, waveforms have been selected on cycle 14 (17/02/2003 to 24/03/2003) which is the period when the spike is the strongest, and cycle 50 (31/07/2006 to 04/09-2006) when the spike is the lowest. Waveforms have been selected as such to average over similar echoes:

- Waveform class = 1
- 2.1 < SWH Adaptive < 2.9 m
- 0.55m < Epoch Adaptive < 0.70 m

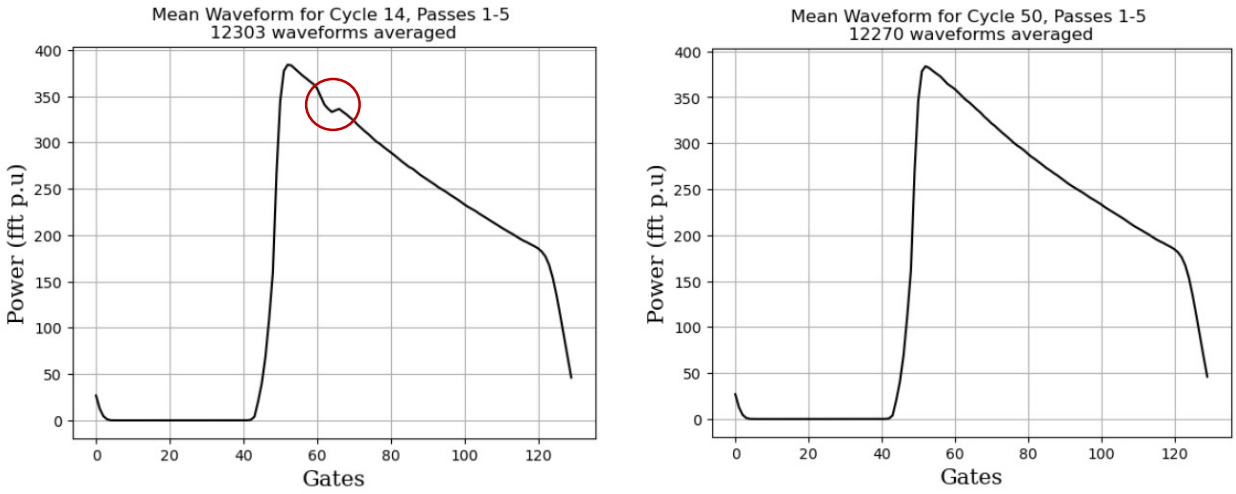

Figure 3-36 : Impact of the spurious on average waveforms for Cycle 14 (left, affected) and Cycle 50 (right, unaffected)

Figure 3-36 shows indeed that at the beginning of the mission, the spurious is visible on the waveforms and artificially lowers the signal around gate 64. As expected, it is no longer visible later during the mission when the spike is much lower.

Impact on the retracked data

Simulations were performed using different LPF arrays and this spurious shows no impact on geophysical estimates.

3.8 Validation of the ENVISAT PTR data

In the frame of this project, a new Adaptive algorithm has been developed to process ENVISAT waveforms. For that matter, the retracking needs a numerical PTR to perform the Adaptive model convolution. The PTR signal is derived from the instrumental Level-0 data and reconstructed based on a new averaging procedure to ensure the best performances in term of noise and accuracy. For that matter, the retracking needs a numerical PTR to perform the Adaptive model convolution. The PTR signal is derived from the instrumental Level-0 data and reconstructed based on a new averaging procedure to ensure the best performances in term of noise and accuracy. Although only Ku-band are used by the retracking, S-band PTR are presented here as they are derived and provided through the same processing scheme. Inputs are the Level-0 from v2.1 reprocessing. According to [**RD-3**] individual PTR waveforms comes as follows:

0	1	2	3	4	5	6	7	8	9	10	11	12	13	14	15
Spare (6 bits)									AGC CAL				AGC CAL		
spare (8 bits)									Datation PTR (8 bits)						
Datation PTR															
Datation PTR															
PTR 1st I/Q sample															
.....															
PTR 128 I/Q sample															
spare (1 byte)									Cal Band id						

Tableau 1: Data structure for PTR recovering from RA2_ME__0P files

- Completeness report for Ku-band PTR (daily)

- Completeness report for S-band PTR (daily)

More details about the new averaging can be found in the Roadmap & Products Summary document [D-1-02] and in the Detailed Processing Model document [D-2-01]. Hereafter are presented the editing statistic and completeness report according to the PTR averaging procedure. As illustrated in Figure 3-37, only valid PTR were used to ensure best PTR signal quality, bad measurement being discarded based on thresholds editing described in [D-2-01].

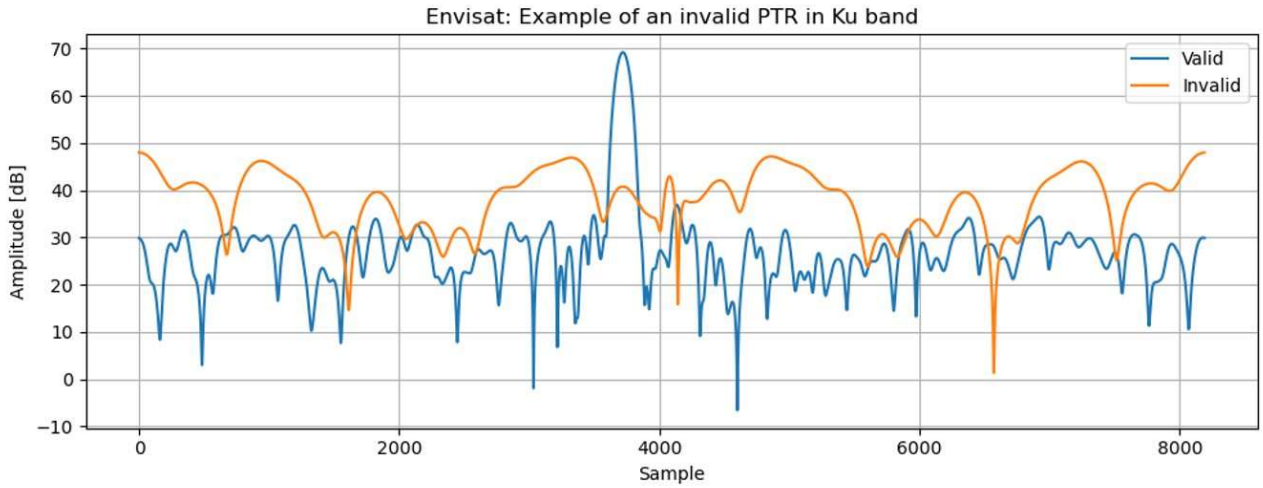

Figure 3-37: Example of PTR qualification for Ku-band

- Ratio of edited PTR in K-band (Bandwidth=320Mhz)

Ratio of edited PTR	2002	2003	2004	2005	2006	2007	2008	2009	2010	2011	2012
KU BAND	4382 / 12242062	1552 / 18212266	1514 / 19678064	947 / 19522488	536 / 19094468	348 / 19252048	62 / 20119362	51 / 19959425	111 / 19931545	154 / 20002524	115 / 5419985
S BAND	236 / 4403897	30 / 6570599	122 / 7031188	67 / 6975878	565177 / 6840303	3 / 6874520	6878697 / 7195870	7141094 / 7141094	7132751 / 7132751	7157506 / 7157506	1938186 / 1938186

- Resulting Mean PTR (I&Q averaging)

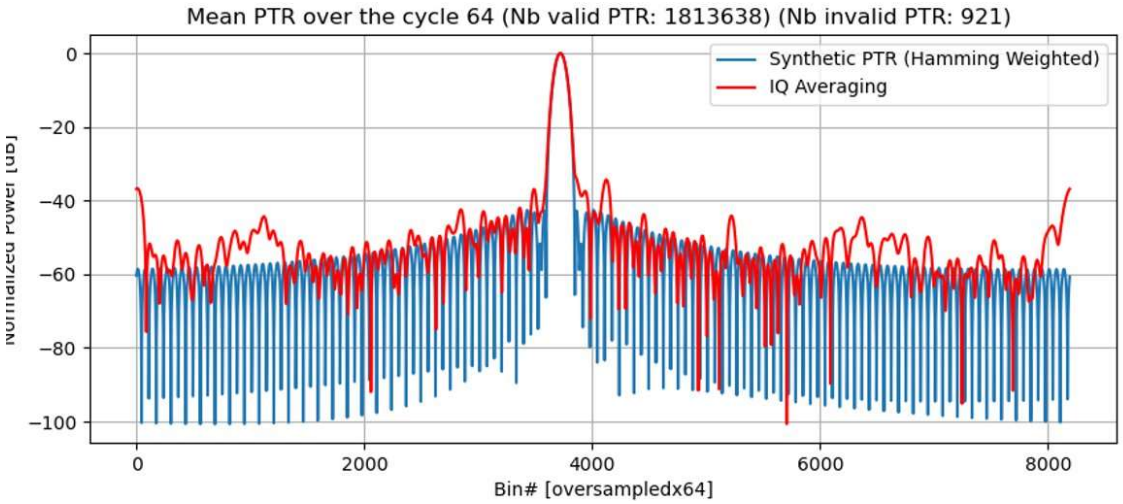

Figure 3-38: Oversampled mean amplitude PTR after I&Q averaging with Hamming window applied.

Mean Ku-band (and S-band) PTR samples are obtained for each satellite pass (half-orbit) by averaging individual PTR waveform over 10 days around with a minimum of 1000 pre-selected PTR to be considered as valid. This time window has been determined among several as a trade-off between availability and quality of data as shown in Figure 3-39 to Figure 3-44 for both Ku/S-band.

- Number of valid PTR over time

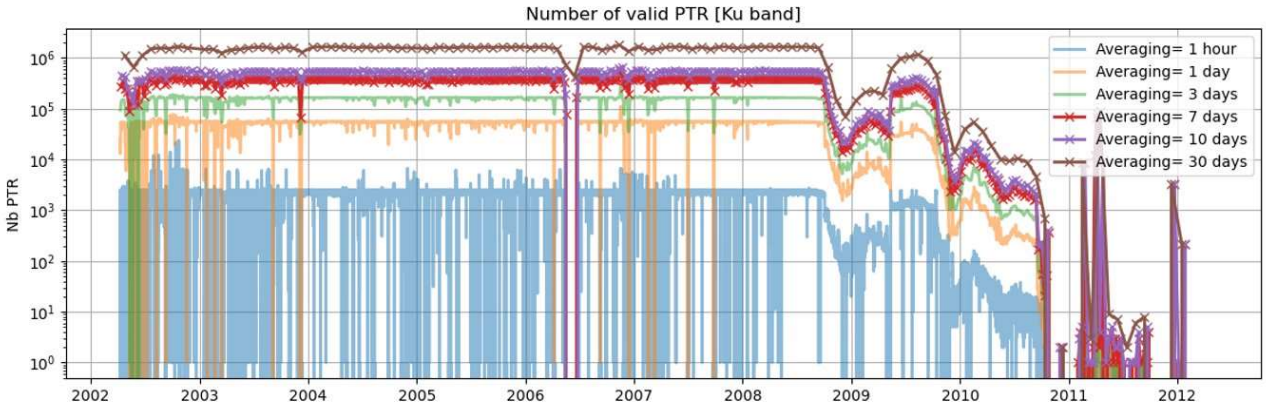

Figure 3-39: Number of valid K-band PTR w.r.t time window size

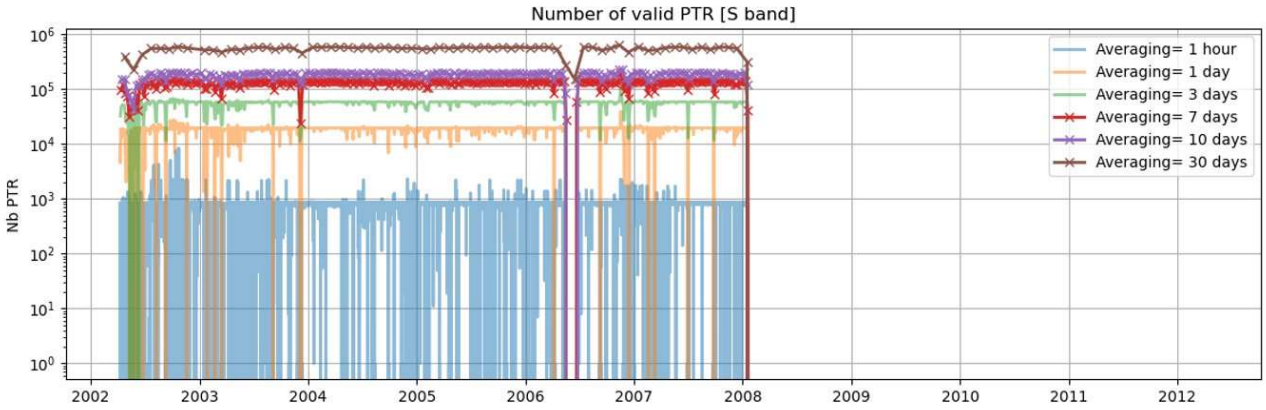

Figure 3-40: Number of valid S-band w.r.t time window size

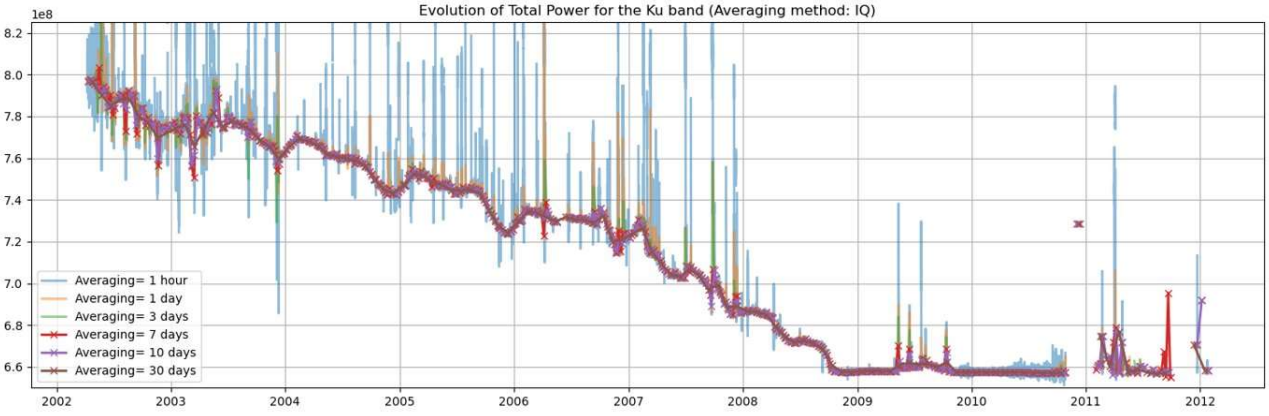

Figure 3-41: Total power in Ku-band w.r.t time window size

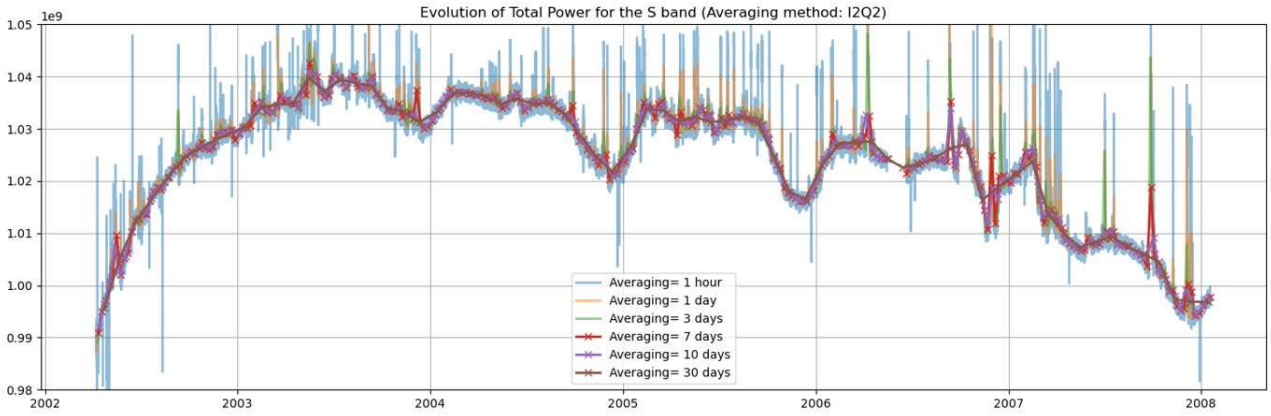

Figure 3-42: Total power in S-band w.r.t time window size

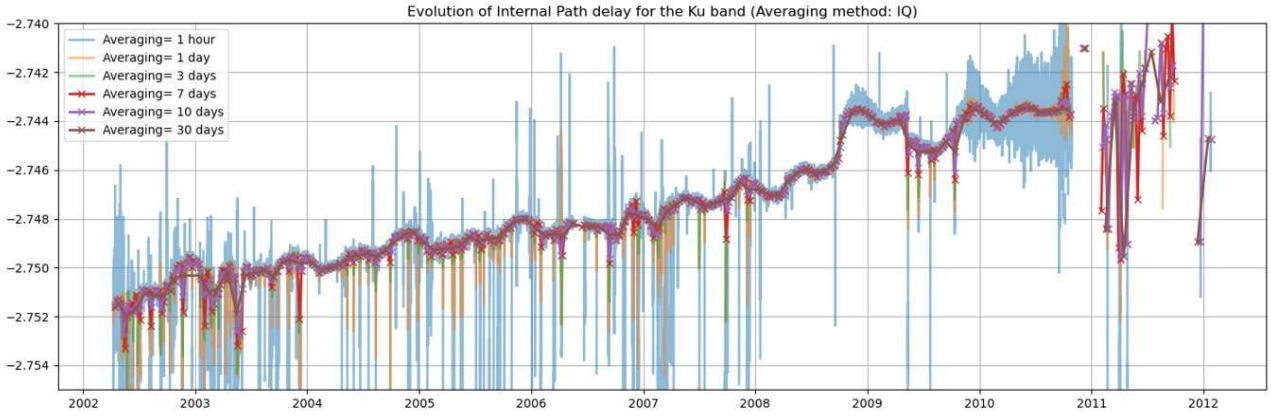

Figure 3-43: LTM of Internal Path Delay in Ku-band for different mean window size

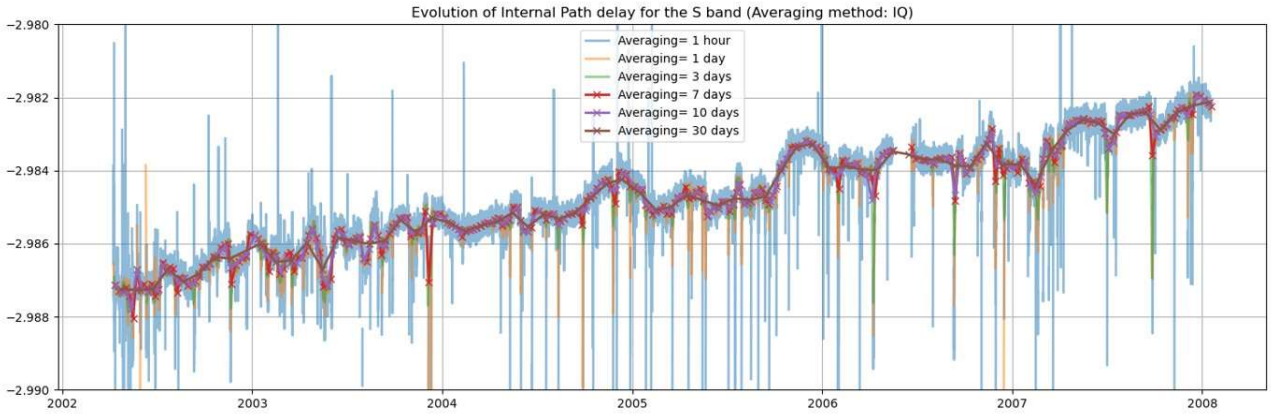

Figure 3-44: LTM of Internal Path Delay in S-band for different mean window size

Note that the internal path delay is a key parameter applied to the final range variable used to derived water height. For more details, one should refer to the Adaptive retracker section 4.4. Also, main lobe width (-3dB) of the averaged PTRs has been monitored over time as additional PTR quality indicator. Figure 3-45 and Figure 3-46 illustrate the monitoring for both Ku and S band of the main lobe width (in Hz) over time. Since S-band anomalies occurred on RA-2 during ENVISAT lifetime, no data can be recovered during those events.

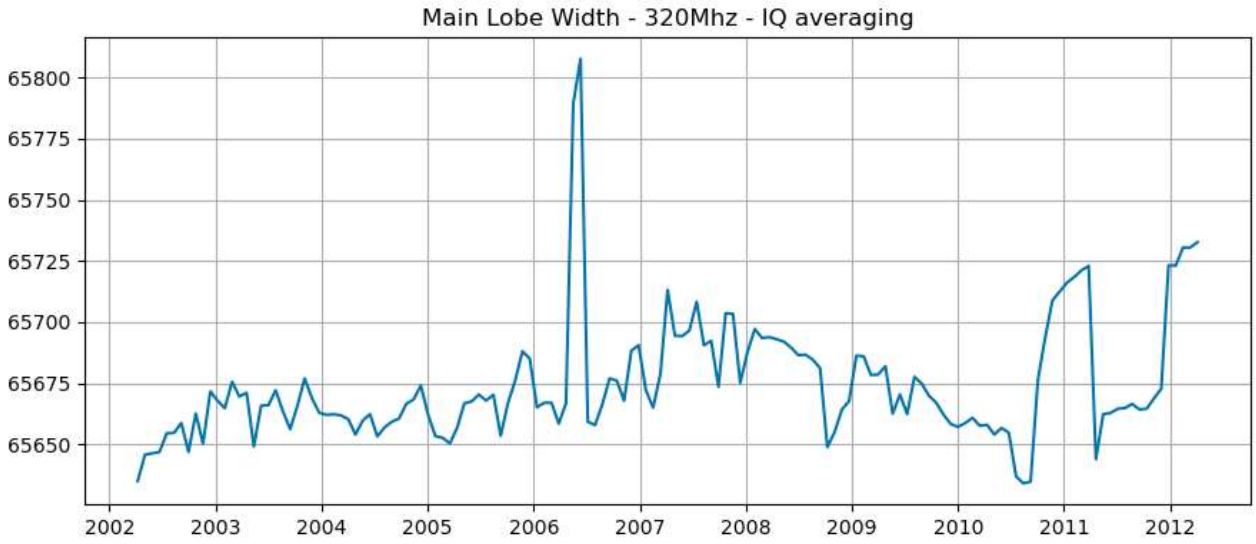

Figure 3-45: Monitoring of the main lobe width of the averaged Ku-band PTR (320Mhz bandwidth) over time. Y-axis unit is Hz and X-axis unit is year.

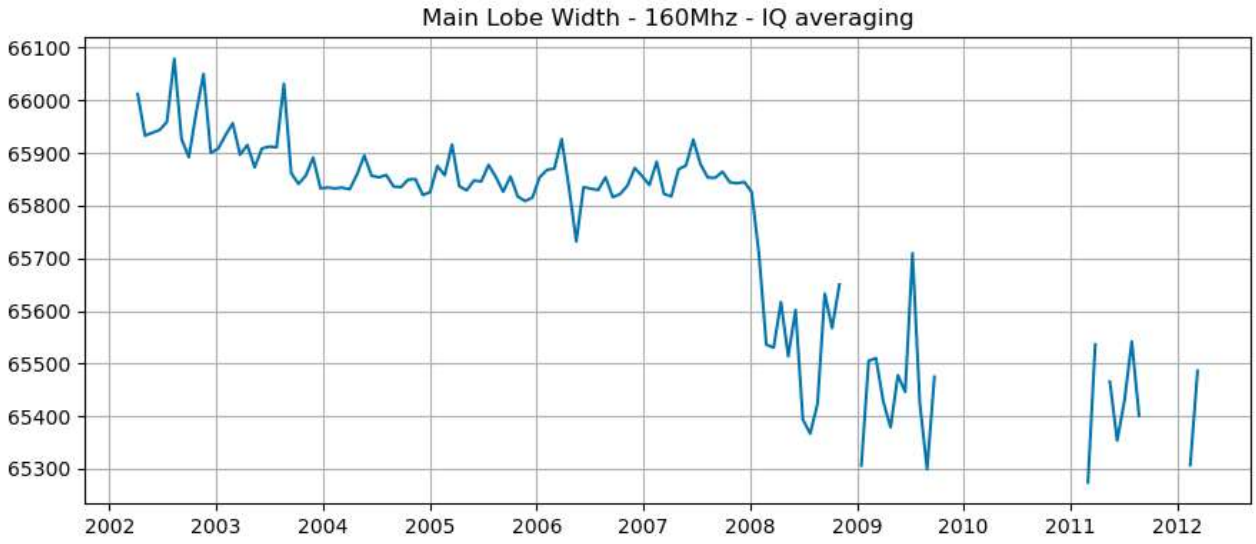

Figure 3-46: Monitoring of the main lobe width of the averaged S-band PTR (160Mhz bandwidth) over time. Y-axis unit is Hz and X-axis unit is year.

Finally, we analysed the availability of valid averaged PTR over the mission lifetime.

- Ku-band

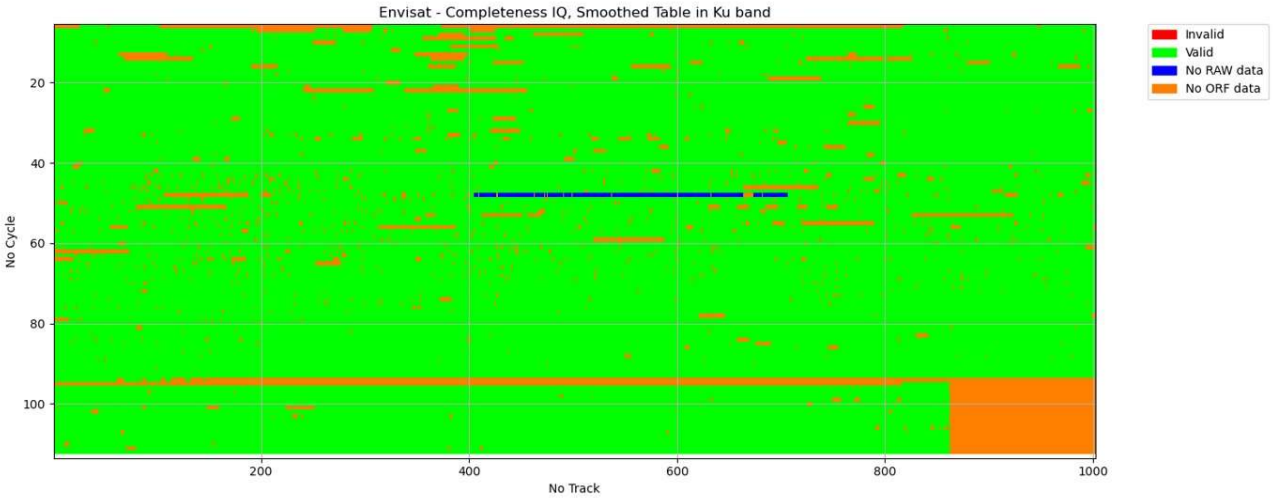

- S-band

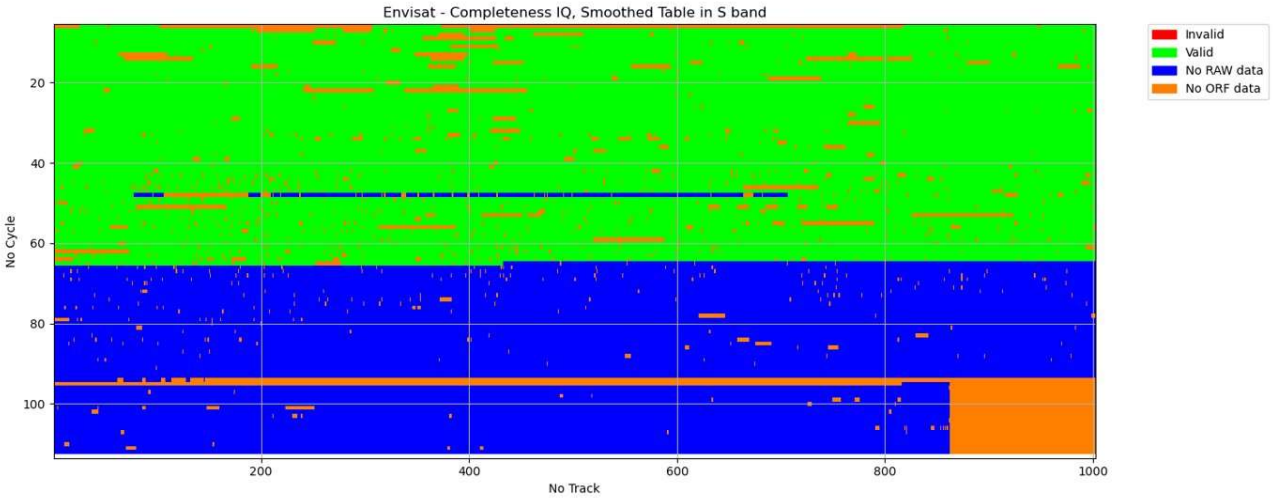

- Chain B

Since ENVISAT altimeter switched to Side B, we derived a single average PTR over the corresponding period.

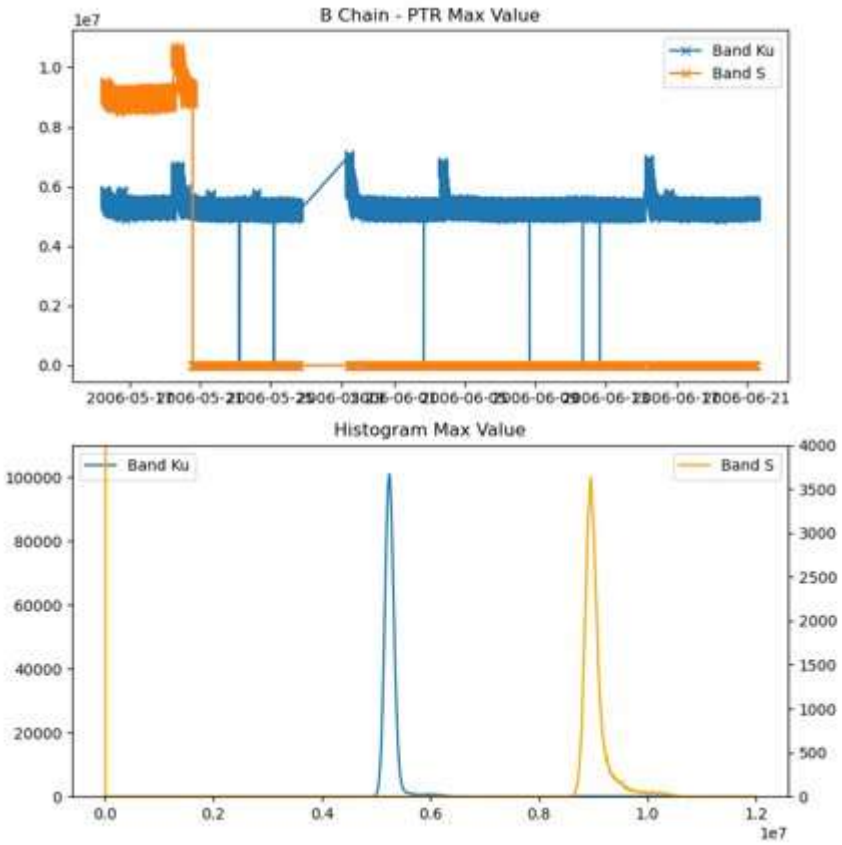

Figure 3-47: Editing threshold study for chain B PTR range values.

A specific editing based on threshold values on was applied.

- Maximum value > 0.4e7 for both Ku and S band
- Median Value < 1000

On top of the previous editing, only the PTRs with stabilized internal path delay (as shown for Ku-band in Figure 3-48) are used to compute the single side B mean PTR waveform.

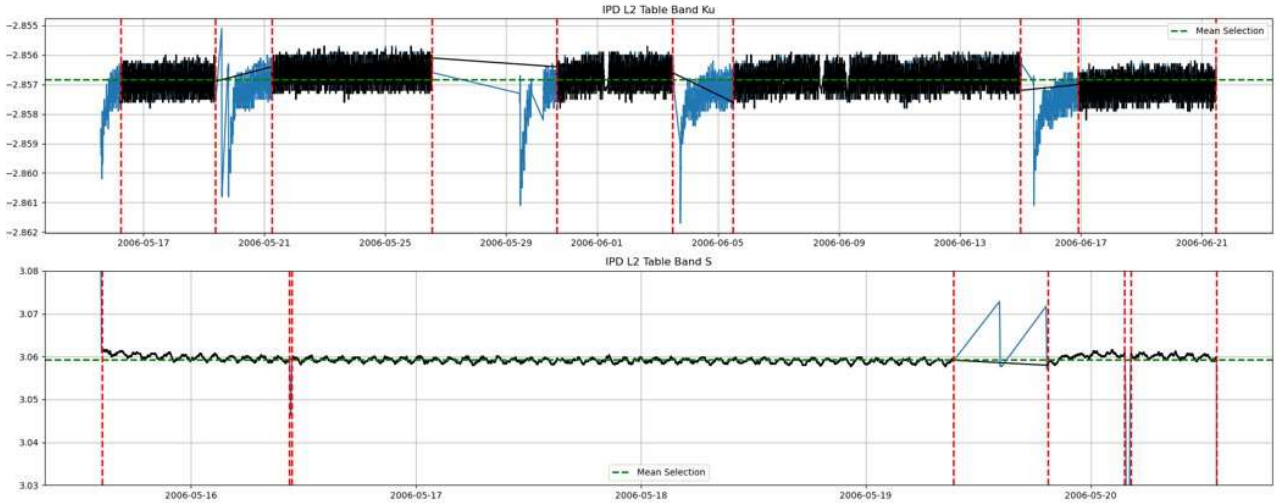

Figure 3-48: Level-2 internal path delay editing, black line represents selected individual PTR.

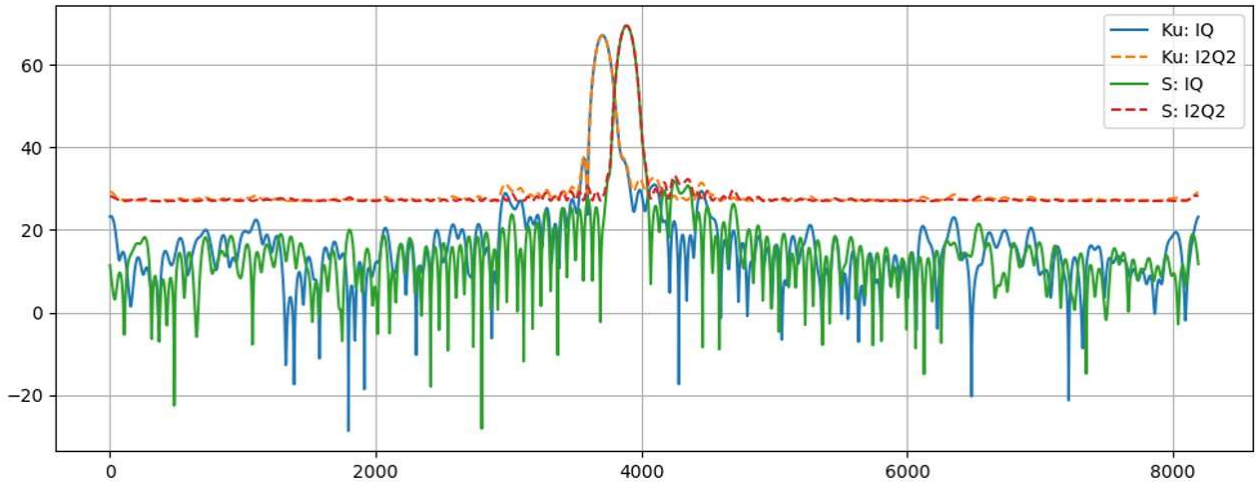

Figure 3-49: Final mean PTR for chain B: I&Q PTR for both Ku and S-band

3.9 Distance to shoreline & surface flag from GSHHG

Refer to the Product Validation Report : Ocean and Coastal TDP for validation.

3.10Reference documents

RD-1	D. J. Brockley, "REAPER—Product handbook for ERS Altimetry reprocessed products", Apr. 2014.
RD-2	REAPER RA L1b IODD ID: REA-DD-IODD-L1b-6002 Issue: 4.b
RD-3	RA-2 ALGORITHMS SPECIFICATION FOR LEVEL 1b SOFTWARE PROTOTYPING. ISARD_ESA_L1B_ESL_DPM_022. Issue 18. 16/06/2015.
RD-4	J. Poisson, G. D. Quartly, A. A. Kurekin, P. Thibaut, D. Hoang and F. Nencioli, "Development of an ENVISAT Altimetry Processor Providing Sea Level Continuity Between Open Ocean and Arctic Leads," in IEEE Transactions on Geoscience and Remote Sensing, vol. 56, no. 9, pp. 5299-5319, Sept. 2018, doi: 10.1109/TGRS.2018.2813061.
RD-5	isardSAT-reaper-calibration-monitoring-quality-assessment-results.pdf

4 The Adaptive Retracker

One of the improvements brought by the FDR4ALT project for the ENVISAT mission is the application of the Adaptive retracker. After a Round Robin exercise described in [D-2-03], the Adaptive outputs have been chosen for the Ocean Waves TDP and the Ocean & Coastal TDP and are available as "expert variables" for the Inland Waters TDP. The Adaptive Sigma0 has also been used for the Atmospheric TDP as an input. As the Adaptive retracker provides Level-2 outputs that have been used in several TDPs, it is described there in a dedicated section.

To validate the Adaptive retracker on ENVISAT, it is first compared to the former reference MLE3 on one full cycle of data. A special attention is paid to the fit of the Adaptive on the actual waveforms.

The Adaptive retracker is then fully validated at TDP level as described in the Product Validation Report : Ocean & Coastal TDP.

Note that the Adaptive retracker has also been tested on ERS but gave unsatisfactory results and could not be investigated more in the frame of this project. These investigations have been documented and can be found in Appendix A 1 -.

For this section, data have been selected over ocean using the following:

- ✓ Waveform class = 1 (ocean)
- ✓ Distance to shoreline > 50 km
- ✓ Abs(Latitude) < 60

4.1 Fit of the waveform

The MQE (Mean Quadratic Error) is a good parameter to assess the quality of the model fit of the waveforms. It is basically the quadratic difference between the waveforms and the fitted models. The lower the MQE, the better. Figure 4-1 shows a comparison of MQE between MLE3 and Adaptive. Not only the Adaptive MQE has a lower mean and standard deviation, but it is better everywhere on the globe. The improvement is more significant on low sea-states areas where the PTR has a bigger impact.

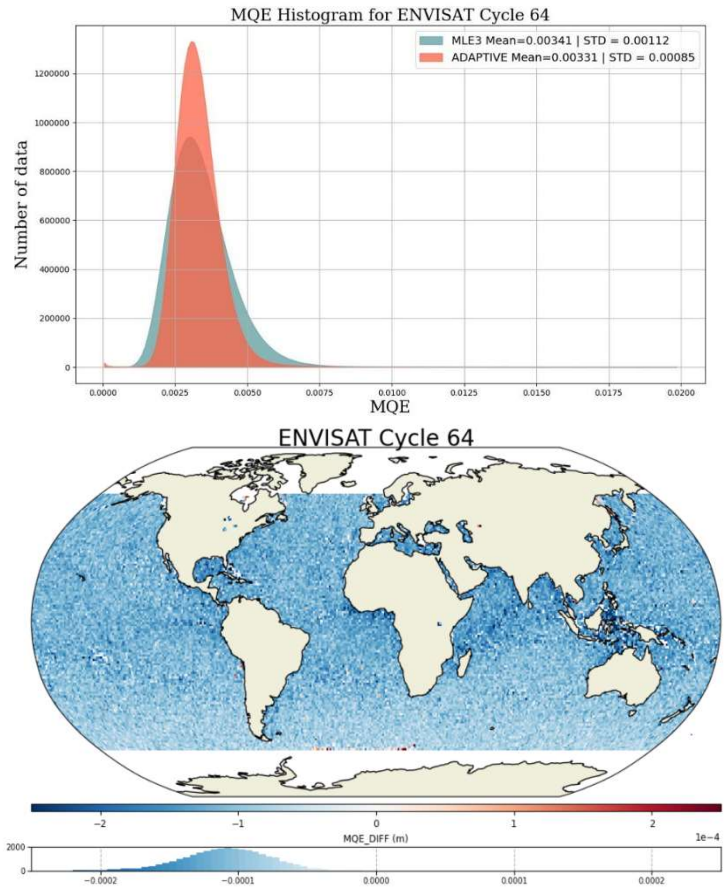

Figure 4-1 : Histograms of MQE MLE3 and Adaptive (Top) and gridded map of the MQE difference [Adaptive-MLE3] (bottom)

Another way to assess the goodness of fit is to compute waveform residuals, i.e., compute the difference between the fitted model and the waveform, averaged over a significant number of similar echoes (selected for a specific epoch and SWH). Figure 4-2 shows that, thanks to the introduction of the real PTR (Point Target Response), the Adaptive is systematically better than the MLE3 on the leading edge of the echo, which is the most important part. The Adaptive is also better on the trailing edge, except for very high waves.

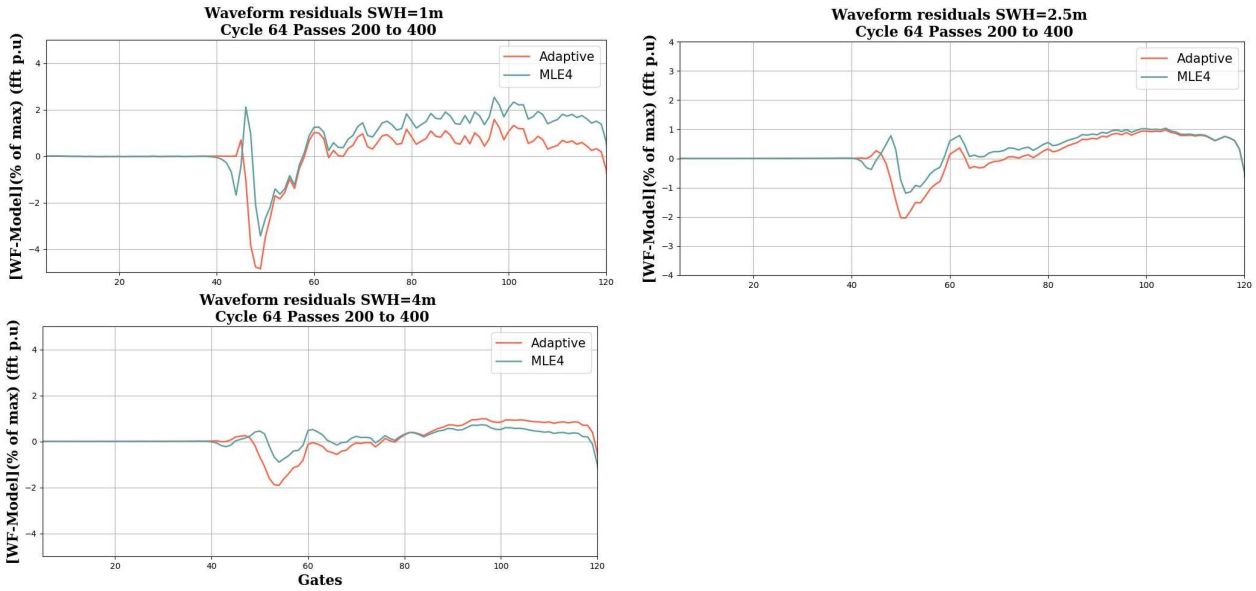

Figure 4-2 :Waveforms residuals for MLE4 (blue) and Adaptive (red) for 3 different SWH values

One of the main features of the Adaptive is its ability to process all surfaces, and not only oceanic-like surfaces with a typical "Brownian' echo. Its capacity to process peaky waveforms has been successfully validated on a few case studies such as the extremely peaky echo below in Figure 4-3. The Adaptive model fits perfectly the echo as expected.

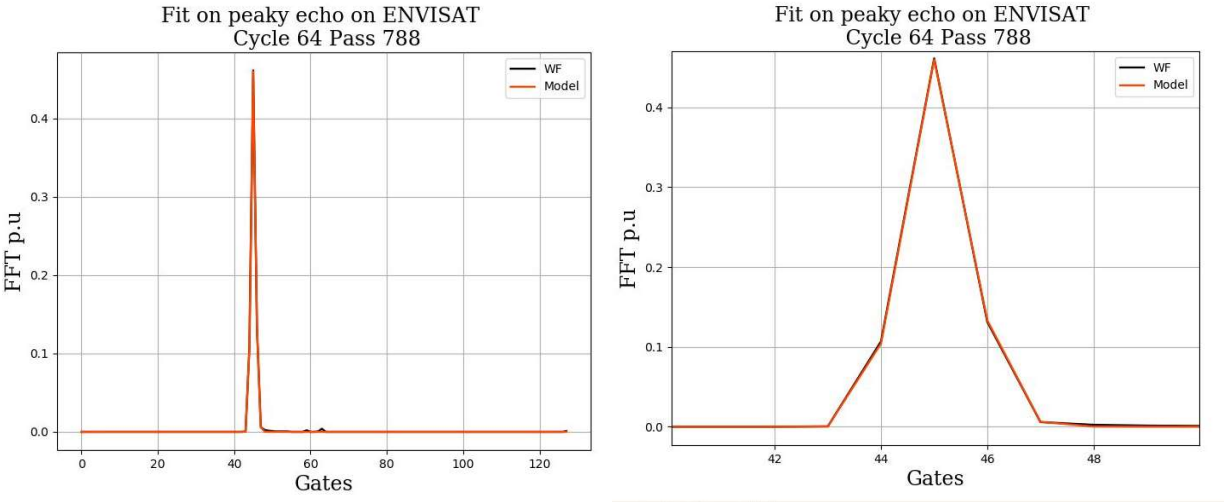

Figure 4-3 : Example of fit on a highly specular echo (left) and zoom on the max of the waveform (right)

4.2 Geophysical outputs: Range, SWH, Sigma0

To validate the Adaptive retracker, the geophysical outputs range, SWH and Sigma0 from the Adaptive are compared to the MLE3 outputs. The MLE3/Adaptive difference must be comparable to the MLE4/Adaptive differences obtained on Jason-3, which is the reference mission for the Adaptive (It was firstly developed on Jason-3 and is now implemented in the ground segment [**RD 4**]).

Indeed, any biases/dependencies that are too strong or not understood can be the sign of a sub-optimal parametrization of the retracker.

In this section, the datasets used are ENVISAT cycle 64 (December 2007-January 2008) and Jason-3 cycle 106 (December 2018-January 2019)

4.2.1 Range

Figure 4-4 shows that the range difference between Adaptive and MLE3 for cycle 64 is centered around **~2cm** with the majority of data between -4cm and 0cm. These metrics are directly comparable to Jason-3 for which the Adaptive retracker has been fully validated and implemented in the ground segment [**RD 4**].

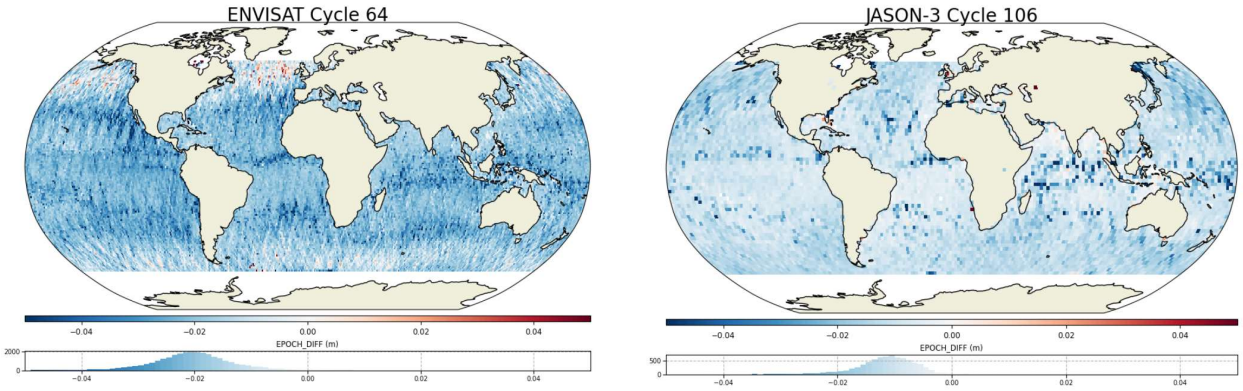

Figure 4-4 : Gridded map of the ENVISAT Epoch difference Adaptive-MLE3 (left) and gridded map of the Jason-3 Epoch difference Adaptive-MLE4 (right)

The mean bias is slightly higher for ENVISAT **(~2cm**) than Jason-3 (**~1cm**), but this could be partially explained by the look-up tables used for ENVISAT MLE3. Indeed, Look-up tables are used to compensate the error made by the Gaussian approximation of the PTR. On ERS and ENVISAT, a Hamming windowing is applied on the PTR, making the Gaussian approximation made by the MLE3 (ocean retracker used in ENVISAT V3.0) a little bit better. We remind that on Jason or Sentinel missions, this Hamming window is not applied and the use of look-up tables for the range and SWH is mandatory to avoid significant biases that are dependant to the sea-state.

On ENVISAT, look-up tables have been computed on the range and SWH in the frame of the V3.0 reprocessing. The range look-up table were considered negligible, but the SWH look-up table allowed a great improvement w.r.t SWH models.

To compute look-up tables, numerical models are simulated using the real PTR data.

As explained in section 3.8, a new way of averaging PTR has been used on ENVISAT. This new PTR can be used to compute new look-up tables, and this could have a non-negligible impact on SWH and range data from the MLE3. However, in the frame of this project, the MLE3 have been replaced by the Adaptive retracker, that directly uses the PTR in its processing, allowing to remove the need for look-up tables. Therefore, no new official MLE3 look-up tables were computed in the frame of FDR4ALT to be included in the products. However, to investigate possible biases, look-up tables were computed using a new PTR:

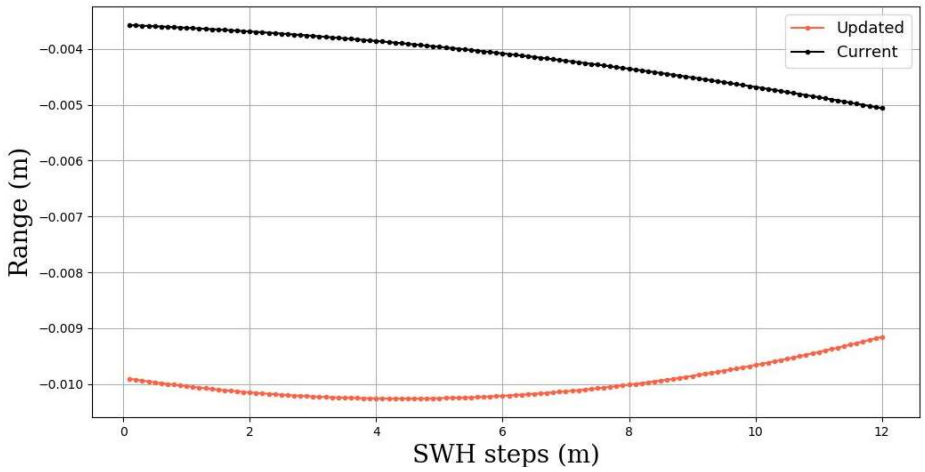

Figure 4-5 : Comparison between the V3.0 range look-up table (black) and the look-up table using the new PTR (red)

Figure 4-5 shows that with the new PTR, the look-up table in range is around ~1cm. For the V3.0, it was considered negligeable and therefore not applied. This ~1cm difference can explain the bias difference observed between ENVISAT and Jason-3 (Figure 4-4).

For more information about the validation of the Adaptive SSH, an extensive validation can be found in the Product Validation Report : Ocean & Coastal Topography TDP.

4.2.2 SWH

Figure 4-6 shows that the SWH difference between Adaptive and MLE3 for cycle 64 is centered around **~8cm** with the majority of data between -20cm and 0cm. These metrics are comparable to Jason-3 for which the Adaptive retracker has been fully validated and implemented in the ground segment [**RD 4**].

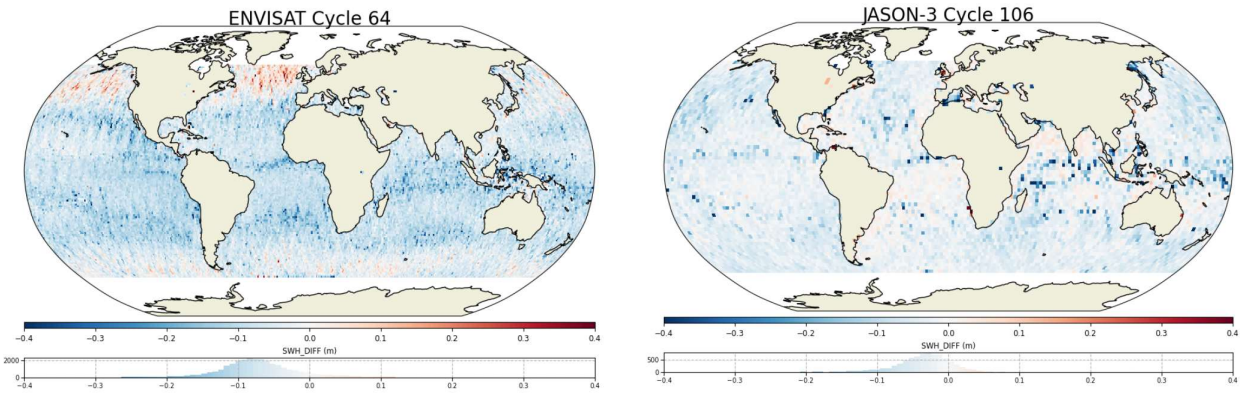

Figure 4-6 : Gridded maps of SWH difference Adaptive-MLE3 for ENVISAT (left) and Jason-3 (right)

The mean bias is higher for ENVISAT **(~8cm**) than for Jason-3 (**~3cm**), but this could be partially explained by the look-up tables used for ENVISAT MLE3.

As explained in the previous section (4.2.1), the look-up tables currently implemented in the V3.0 are sub-optimal and use a noisy PTR. When using an averaged FDR4ALT PTR, the new SWH look-up table is very comparable to the V3.0 for SWH<2m but can vary up to 5cm for high SWH. This is important to keep in mind when comparing MLE3 and the Adaptive.

Another important point is that the SWH look-up tables are not gaussian (as opposed to the range), meaning that the mean value used is biased. This explains fully the 3/4cm difference observed in Jason-3 [**RD 5**]. A similar analysis has not been performed on ENVISAT, but one can assume that the SWH look-up tables are also biased, by an order of magnitude that has not been quantified. Indeed, the new baseline for ENVISAT is now the Adaptive that does not need any look-up tables.

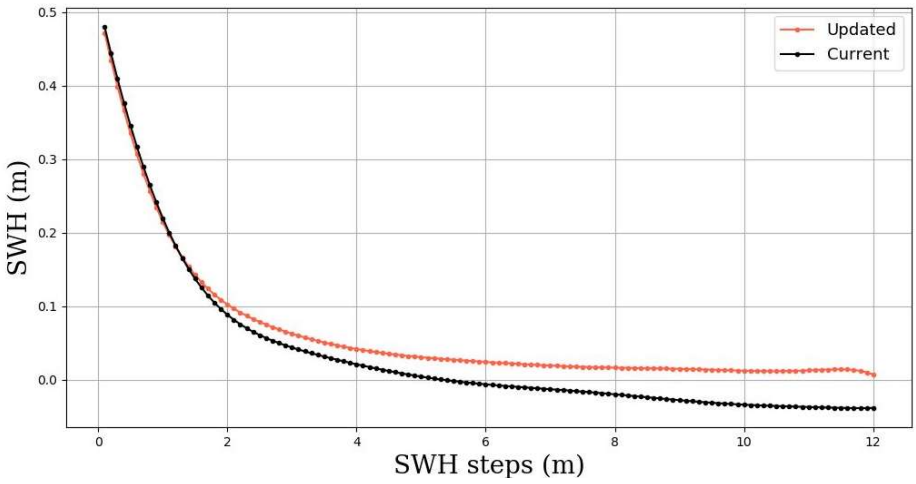

Figure 4-7 : Comparison between the V3.0 SWH look-up table (black) and the look-up table using the new PTR (red)

For more information about the Adaptive SWH, an extensive validation can be found in the Product Validation Report: Ocean Waves TDP.

4.2.3 Sigma 0

Figure 4-8 shows that the Sigma0 difference between Adaptive and MLE3 for cycle 64 is negligible. These metrics are not directly comparable to Jason-3 because the Sigma0 MLE3 and MLE4 are not similar. By construction, the MLE3 Sigma0 is more physical and is decorrelated from the trailing edge of the waveform, as opposed to the MLE4. The Adaptive Sigma0 is also more physical and decorrelated from the trailing edge, explaining why both solutions are so similar. The Sigma0 Adaptive therefore behaves totally as expected.

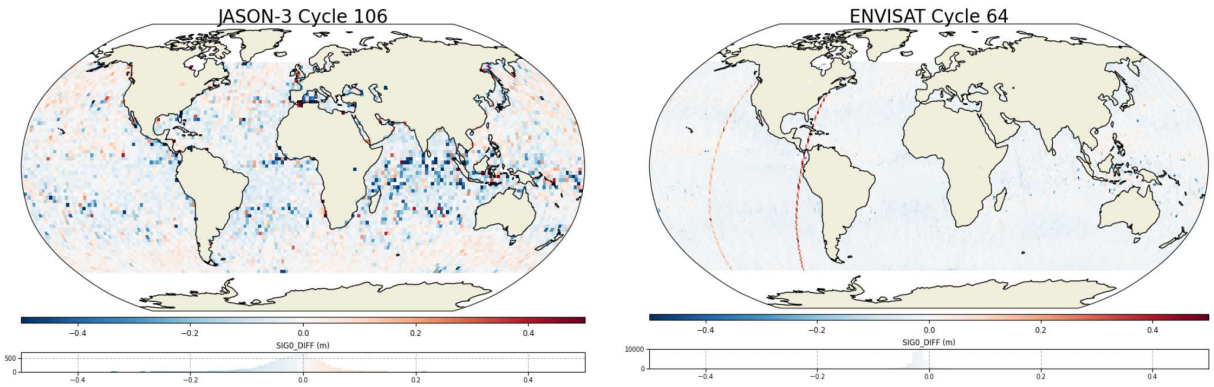

Figure 4-8 : Gridded map of the ENVISAT Sigma0 difference Adaptive-MLE3 (left) and gridded map of the Jason-3 Sigma0 difference Adaptive-MLE3 (left)

4.3 Continuity between ocean and sea-ice

One the main features of the Adaptive is its ability to process data from all surfaces. A good indicator of the Adaptive performances is to look at the continuity between the SLA in open ocean and the SLA from leads in the polar regions.

In order to do so, it is important to build two separates SLA, because the geophysical corrections cannot be applied on both ocean and leads similarly. To perform this diagnosis, data were selected between “ocean” and “leads” using the sea-ice fraction coming from OSI-SAF. Then, for the SLA ocean, the geophysical corrections applied are those used for the Ocean & Coastal TDP. For the SLA leads, the geophysical corrections applied are those used for the Sea-Ice TDP. Details about the corrections can therefore be found in the Products Requirements & Format Specifications document.

Figure 4-9 shows that using the Adaptive retracker, there is a perfect continuity of the SLA between open ocean and leads. Using the ICE-1 retracker for leads (as it is commonly done), there is a clear bias between ocean and leads.

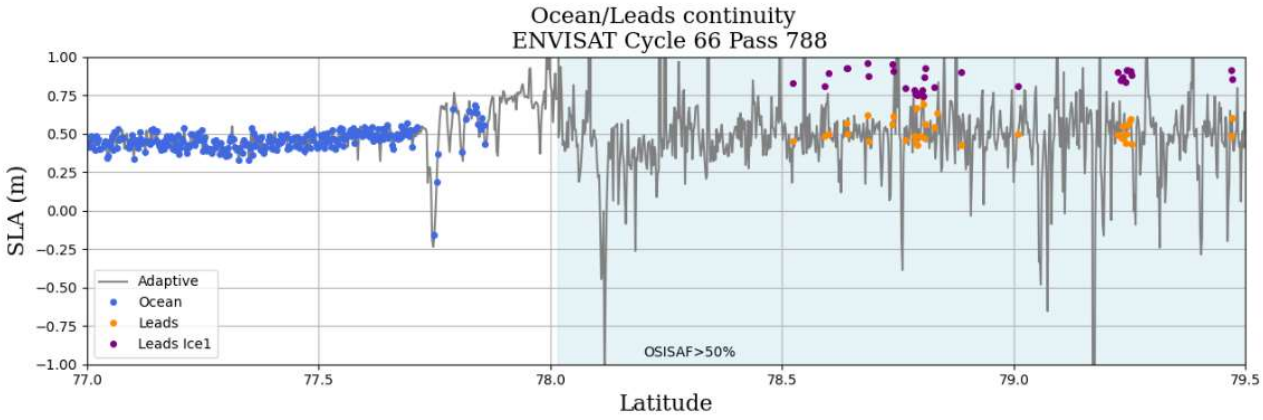

Figure 4-9 : Continuity of the Sea Level Anomaly between open ocean and leads. The blue envelope represents data where the sea-ice fraction from OSI-SAF is higher than 50%. Blue dots represent the Adaptive points identified as ocean by the waveform classification (class=1). Orange and purple dots are points identified as leads (class=2 and Sigma0 > 45 dB).

This confirms the excellent performances of the Adaptive on peaky echoes. Unfortunately, in the frame of this project, the Adaptive was not used in the Sea-Ice TDP. Therefore, it would be interesting to assess more globally the performances of the Adaptive in terms of SLA leads but also for the freeboard computation.

4.4 Focus on the internal path delay

The internal path delay correction is part of the corrections applied to the range and comes directly from the PTR itself. Lots of investigations have been made on this correction at the time of the V3.0 reprocessing [**RD 6**], and even if new PTR arrays have been used for the Adaptive (see section 3.8), we decided to keep this correction unchanged for the project, i.e., to use the same internal path delay correction as it was previously done for the V3.0 reprocessing.

However, during the global validation of the Ocean & Coastal TDP, questions were raised on the new GMSL obtained with the Adaptive retracker, and we decided to take a closer look to this correction. Figure 4-10 show the difference between the V3.0 internal path delay and the one obtained in the frame of FDR4ALT, using the new PTR arrays. It has been smoothed over 10 days (same windowing as the PTR averaging, see 3.8). The difference varies between -1.25mm and -2.75mm, with a bias quite stable for the first years of the mission.

This difference is quite small and will not have any impact on 20Hz data, as this difference will be hidden below the data noise. However, for the 1Hz data and the GMSL analysis in particular, this difference can have an impact on the trend estimations. Therefore, this difference was directly applied to the 1Hz range estimations of the Ocean & Coastal TDP (see Product Validation Report : Ocean & Coastal TDP).

Please note that this was not applied on the 20Hz range estimations for the Inland Waters TDP expert group.

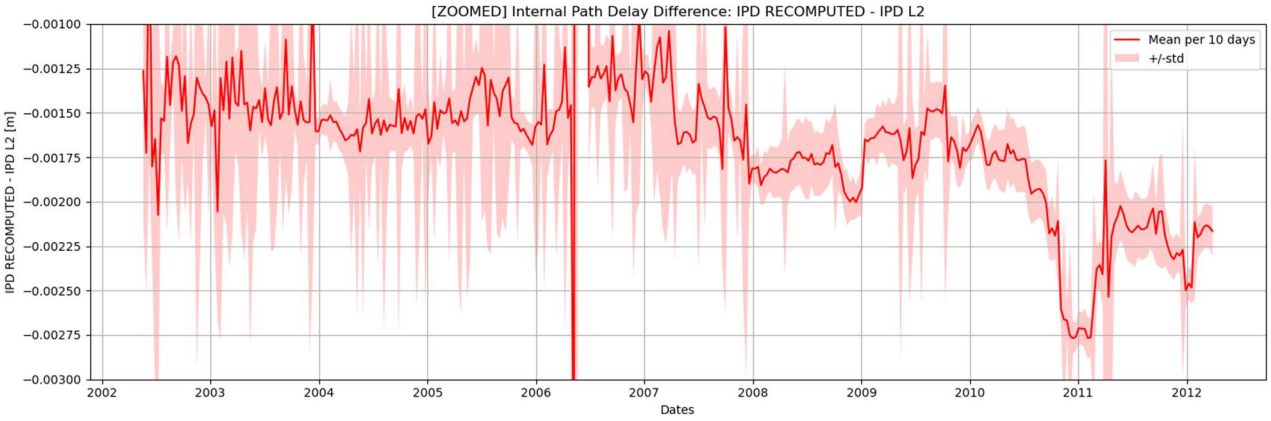

Figure 4-10 : Difference between internal path delay from Level 2 V3.0 and internal path delay computed from the FDR4ALT calibrations.

It is important to note that ideally, this correction should not be applied to the range but directly taken into account in the retracker via the natural convolution of the PTR. The version of the Adaptive used for FDR4ALT recentres the PTR before convolution, and the internal path delay correction must be applied at range level as it was usually done.

Even if the impact of this method is considered as negligible today, it would be more elegant and could remove the potential source of error that is the PTR centring.

4.5 Reference documents

RD 3	C. Tourain, F.Piras *et al.*, "Benefits of the Adaptive Algorithm for Retracking Altimeter Nadir Echoes: Results From Simulations and CFOSAT/SWIM Observations," in ***IEEE Transactions on Geoscience and Remote Sensing***, doi: 10.1109/TGRS.2021.3064236.
RD 4	P. Thibaut *et al.*, "Benefits of the "Adaptive Retracking Solution" for the JASON-3 GDR-F Reprocessing Campaign," *2021 IEEE International Geoscience and Remote Sensing Symposium IGARSS*, 2021, pp. 7422-7425, doi: 10.1109/IGARSS47720.2021.9553647.
RD 5	JC Poisson, F.Piras, P.Thibaut., New Powerful Numerical Retracker Solution Accounting for Speckle Noise Statistics, OSTST La Rochelle
RD 6	Quality Assessment Results of REAPER calibrations (pdf, IsardSAT), 2014

5 MWR Fundamental Data Records

5.1 Introduction

The validation of the intercalibration of the three missions follows the same strategy as the Sentinel-3 in-flight calibration **[RD 12],** based on vicarious analyses applied to several missions and covering the full range of brightness temperatures:

- Comparison of measurements to simulated brightness temperatures;
- Comparison of coldest ocean points applied to measurements;
- Comparison of hottest temperature over the Amazon Forest;
- Climatological stability.

This kind of diagnostics allows to assess the stability in terms of K/decade and to validate the brightness temperature range with respect to an intercalibration reference.

In addition, the completeness of the whole dataset is analysed.

5.2 Completeness

A global overview of data validity is provided as a donut chart such as Figure 5-1 (left plot), while details of data quality and reasons for flagging are represented as well (right plot).

From Figure 5-1, it can be seen that 1.35% of the ENVISAT data are flagged as “degraded” due to the lack of precise orbit files at the beginning of the mission (from 2002-04-10 to 2002-06-17). Otherwise, the number of data flagged as “bad” is small, lower than for ERS, and corresponds mainly to anomalous values detected on brightness temperatures. For ERS (Figure 5-2 and Figure 5-3), the main cause of invalidity are the anomalous values of the calibration parameters. A small part of the mission (0.1%) is flagged as ‘degraded’ due to the lack of precise orbit files, but it only represents the first 3 days/5days of the ERS-1/ERS-2 missions respectively. Note that for ERS-1, due to the missing cycle/pass definition of these three days, these data cannot be provided in the FDR dataset.

The completeness of the FDR product is addressed through monthly plots throughout the mission lifetime. Figure 5-4 represents the quality flag of one main parameter (here the brightness temperature of the 36.5GHz channel) using three colours according to data quality. The data gaps are represented as white gaps. Each column represents a day, with the 24hours of the day on the y-axis. The whole x-axis spans one month for each plot. With this mapping, data coverage and issues can easily be identified by the user for a specific date and time. For instance, in this plot we can see that the data quality is degraded at the beginning of the mission until the first day when the precise orbit files are available. Users are strongly recommended to use only data flagged as “valid”, as flagged data can contain very anomalous situations. The completeness of the whole period of the three missions will be provided in a separate document (Completeness Report [D-5-04]) where the list of all the unavailable product files is provided, along with the reasons for unavailability.

Looking at Table 5, it appears that a certain amount of missing telemetry (up to 61% for ERS-1) cannot be explained by any instrumental event. This could mean that efforts to consolidate the L0 dataset archive could help to recover some gaps, especially for ERS-1.

In addition, two problems have been identified by inspecting ERS Level 0 files headers that could explain some of the missing files resulting due to unprocessable telemetry:

1) For some files, start and stop times derived from OBC values and time correlation files are different from those reported in the filename and ASCII headers; this also affects the assigned orbit number -> ERS-1/ERS-2: 11/36 telemetry.
2) Several ERS L0 files were generated by selecting a state vector with a time beyond the expected nominal 2 hours -> ERS-1/ERS-2: 191/101 telemetry.

Table 5 : Number of available and missing FDR MWR files for each mission

	Number of available files	Number of missing files (% of total dataset)	Number of missing files due to unexplained missing telemetry (% of missing files)
ERS-1	49067	1526 (3%)	937 (61.4%)
ERS-2 before tape recorder failure	169139	3625 (2.1%)	1424 (39.3%)
ERS-2 after tape recorder failure		15033 (8.9%)	NA
ENVISAT	101167	3409 (3.3%)	1417 (41.6%)

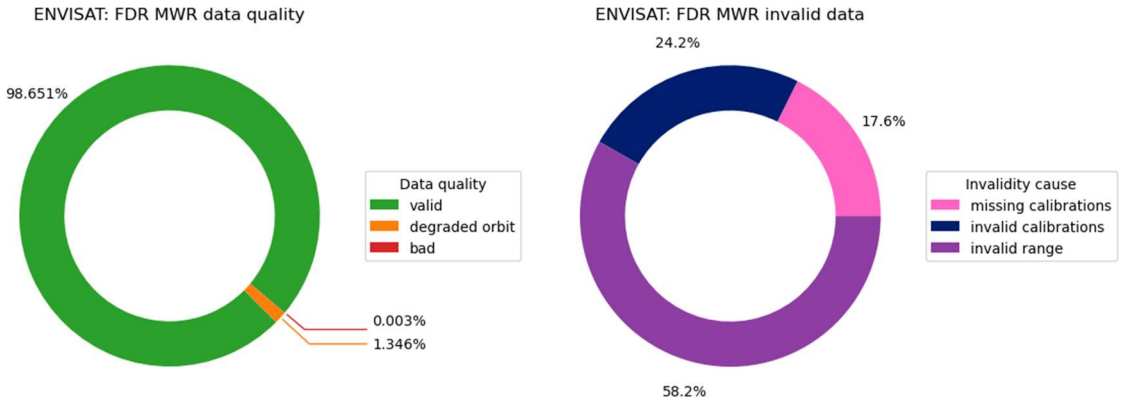

Figure 5-1 : Data quality and invalid data cause repartition for the full dataset of ENVISAT FDR MWR

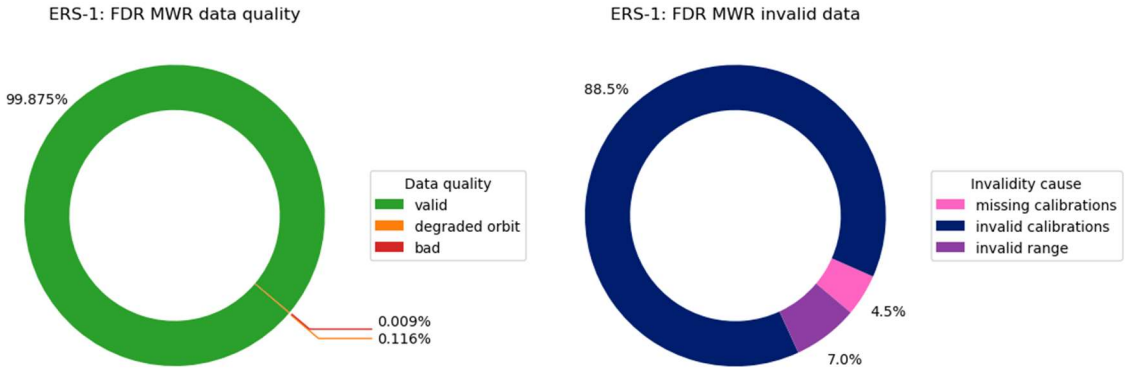

Figure 5-2 : Data quality and invalid data cause repartition for the full dataset of ERS-1 FDR MWR

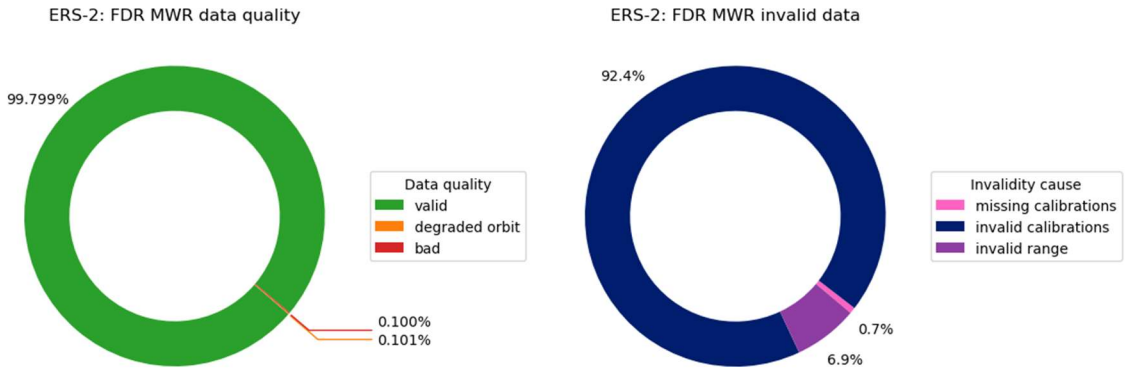

Figure 5-3 : Data quality and invalid data cause repartition for the full dataset of ERS-2 FDR MWR

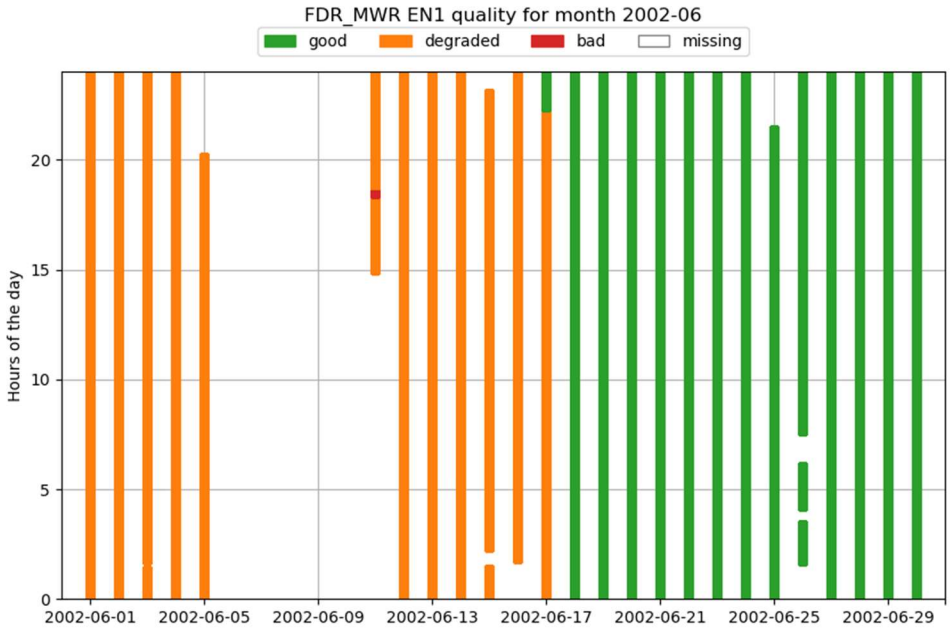

Figure 5-4 : Completeness and quality of the FDR MWR products for June 2002 of ENVISAT dataset

5.3 Harmonized brightness temperature validation

This section addresses the brightness temperature bias correction validation. The homogenized brightness temperatures are computed using from the harmonized brightness temperatures. Hence, the validation of homogenized brightness temperatures is focused on the bias correction.

5.3.1 Radiometric NeDT (sensitivity)

Since FDR4ALT MWR FDR contains, for the first time, radiometer data directly at the MWR sampling rate (7Hz, 150ms), it gives access to the MWR instrumental noise, the so-called radiometric sensitivity.

One of the methods to verify that the sensitivity is close to on-ground measurements consists in performing a spectral analysis of the brightness temperatures. The cut-off frequency with the noise plateau represents half the size of the MWR pixel. Below that cut-off frequency, the spectra are flat, revealing nothing but white

noise. The only information available at these scales is the instrumental noise. This noise provides an estimation of the MWR sensitivity.

The radiometric sensitivity estimation (Table 6) is consistent between ERS-1 and ERS-2, with lower sensitivity for the 36.5GHz channel. The 23.8GHz sensitivity is consistent with the value of 0.4K cited by [**RD 17**]. Envisat sensitivity is the same for both channels, consistent with the values found in literature (0.4K for both channels [**RD 16**]), and very close to ERS 36.5GHz channel sensitivity.

Table 6 : Radiometric NeDT for ERS-1, ERS-2, ENVISAT FDR MWR products

	ERS-1	ERS-2	ENVISAT
23.8GHz	0.40K	0.47K	0.35K
36.5GHz	0.32K	0.34K	0.35K

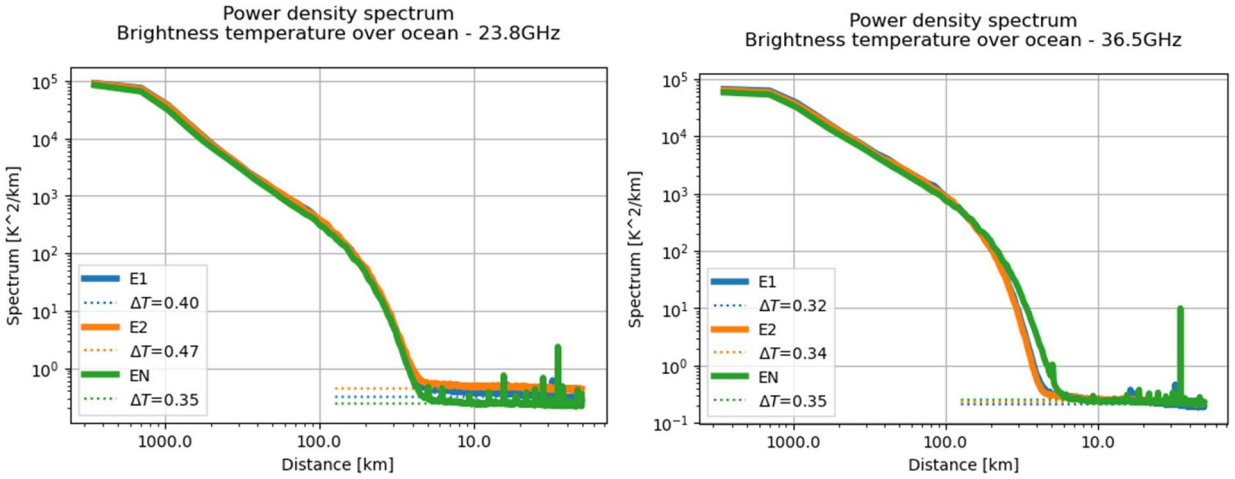

Figure 5-5 : Power density spectrum for FDR4ALT brightness temperature for 23.8GHz (left) and 36.5GHz (right) over ocean.

5.3.2 Vicarious Calibration - Ocean coldest temperatures

In a study on the detection of MWR calibration drifts [**RD 7**], Ruf showed that coldest ocean points are observed under specific conditions: low wind, no clouds, and low humidity content. This set of conditions is encountered with a sufficient regularity that a useful number of observations can be accumulated within a few days or weeks. Moreover, it happens that these conditions are also the easiest to model. Then the tail of the brightness temperature histograms provides a reference which can be used for calibration and detection of drift in the calibration.

These coldest temperatures can be used to detect instrumental drifts and are also used for long-term monitoring and inter-calibration . This method was used for in-flight calibration and the long-term monitoring of SARAL/ALtiKa [**RD 13**] and Sentinel-3A/B missions [**RD 12**].

The Figure 5-6 shows the time series of the coldest brightness temperatures over the ocean for the 23.8 GHz channel of ERS and ENVISAT missions. The orange curves illustrate the data of the previous reprocessing, while the blue curves stand for FDR4ALT reprocessing. The right panel of the figure shows averaged values over each mission period, except for ERS-2 where data are considered only before the tape failure event

(1995-2003). It is clear that the previous reprocessing shows a calibration difference of 2K between ERS-1 and 2, while ENVISAT seems to be aligned with ERS-2. It is also a bit lower (-1K) than Sentinel3-A calibration.

With the FDR4ALT reprocessing, ERS-1, ERS-2 and ENVISAT are now aligned, and consistent with Sentinel3-A calibration. The same monitoring for the 36.5 GHz channel is displayed in Figure 5-7. As for 23.8 GHz channel, the previous reprocessing of ERS-1 and ERS-2 differs by 2K and a little (0.5K) from the ENVISAT calibration. A strong annual signal can be observed on the ERS-1 and ERS-2 timeseries. With the FDR4ALT reprocessing, this signal disappears and the three mission are well aligned, consistently with Sentinel3-A. The analysis of post tape failure period of ERS-2 (2003-2011) must be made carefully, since the data are really partial (measurements only around ground stations) and statistics for this period can be really different.

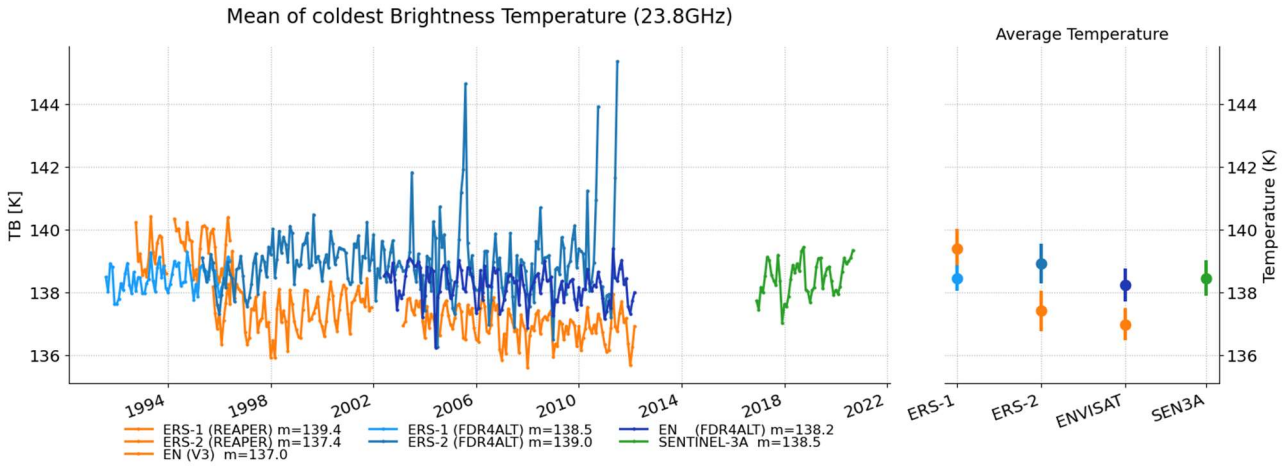

Figure 5-6 : Time series of coldest brightness temperatures over ocean for measurements at 23.8 GHz ERS-1, ERS-2, ENVISAT and Sentinel-3A. The right panel shows the average temperature computed over each mission data period.

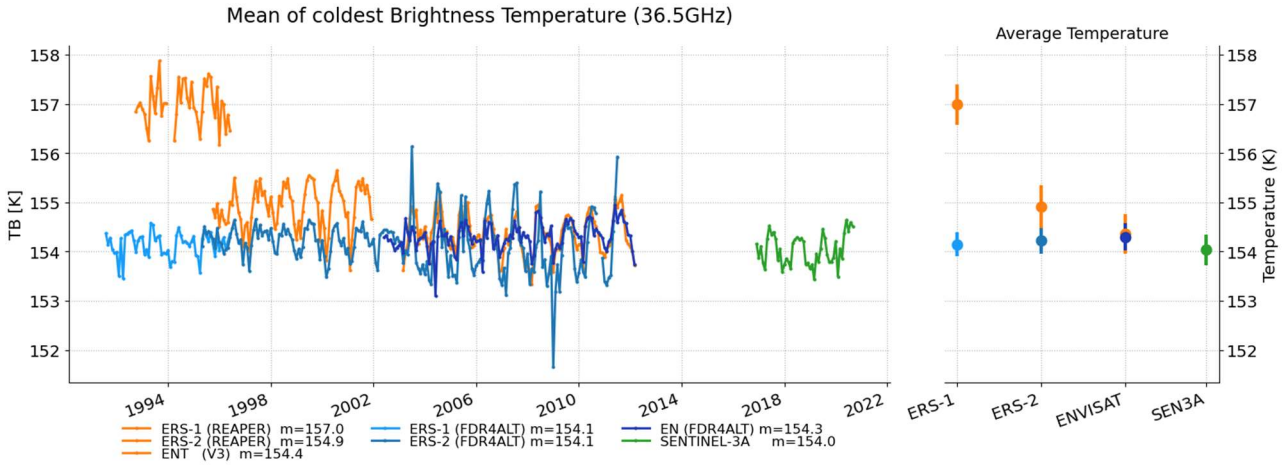

Figure 5-7 : Time series of coldest brightness temperatures over ocean for measurements at 36.5 GHz ERS-1, ERS-2, ENVISAT and Sentinel-3A. The right panel shows the average temperature computed over each mission data period.

5.3.3 Vicarious Calibration - Comparison to simulated brightness temperatures

The comparison of measurements and simulations is called single difference. It allows to account for the instrument characteristics like the frequency, the incidence angle and the orbit. The single difference is a good way to remove configuration and orbit impact on the final estimation. Thus, in the difference remains

only the calibration. This method was successfully applied to Sentinel-3A/B: it allowed to detect and correct a slight difference between ascending and descending (study funded by ESA/ESTEC in 2019).

To perform this analysis, the simulated brightness temperatures are computed using surface and profile parameters from the ERA5 Numerical Weather Prediction model reanalysis and a Radiative Transfer Model. Collocated simulated brightness temperatures are computed using a space/time threshold of 50km/30minutes. The consistency of the comparison is improved by the filtering of outliers. Indeed, large differences between measurements and simulations can be observed close to the coast due to the land contamination of the main beam, or in icy areas or in cloudy situations that are inaccurately handled by NWP models.

To do so, the radiative transfer model requires daily meteorological atmospheric profiles defined on ERA5 model levels. However, the huge accessibility problems encountered to download ERA5 profiles from the CDS (Copernicus Data Store) made impossible to download the profiles necessary for this diagnosis in time for the validation of the whole FDR dataset. Therefore, this diagnosis has been performed only for one year for each of the three missions (corresponding to the Test Dataset TDS) during the pre-validation phase.

The single difference analysis can be carried out globally but here, we process separately the ascending and descending passes. This allows the detection of unwanted ascending/descending signal. Since REAPER data does not cover the whole analysis period of ERS-2, we added the OPR data (orange curve) to give a comparison point.

When applied to ERS-1 (Figure 5-8) and ERS-2 (Figure 5-9), this analysis shows that for the 23.8 GHz channel, a small signal between ascending and descending passes is corrected with FDR4ALT reprocessing. In addition, the mean difference is consistent between ERS-1 and ERS-2 (resp. 3.5K/3.6K) while for REAPER it was very different of 2K (4.9K/2.8K).

Same conclusion applies for the 36.5GHz channel, except for ERS-2 were the signal between ascending and descending curves seems to slightly, but not significantly, grow. This could mean that the satellite temperature correction could be improved further.

The results are more evident for ENVISAT, were the new processing clearly corrected a huge asc/dsc signal that could reach 1.5K depending on the season.

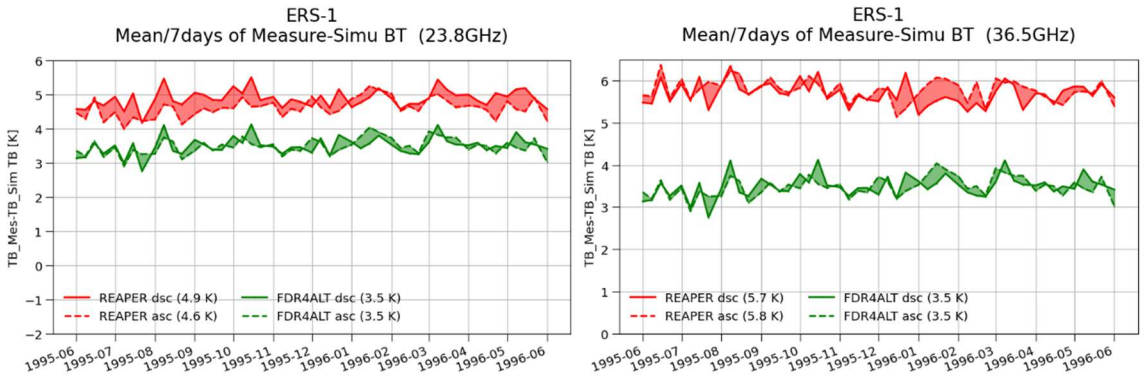

Figure 5-8 : Difference of measured brightness temperature with simulated brightness temperatures for ocean measurements for ERS-1 mission. Left plot illustrates the 23.8GHz channel and right plot the 36.5GHz channel.

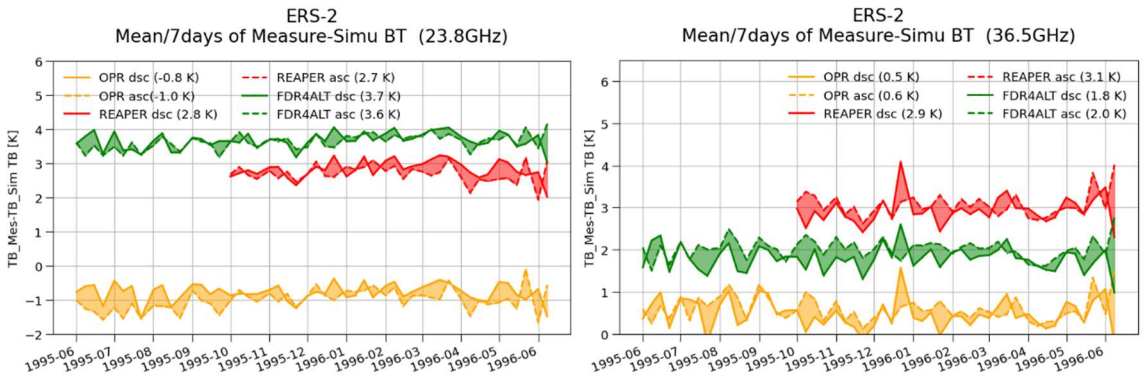

Figure 5-9 : Difference of measured brightness temperature with simulated brightness temperatures for ocean measurements for ERS-2 mission. Left plot illustrates the 23.8GHz channel and right plot the 36.5GHz channel.

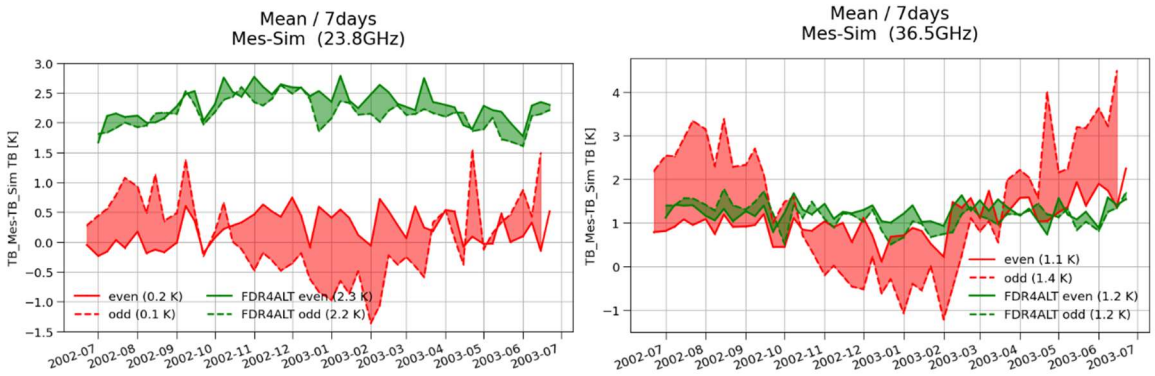

Figure 5-10 : Difference of measured brightness temperature with simulated brightness temperatures for ocean measurements for ENVISAT mission. Left plot illustrates the 23.8GHz channel and right plot the 36.5GHz channel.

5.3.4 Vicarious Calibration - Hottest Amazon Forest temperatures

The Amazon Forest provides a reference target calibration at the high end of the radiometer dynamic range. It is the natural body, the closest to a black body for a microwave radiometer with the emission of the canopy that is independent of the polarization and the incidence angle. Thus it is commonly used to assess the calibration of microwave radiometers [**RD 8**][**RD 9**][**RD 14**].

This method was used for in-flight calibration and the long-term monitoring of SARAL/ALtiKa [**RD 13**] and the Sentinel-3A/B missions [**RD 12**].

The Figure 5-11 shows the time series of the hottest brightness temperatures over the Amazon Forest for the channel 23.8GHz of ERS and ENVISAT missions. The orange curves illustrate the data of the previous reprocessing while the blue curves stand for FDR4ALT reprocessing. The right panel of the figure shows averaged values over each mission period, except for ERS-2 where data are considered only before the tape failure event (1995-2003). It is clear that the previous reprocessing suffers of too hot brightness temperatures for ERS-1 and 2, with a calibration difference of 1.6K between the two. It is also very far (9K) from ENVISAT calibration which seems very cold. With FDR4ALT reprocessing, ERS-1, ERS-2 and ENVISAT are aligned, and consistent with Sentinel3-A calibration. Data from AMSU on Metop-A (grey curve) helps to check that the strong feature observed towards the end of ENVISAT mission (2010-2011) is not due to instrumental problem and correspond to a geophysical event since it is also observed by AMSU. The analyse of post tape failure

period of ERS-2 (2003-2011) must be made carefully since the data are really partial and statistics can be really different for this period.

The same monitoring for the 36.5GHz channel is displayed onFigure 5-12. For this channel, AMSU mission was not added since the channel frequency is different (31.4GHz) so cannot be compared directly. As for 23.8GHz channel, the previous reprocessing of ERS-1 and ERS-2 differ of 1K and are too hot (10K) with respect to ENVISAT. The FDR4ALT reprocessing aligns well the three mission consistently with Sentinel3-A. The analyse of post tape failure period of ERS-2 (2003-2011) must be made carefully since the data are really partial and statistics can be really different for this period.

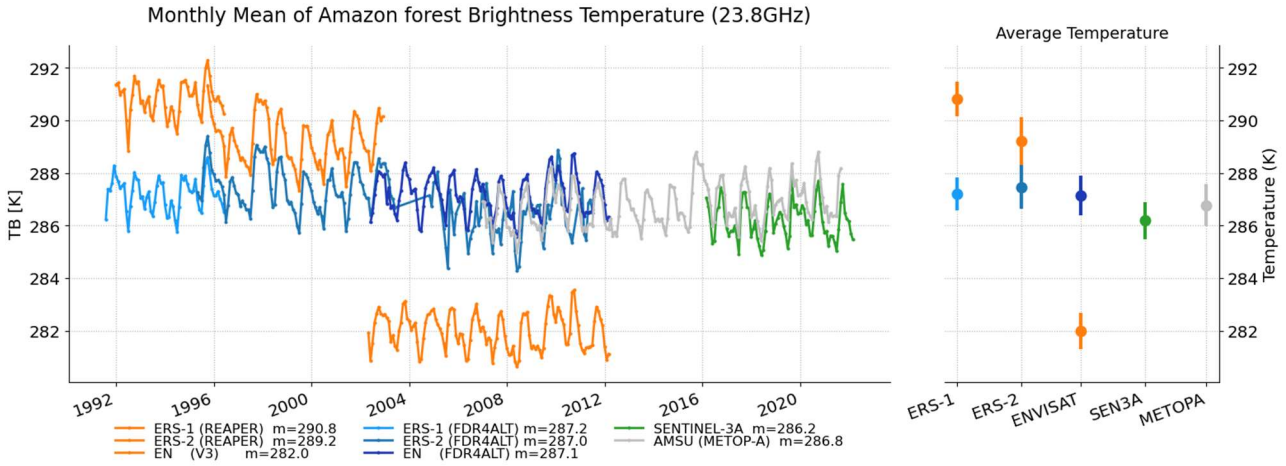

Figure 5-11 : Time series of hottest brightness temperatures over Amazon Forest at 23.8 GHz ERS-1, ERS-2, ENVISAT, MetOp-A and Sentinel-3A. The right panel is showing the average temperature computed over each mission data period.

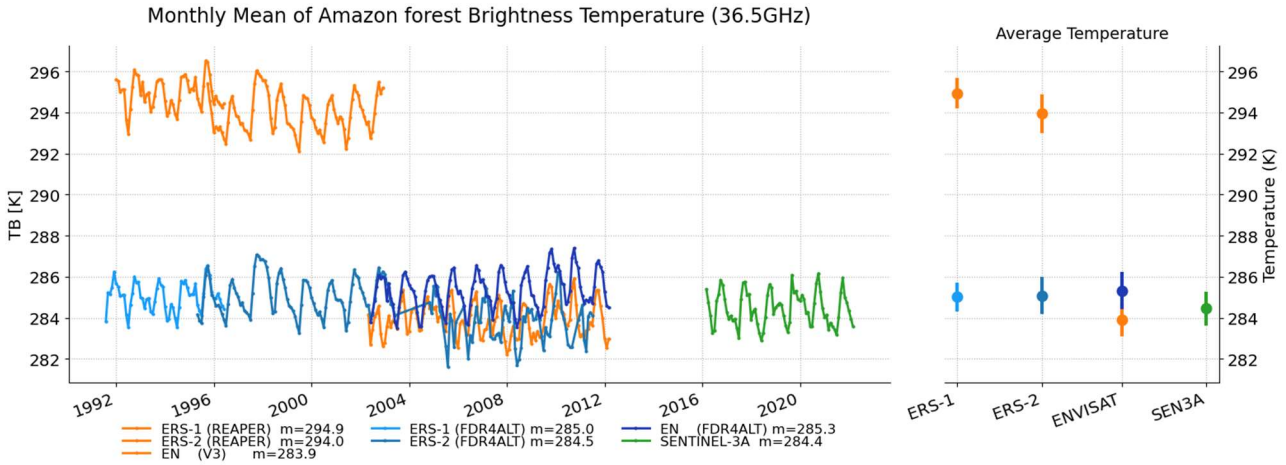

Figure 5-12 : Time series of hottest brightness temperatures over Amazon Forest at 36.5 GHz ERS-1, ERS-2, ENVISAT and Sentinel-3A. The right panel is showing the average temperature computed over each mission data period.

5.3.5 Climatological stability of ocean measurements

Thao et al's method to detect trends in atmospheric water vapor at climatological level in [RD 15] is also applicable to brightness temperatures. It can produce time series of mean brightness temperature and

monthly anomaly. By choosing a reference mission, one can compute the difference of mean brightness temperature and anomaly in order to highlight trends in the brightness temperatures measurements.

This method is also useful to assess the quality of a correction (for instance, gain drop correction for ERS-2 36.5GHz channel). It also allows to check for any regional bias that might be introduced by a processing issue.

In the following sections, Hovmoller plots will be presented. It consists in averaging the data into monthly bins, and then average across the longitude. The result is presented as function of the latitude wrt time. This allows to follow the difference patterns as function of the latitude across the time, to detect seasonal effects or reginal abrupt changes. The same diagnosis is applied to the difference of TB anomalies, to highlight this time the trends.

To carry out these analyses, we will use two missions as reference, with different designs and orbits: AMSU-A on Aqua and TMR on TOPEX. All missions are sun synchronous except for Topex: their characteristics and Local Time at Ascending Node (LTAN) are summarized in Table 7.

AMSU-A is a multi-channel sounding radiometer with 15 channels from 23.8 GHz up to 90 GHz. This radiometer is on-board several missions in the European Polar System (EPS) MetOp missions and in the 15th to 19th NOAA missions. As the sounder has a varying incidence angle, pixels closest to nadir are averaged to provide a near-nadir temperature. AMSU-A data is extracted from L1C data available at ICARE archive center (ftp://ftp.icare.univ-lille1.fr).

Topex Microwave Radiometer (TMR) is a three frequencies (18,21 and 37GHz) instrument on-board the Topex/Poseidon mission (CNES/NASA). The data is extracted from aviso CNES data center. (https://aviso-data-center.cnes.fr)

	ERS-1	ERS-2	ENVISAT	AMSU-A AQUA	TMR
Dataset	FDR4ALT FDR	FDR4ALT FDR	FDR4ALT FDR	L1C ICARE	GDR-F
Inclination	98°	98°	98	98°	66°
Local Time at Ascending Node	22:30	22:30	22:00	13:30	non sun-synchroneous
Frequencies (GHz)	23.8, 36.5	23.8, 36.5	23.8, 36.5	23.8, 31.4	21/37
time coverage	1991-1996	1995-2011	2002-2012	2002-2016	1992-2006

Table 7 : Mission characteristics

VALIDATION OF ERS-1

Hereafter, the validation will be performed by comparing FDR4ALT to the previous reprocessing, using a common reference (TMR). When looking at the distribution of the BT difference (ERS1-AMSU) in Figure 5-13, it shows the same shape for the two reprocessing versions, and the distribution keeps the same std. However, the mean difference is closer to 0 for FDR4ALT reprocessing, which means it is globally closer to TMR GDR-F reprocessing.

Maps of the BT difference, averaged throughout the whole mission period, allows to detect regional effects. Indeed, Figure 5-14 illustrates that the regional effects, probably caused by inaccurate radiometric corrections (such as sidelobe, skyhorn contaminations…), reduced with FDR4ALT reprocessing of 23.8GHz, and disappears for 36.5GHz. The same conclusions can be drought with Figure 5-15 where we can see that these patterns are located to specific areas, with seasonal variations along the time.

When looking at the difference of BT anomaly, no significant trends are observed, the two reprocessings giving similar results.

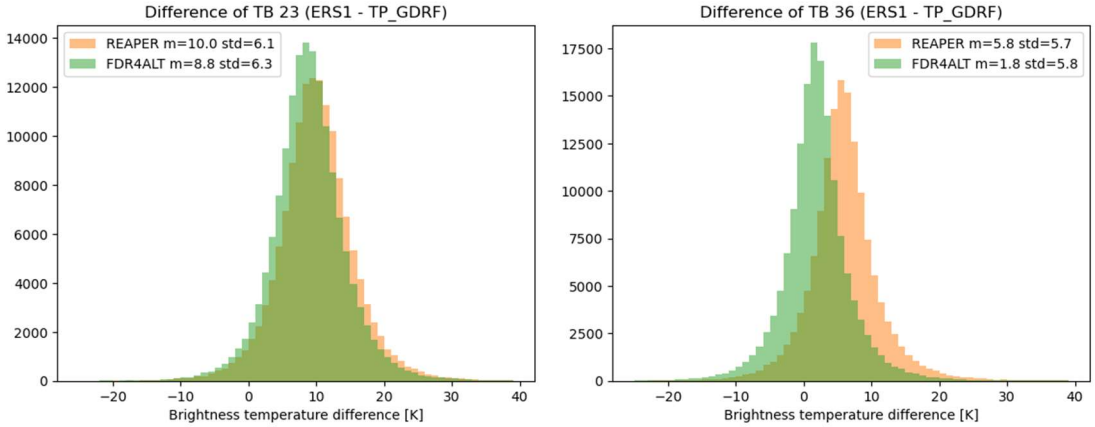

Figure 5-13 : Density plot of BT Difference (ERS-1 – Topex) for channel 23.8GHz (left) and 36.5GHz (right)

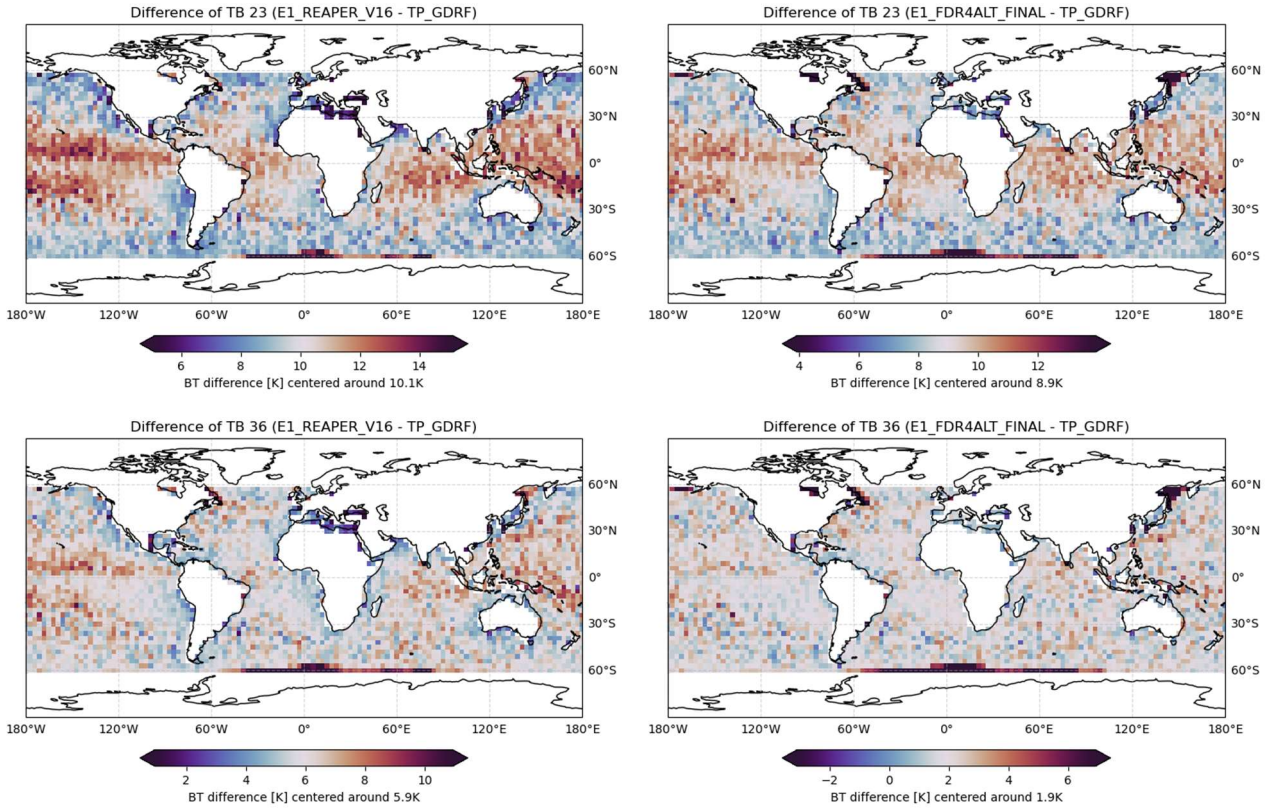

Figure 5-14 : Map of BT Difference of ERS-1 with Topex reprocessing for channel 23.8GHz (top) and 36.5GHz (bottom); for REAPER (left) and FDR4ALT (right) datasets.

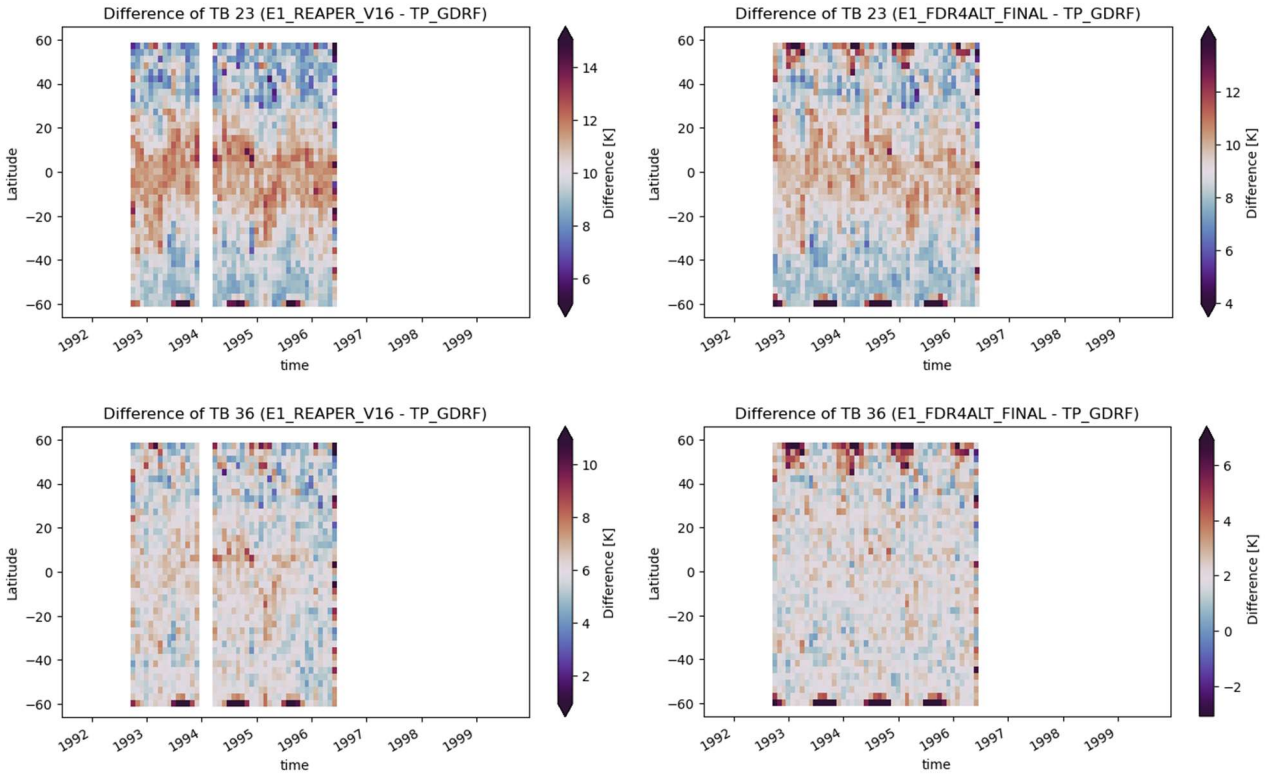

Figure 5-15 : Hovmoller diagram of BT Difference of ERS-1 with Topex reprocessing for channel 23.8GHz (top) and 36.5GHz (bottom); for REAPER (left) and FDR4ALT (right) datasets.

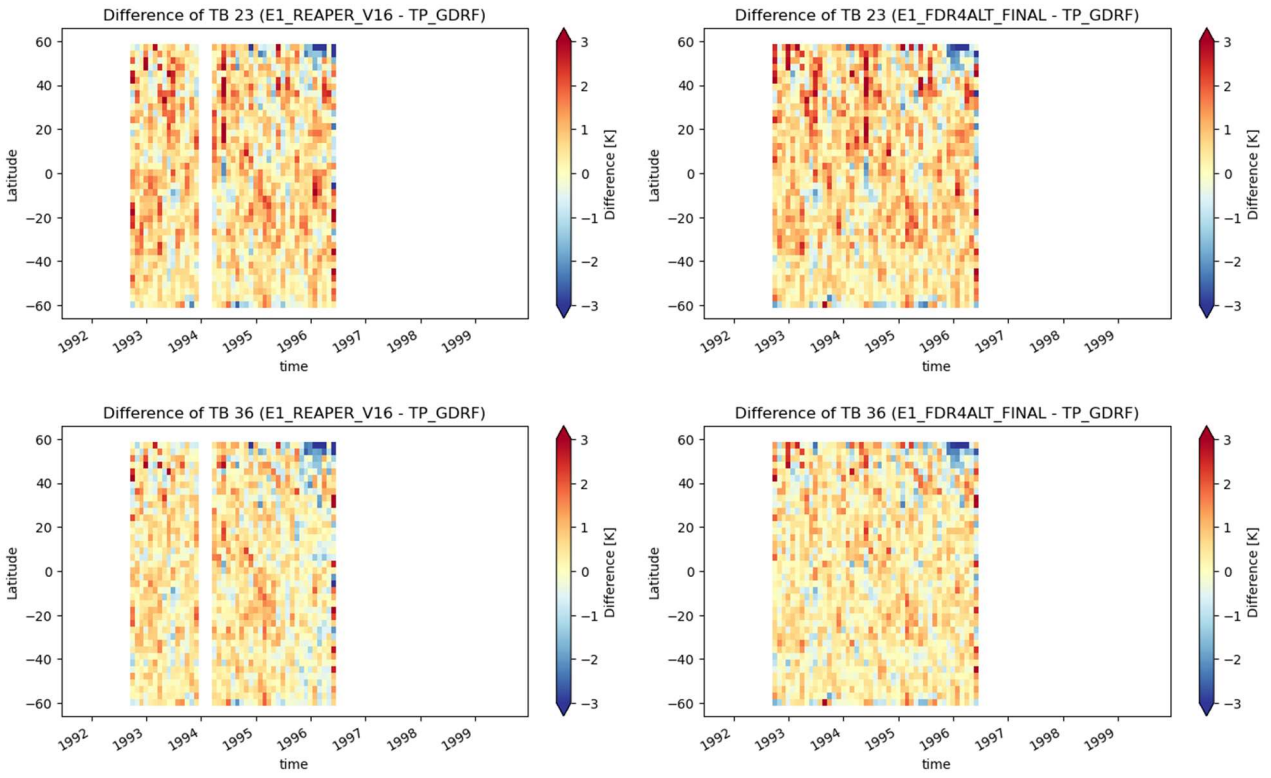

Figure 5-16 : Hovmoller diagram of Difference of BT anomaly of ERS-1 with Topex reprocessing for channel 23.8GHz (top) and 36.5GHz (bottom); for REAPER (left) and FDR4ALT (right) datasets.

VALIDATION OF ERS-2

Hereafter, the validation will be performed by comparing FDR4ALT to the previous reprocessing, using a common reference (TMR). When looking at the distribution of the BT difference (ERS2-TMR) in Figure 5-17, it shows that for 36.5GHz channel, the distribution keeps the same shape and std with FDR4ALT reprocessing. However, the mean difference is closer to 0 for FDR4ALT reprocessing, which means it is globally closer to TOPEX GDR-F reprocessing. For the 23.8GHz channel, the std reduction is significant (7.1K to 6.2K with FDR4ALT), and closer to ERS-1 std. The median value is higher, but this is only reflecting the calibration difference between the two instruments. This channel had many issues (gain drop) corrected; hence a distribution plot can mask a lot of effects.

Maps of the BT difference, averaged throughout the whole mission period, allows to detect regional effects. Indeed, Figure 5-18 illustrates that the regional effects, due to inaccurate corrections, is strongly reduced in FDR4ALT reprocessing of 23.8GHz and disappears for 36.5GHz. The same conclusions can be drought with Figure 5-19 where we can see that these patterns are located to specific areas, with seasonal variations along the time, and also steps in the timeserie corresponding to before/after the gain drop event of 23.8GHz channel.

When looking at the difference of BT anomaly, no significant trend is observed, the two reprocessings giving similar results for the 36.5 GHz channel. The bands and the step in 1996 are associated to the gain drop event which was not corrected in REAPER reprocessing. With FDR4ALT, this event was corrected, hence the step disappeared, and the variations are strongly reduced, but there is still a difference of behaviour before and after 1998. This might indicate that the gain drop correction might be a bit too high of 0.5K for ocean measurements, with respect to the pre-gain drop period.

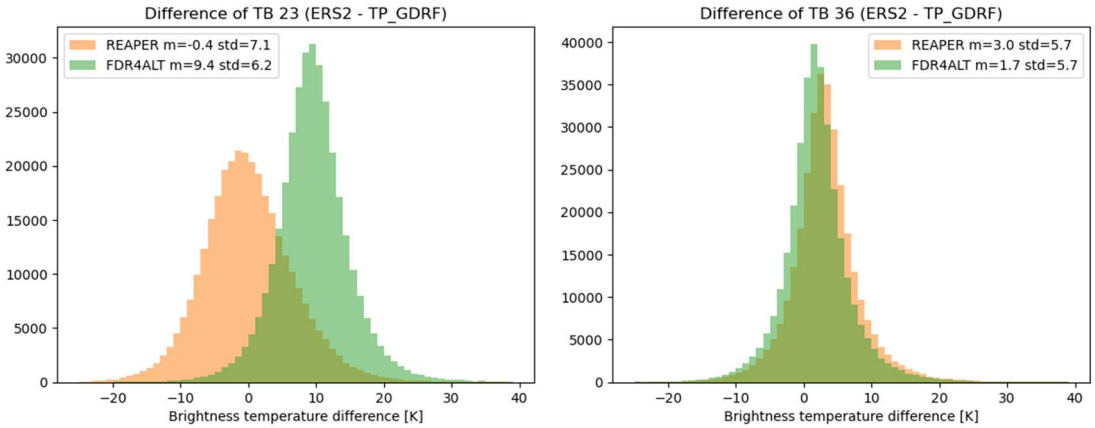

Figure 5-17 : Density plot of BT Difference (ERS-2 – Topex) for channel 23.8GHz (left) and 36.5GHz (right)

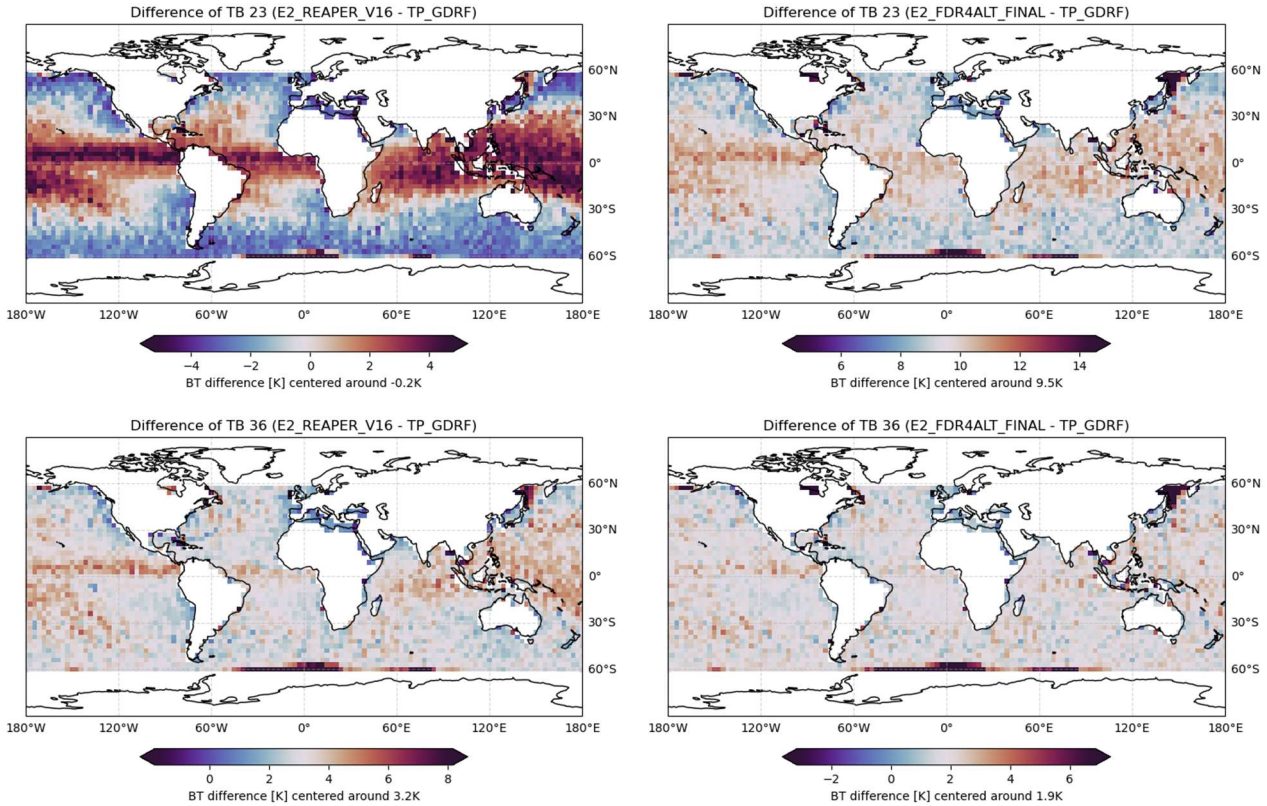

Figure 5-18 : Map of BT Difference of ERS-2 with Topex reprocessing for channel 23.8GHz (top) and 36.5GHz (bottom); for REAPER (left) and FDR4ALT (right) datasets.

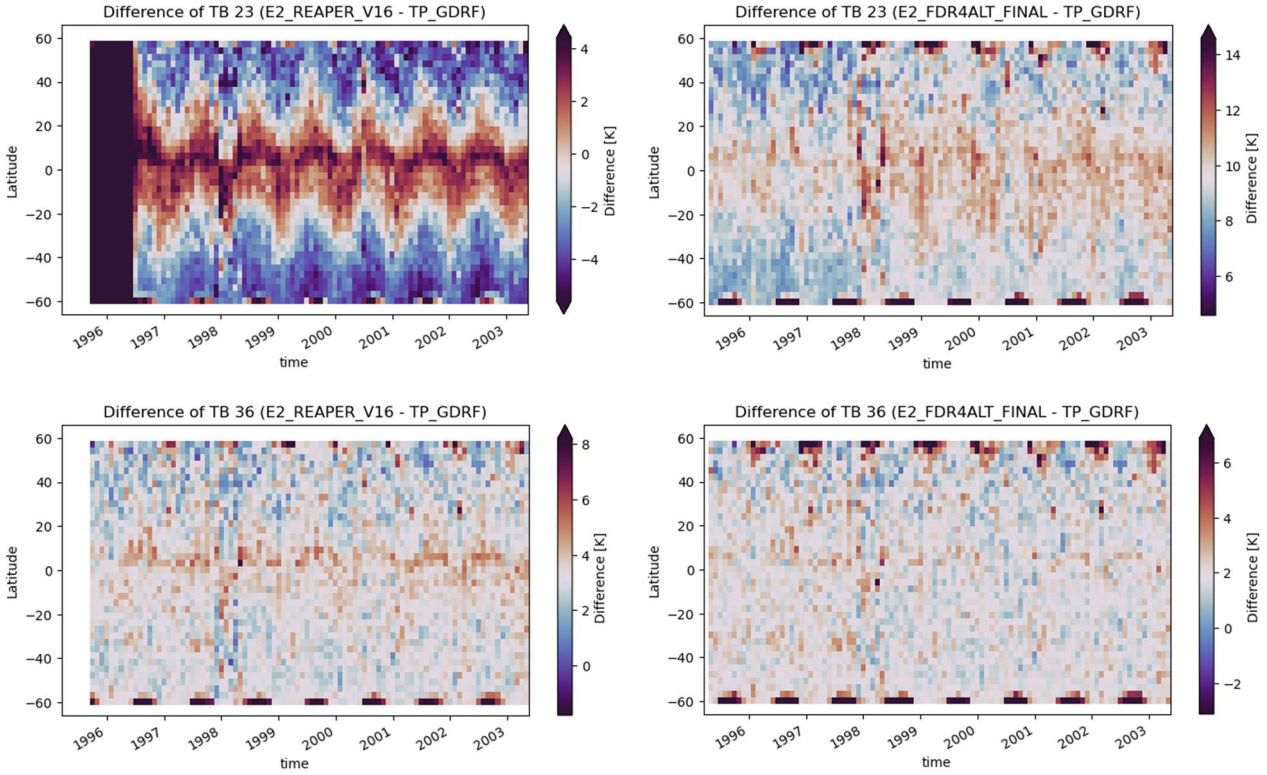

Figure 5-19 : Hovmoller diagram of BT Difference of ERS-2 with Topex reprocessing for channel 23.8GHz (top) and 36.5GHz (bottom); for REAPER (left) and FDR4ALT (right) datasets.

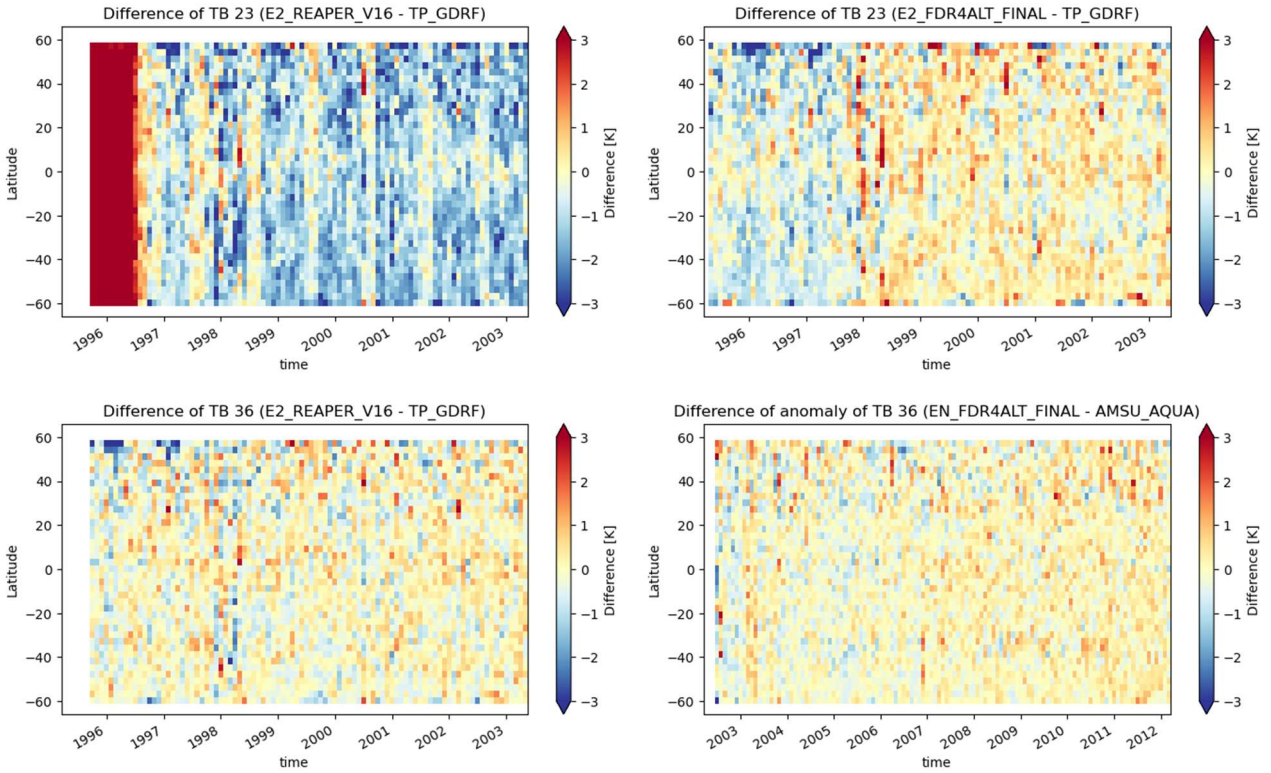

Figure 5-20 : Hovmoller diagram of Difference of BT anomaly of ERS-2 with Topex reprocessing for channel 23.8GHz (top) and 36.5GHz (bottom); for REAPER (left) and FDR4ALT (right) datasets.

VALIDATION OF ENVISAT

Hereafter, the validation will be performed by comparing FDR4ALT to the previous reprocessing, using a common reference (AMSU). When looking at the distribution of the BT difference (EN-AMSU) in Figure 5-21, it shows that for 36.5GHz channel, the distribution keeps the same shape and std with FDR4ALT reprocessing. For the 23.8GHz channel, the std reduction is significant (6.2K to 5.6K with FDR4ALT), and closer to ERS std. The median value is also lower, meaning that FDR4ALT dataset is closer to AMSU then the previous one.

Maps of the BT difference, averaged throughout the whole mission period, allows to detect regional effects. Indeed, Figure 5-22 illustrates that the regional effects, due to inaccurate corrections, is strongly reduced in FDR4ALT reprocessing of 23.8GHz but is only a bit attenuated for 36.5GHz. The same conclusions apply to Figure 5-23 where we can see that these patterns are located to specific areas, with seasonal variations along the time. It indicates that there is probably a contamination that remains uncorrected for this channel.

When looking at the difference of BT anomaly, no significant trend is observed, the two reprocessing giving similar results. The step visible in 2003 on V3 reprocessing disappear with FDR4ALT reprocessing, where we implemented a piecewise correction of 36.5GHz channel.

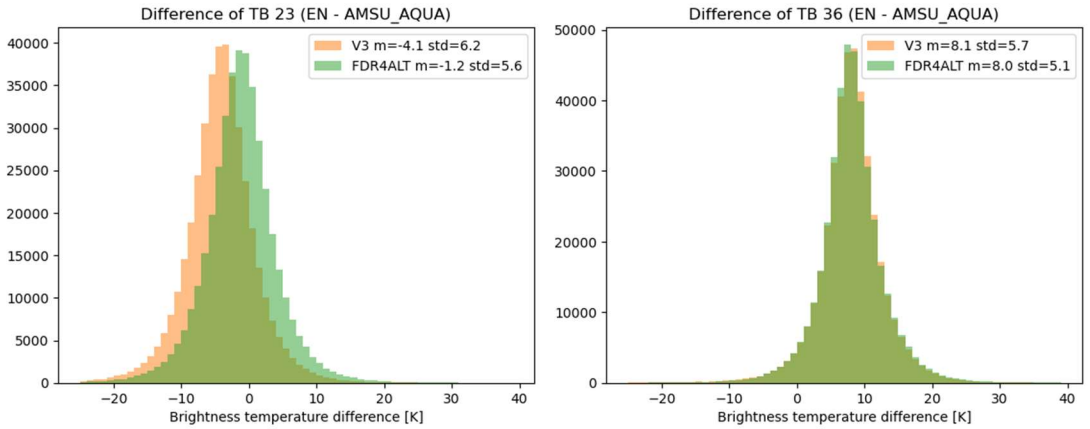

Figure 5-21 : Density plot of BT Difference (ENVISAT – AMSU) for channel 23.8GHz (left) and 36.5GHz (right)

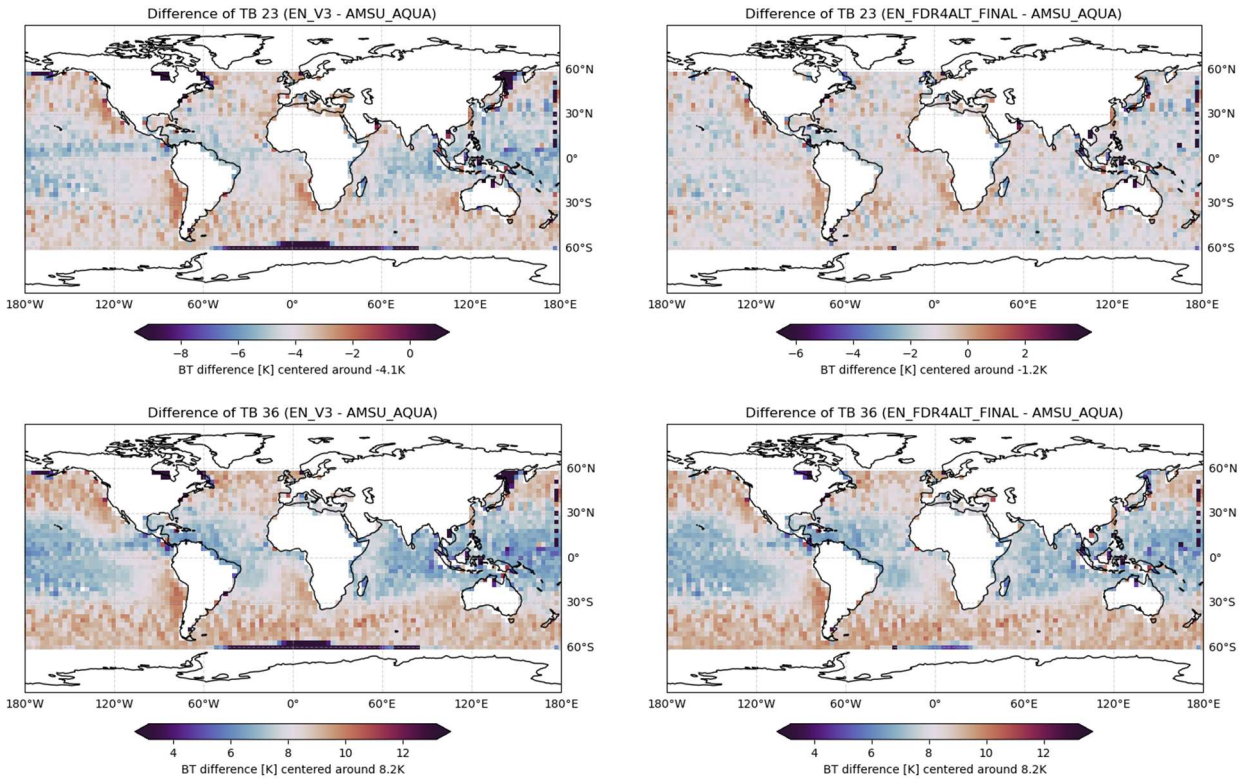

Figure 5-22 : Map of BT Difference of ENIVSAT with AMSU for channel 23.8GHz (top) and 36.5GHz (bottom); for V3 (left) and FDR4ALT (right) datasets.

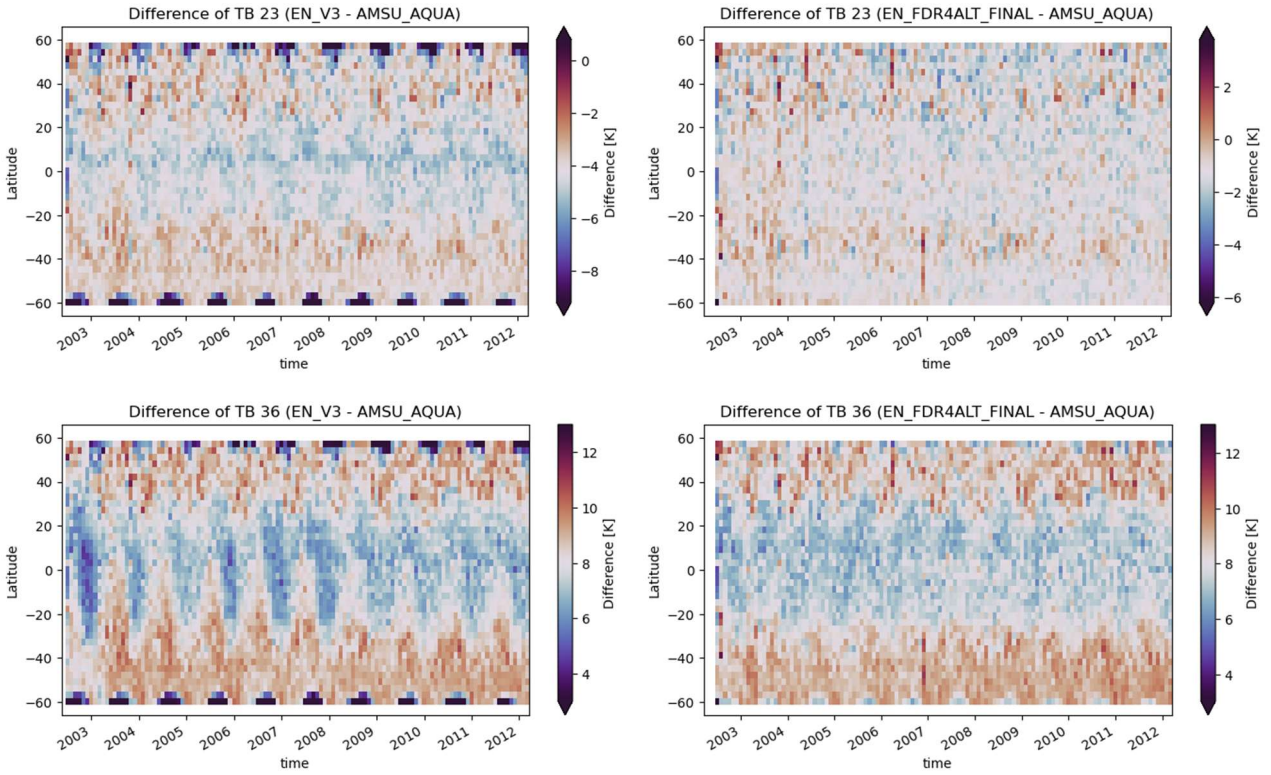

Figure 5-23 : Hovmoller diagram of BT Difference of ENVISAT with AMSU reprocessing for channel 23.8GHz (top) and 36.5GHz (bottom); for V3 (left) and FDR4ALT (right) datasets.

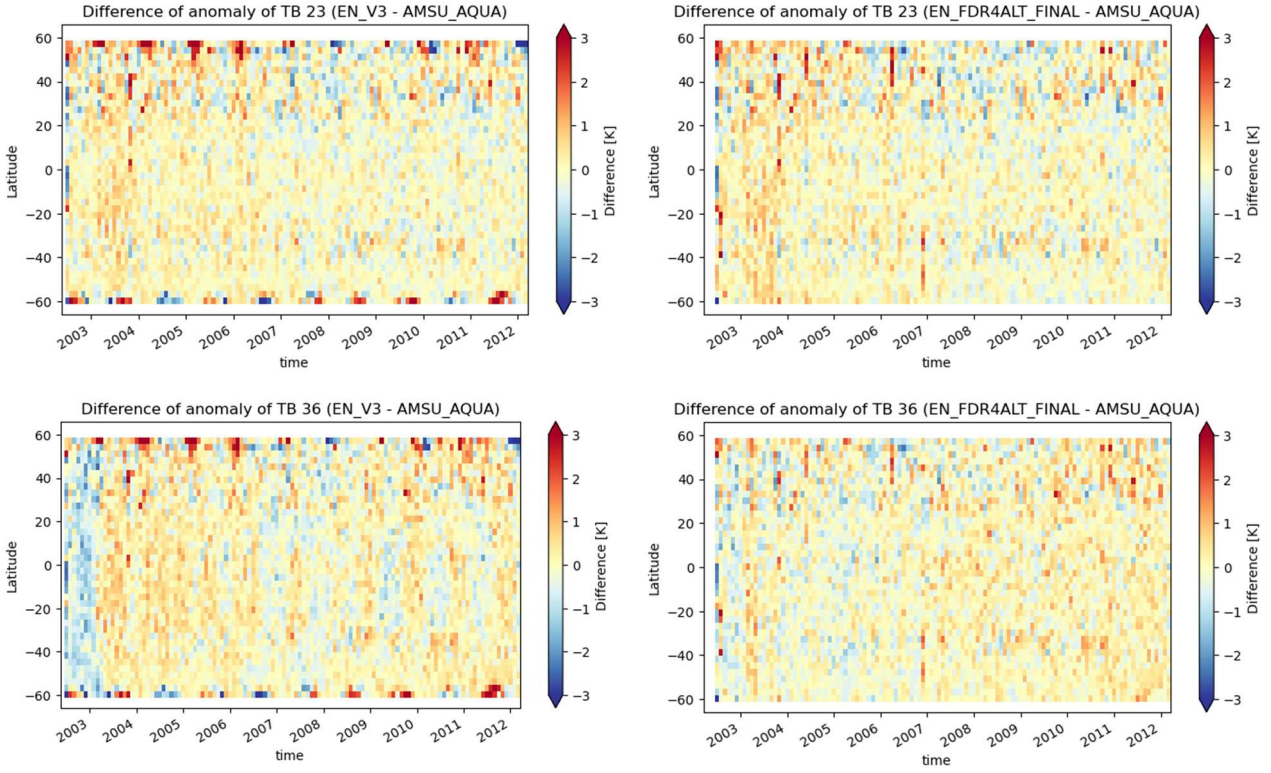

Figure 5-24 : Hovmoller diagram of Difference of BT anomaly of ENVISAT with AMSU for channel 23.8GHz (top) and 36.5GHz (bottom); for V3 (left) and FDR4ALT (right) datasets.

5.4 Conclusions

The FDR4ALT harmonized BT are fully validated. FDR4ALT project has improved the data quality with:

- ✓ Correction/decrease of annual signal for 23.8GHz/36.5GHz for ERS-1
- ✓ Correction/decrease of annual signal for 23.8GHz/36.5GHz, correction of gain drop for 23.8GHz for ERS-2
- ✓ Correction/decrease of annual signal for 23.8GHz/36.5GHz and correction of 36.5GHz step in 2003 for ENVISAT.

The use of the FDR MWR instead of the previous reprocessing activities is therefore strongly recommended to the users.

It could be of interest for future studies to understand the residual contaminations observed and characterize its effect on WTC.

5.5 Reference documents

RD 7	C. Ruf, 2000: Detection of Calibration Drifts in spaceborne Microwave Radiometers using a Vicarious cold reference, **IEEE Trans. Geosci. Remote Sens., 38, 44-52**
RD 8	S. Brown, C. Ruf, 2005: Determination of an Amazon Hot Reference Target for the on-orbit calibration of Microwave radiometers, **Journal of Atmos. Ocean. Techno., 22, 1340-1352**
RD 9	L. Eymard, E. Obligis, N. Tran, F. Karbou, M. Dedieu, 2005: Long term stability of ERS-2 and TOPEX microwave radiometer in-flight calibration, **IEEE Trans. Geosci. Remote Sens., 43, 1144-1158**
RD 10	C. Ruf, 2002: Characterization and correction of a drift in calibration of the TOPEX microwave radiometer, **IEEE Trans. Geosci. Remote Sens., 40, 509-511**
RD 11	R. Scharoo, J. Lillibridge, W. Smith, 2004: Cross-calibration and long-term monitoring of the microwave radiometers of ERS, TOPEX, GFO, Jason and Envisat, **Marine Geodesy, 27, 279-297**
RD 12	M. L. Frery et al., "Sentinel-3 microwave radiometers: Instrument description, calibration and geophysical products performances," Remote Sens., vol. 12, no. 16, pp. 1–24, 2020.
RD 13	B. Picard, M.-L. Frery, E. Obligis, L. Eymard, N. Steunou, and N. Picot, SARAL/AltiKa Wet Tropospheric Correction: In-Flight Calibration, Retrieval Strategies and Performances, **Marine Geodesy., 2015.**
RD 14	Brown, S., C. Ruf, S. Keihm, and A. Kitiyakara: Jason Microwave Radiometer Performance and On-Orbit Calibration, **Mar. Geod., vol. 27, no. 1–2, pp. 199–220, 2004**.
RD 15	S. Thao et al.: Trend and variability of the atmospheric water vapor: a Mean Sea Level issue, **American Meteorological Society, vol 31, 2014.**
RD 16	Guijarro, J.; Auriol, A.; Costes, M.; Jayles, C.; Vincent, P., 2000. MWR and DORIS - Supporting Envisat's radar altimetry mission, ESA BULLETIN-EUROPEAN SPACE AGENCY, (104):41-46, https://www.esa.int/esapub/bulletin/bullet104/guijarro104.pdf
RD 17	R. Bernard, L. Comec, L. Eymard, L. Tabary, 1993: The Microwave Radiometer Aboard ERS-1 : Part 1-Characteristics and Performances, **IEEE Transactions on Geoscience and Remote Sensing,** vol. 31, no. 6, 1993

Appendix A - Complementary analysis

Appendix A 1 -First tests of the application of the Adaptive Retracker on ERS-1/2

In the frame of the FDR4ALT project, the Adaptive retracker has been successfully applied on ENVISAT as explained in section 4 thanks to the work performed on the PTR.

On ERS, the so-called OLC-PTR cannot be used as they are not oversampled. The other calibrations called SPTR (Scanning PTR) could be used for such a purpose, but they need to be reconstructed using a dedicated algorithm as described in the Product User Guide. In the time frame of this project, we could not test the SPTR arrays as inputs for the Adaptive, therefore we used a synthetic PTR (with the correct Hamming window applied)

The Adaptive was applied on one cycle of ERS data, using a theoretical PTR. In terms of waveform fit, the results are satisfactory as we can see on Figure 5-25 : The Adaptive MQE is systematically lower than the MLE3 MQE, which means that the Adaptive model fits the real waveform better than the MLE3 model.

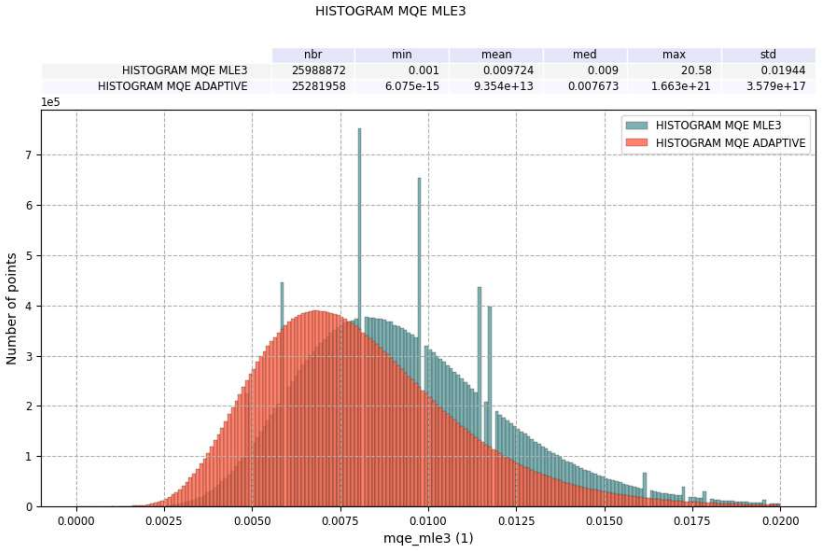

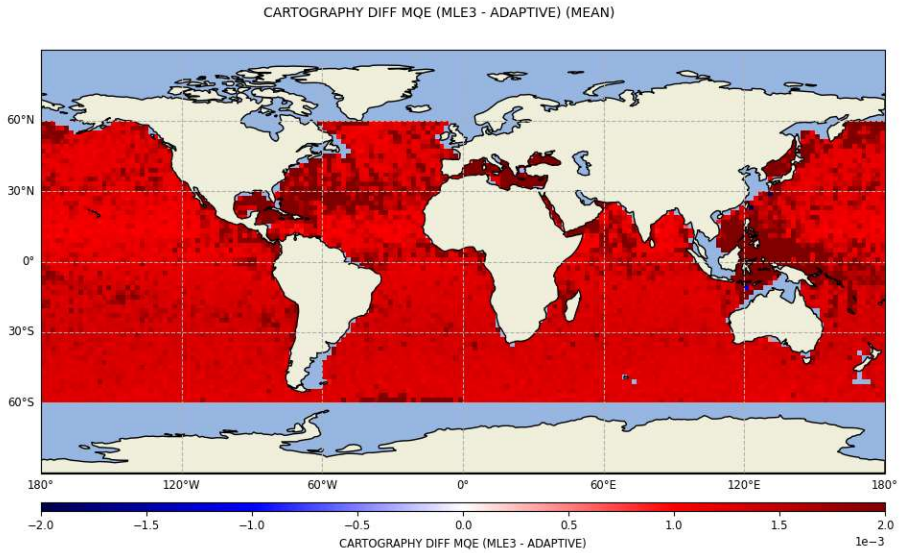

Figure 5-25 : Histograms of MQE MLE3 and Adaptive (above) and gridded map of the difference MLE3-Adaptive for one ERS cycle (below)

However, looking at waveform residuals in Figure 5-26, we can see that the fit on the leading edge is not better with the Adaptive, compared to the MLE3. The leading edge is the most important part of the waveform fit, so this result is not satisfactory and needs to be further investigated.

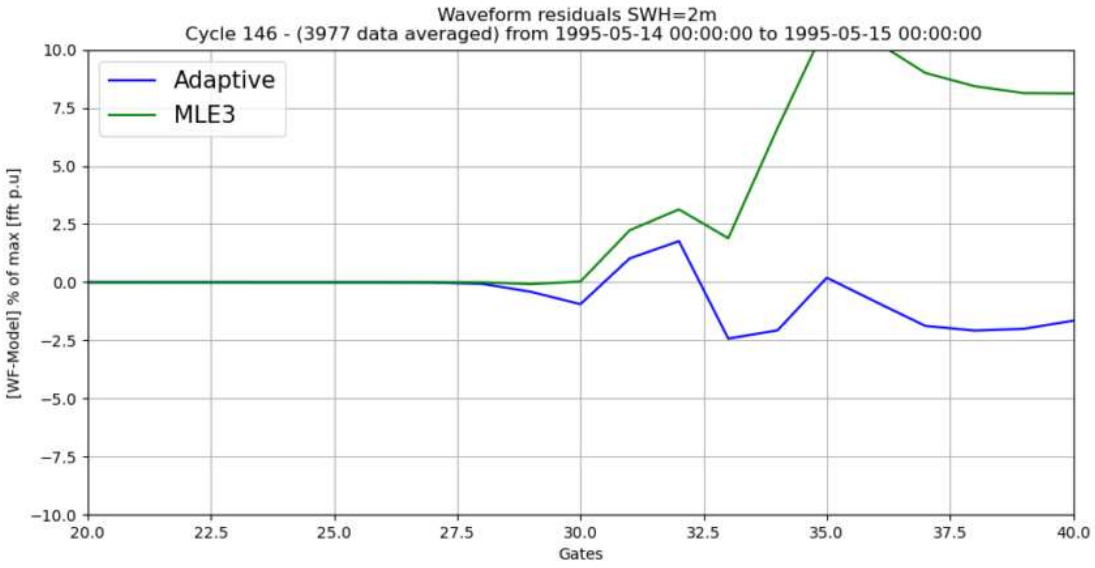

Figure 5-26 : Waveforms residuals for SWH=2m, zoomed on the leading edge

Furthermore, Figure 5-27 shows the difference of range [MLE4-Adaptive] and SWH [MLE4-Adaptive] with respect to SWH Adaptive or SWH MLE3. We can see a very strong dependency of the difference in function of the SWH, which is not expected and needs to be further investigated and understood. It could be linked to the fact that no look-up tables have been applied on ERS data.

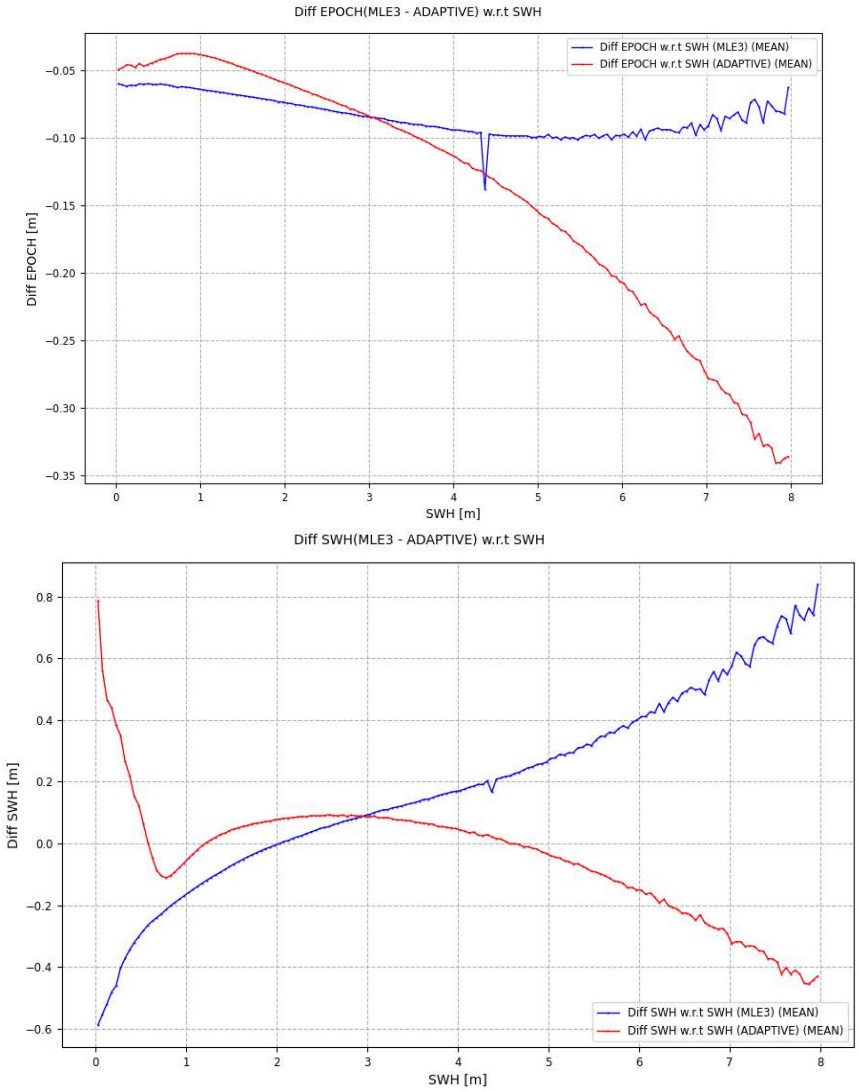

Figure 5-27 : Difference of Epoch [MLE3-Adaptive] and difference of SWH [MLE3-Adaptive] w.r.t SWH Adaptive (red) or SWH MLE3 (blue)

These results are preliminary and further investigation is needed to see if the Adaptive can be successfully applied on ERS. The choice of the PTR in input (SPTR or synthetic) will be most likely critical to ensure satisfactory results.

Appendix B - FDR4ALT deliverables

The table below lists all FDR4ALT deliverables with their respective ID number and confidentiality level.

Document	ID	Confidentiality Level
Products Requirements & Format Specifications Document	[D-1-01] [D-2-02]	Public
Roadmap & Product Summary Document	[D-1-02]	Project Internal
Data Requirements Document	[D-1-03]	Project Internal
System Maturity Matrix	[D-1-04]	Project Internal
Examples of products	[D-1-05]	Project Internal
Review Procedure Document	[D-1-06]	Project Internal
Review Data Package	[D-1-07]	Project Internal
Phase 1 Review Report Document	[D-1-08]	Project Internal
Detailed Processing Model Document	[D-2-01]	Public
Round Robin Assessment Report Document	[D-2-03]	Public
Data Production Status Report	[D-3-01]	Project Internal
Final Output Dataset	[D-3-01]	Public
Product Validation Plan	[D-4-01]	Project Internal
Product Validation Report : FDR	[D-4-02a]	Public
Product Validation Report : Sea-Ice TDP	[D-4-02b]	Public
Product Validation Report: Land-Ice TDP	[D-4-02c]	Public
Product Validation Report : Ocean Waves TDP	[D-4-02d]	Public
Product Validation Report : Ocean & Coastal TDP	[D-4-02e]	Public
Product Validation Report: Inland Waters TDP	[D-4-02f]	Public
Product Validation Report: Atmosphere TDP	[D-4-02g]	Public
Uncertainty Characterization Definition Document	[D-5-01]	Project Internal
Uncertainty Characterization Report	[D-5-02]	Public
Product User Guide	[D-5-03]	Public
Completeness Report ALT	[D-7-01]	Public
Completeness Report MWR	[D-7-02]	Public

Table 8 : List of FDR4ALT deliverables

Appendix C - Acronyms

AATSR	Advanced Along-Track Scanning Radiometer
AEM	Airborne electromagnetic
AIR	AIRWAVES2
AVISO	Archivage, Validation et Interprétation des données des Satellites Océanographiques
AMSR-E	Advanced Microwave Scanning Radiometer - Earth Observing System sensor
AMSU-A	Advanced Microwave Sounding Unit-A
ALT	Altimetry
ASSIST	Arctic Shipborne Sea Ice Standardization Too
ATM	Airborne Topographic Mapper
BDHI	Base de datos Hidrologica integrada
BGEP	Beaufort Gyre Exploration Project
CAL	Calibration
CCI	Climate Change Initiative
CFOSAT	Chinese-French Oceanic SATellite
CDS	Copernicus Data Service
CLS	Collecte Localisation Satellite
CMEMS	Copernicus Marine Environment Monitoring Service
CMSAF	Climate Monitoring Satellite Application Facility
CNES	Centre National des Etudes Spatiales
CRREL	Cold Regions Research and Engineering Laboratory
DAHITI	Database for Hydrological Time Series of Inland Waters
DGA	Direccion General de Aguas
ENVISAT	ENVIronment SATellite
EMD	Empirical mode decomposition
EO	Earth Observation
EPS	European Polar System
ERA	ECMWF Re-Analysis
ERS	European Remote-Sensing Satellite
ESA	European Space Agency
ESTEC	European Space Research and Technology Centre
FCDR	Fundamental Climate Data Record
FDR	Fundamental Data Records
FIDUCEO	Fidelity and uncertainty in climate data records from Earth Observations
FMR	Full Mission Reprocessing
FYI	First Year Ice
GEWEX	Global Energy and Water Exchanges
GFO	Geosat Follow-On
GIEMS	Global Inundation Extent from Multi-Satellites
GMSL	Global Mean Sea Level
GNSS	Global Navigation Satellite System
GPM	Global Precipitation Measurement
GRDC	Global Runoff Data Centre
G-REALM	Global Reservoir And Lake Monitor
G-VAP	GEWEX Water Vapour Assessment
HYBAM	HYdro-géochimie du Bassin AMazonien
ICARE	

IGM	Instituto Geografico Militar
IGN	Instituto Geografico Nacional
IMB	Ice Mass Balance
INA	Instituto Nacional de Agua
ISRO	Indian Space Research Organisation
IRPI	Istituto di Ricerca per la Protezione Idrogeologia
IWMI	International Water Management Institute
LEGOS	Laboratoire d'Etudes en Géophysique et Océanographie Spatiales
LIDAR	Ligth Detection And Ranging
LTAN	Local time of the ascending node
LWP	Liquid Water Path
MAC	Multisensor Advanced Climatology
MEAS-SIM	Measure-Simulation
MQE	Mean Quadratic Error
MSSH	Mean Sea Surface Height
MWR	Microwave Radiometer
NASA	National Aeronautics and Space Administration
NE	North East
NN	Neural Network
NPI	Norwegian Polar institute
NWP	Numerical Weather Prediction
NOAA	National Oceanic and Atmospheric Administration
OIB	Operation Ice Bridge
OLC	Open Loop Calibration
OSTST	Oceanography Surface Topography Science Team
POSTEL	Pôle d'Observation des Surfaces continentales par TELEdétection
PTR	Point Target Response
RD	Reference Document
REAPER	Reprocessing of Altimeter Products for ERS
RM	Review Meeting
RSS	Remote Sensing System
SALP	Service d'Altimétrie et de Localisation Précise
SARAL	Satellite with Argos and Altika
SLA	Sea Level Anomaly
SCICEX	Submarine Arctic Science Program
SGDR	Sensor Geophysical Data Record
SHOA	Servicio Hidrografico y Oceanografico de la Armada
SSB	Sea State Bias
SSH	Sea Surface Height
SSM/I	Special sensor microwave/imager
SST	Sea Surface Temperature
SWH	Significant Wave Height
SWIM	Surface Waves Investigation and Monitoring instrument
TAC	Thematic Assembly Center
TB	Température de Brillance (Brightness Temperature)
TDP	Thematic Data Products
TDS	Test Data Set
TFMRA	Threshold First-Maximum Retracker Algorithm
TMR	Topex Microwave Radiometer
TP	Topex/Poseidon

TCWV	Total column water vapour
VCC	Vicarious calibration
VS	Virtual Station
ULS	Upward Looking Sonar
USA	United States of America
USDA	United States Department of Agriculture
WHALES	Wave Height Adaptive Leading Edge Subwaveform
WTC	Wet Tropospheric Correction